Design, Modeling, Simulation, and Testing of Resonant Micromachined Magnetic Field Sensors

by

Behraad Bahreyni

A thesis submitted to the Faculty of Graduate Studies

in partial fulfillment of the requirements for the degree of

Doctor of Philosophy

Department of Electrical and Computer Engineering

The University of Manitoba

Winnipeg, MB, Canada

THE UNIVERSITY OF MANITOBA

FACULTY OF GRADUATE STUDIES

*****

COPYRIGHT PERMISSION

Design, Modeling, Simulation, and Testing of Resonant Micromachined Magnetic Field Sensors

BY

Behraad Bahreyni

A Thesis/Practicum submitted to the Faculty of Graduate Studies of The University of Manitoba in partial fulfillment of the requirement of the degree

OF

DOCTOR OF PHILOSOPHY

To the people of my country, Iran

and

To my father, mother, and wife

for their love and support

Abstract

This thesis is about the development of a novel micromachined magnetic field sensor. A linear response to a wide range of magnetic fields makes this design suitable for applications where large fields need to be measured with high resolution. The operation of this sensor is based on a shift of the resonant frequency of a resonating microstructure in presence of a magnetic field. The flexural beams of the micromachined resonator are designed so that an axial force is exerted on them when exposed to a magnetic field. The axial force will cause a positive or negative shift in the resonant frequency of the structure, depending on the directions of the magnetic field and a DC current that flows in the crossbars of the sensor. The design of the sensor allows for its fabrication in many standard MEMS processes, and therefore sensor prototypes can be quickly and inexpensively fabricated and transfered to mass production.

A comprehensive model of the sensor is derived which encompasses the interaction of the mechanical operation of the device and its magneto- and electrostatic response. This model is verified using finite element simulations and confirmed with experiments on four different sensor geometries. Three different process flows are employed to fabricate the sensors. The pros and cons of each of the process flows are pointed out. Custom signal processing electronics are designed and used to analyze the sensor

data. The noise behavior of each sensor is investigated, the minimum detectable signal determined, and the best configuration selected.

The measured resolution of the sensors is about $80\mu T$ if they are used with the designed signal processing electronics. The theoretical minimum detectable signal with current devices is on the order of $200nT$. Methods to improve the noise performance of the current sensors are suggested as well as fabrication and signal processing techniques that allow for device designs with better sensitivities.

Acknowledgments

First and foremost, I would like to thank my advisor, Dr. Cyrus Shafai, for his support, patience, and trust in me. I am not sure I would be at this stage at this time if it were not for his encouragements and continuous support. Administrative details of running a state of the art laboratory is one of the many things that I learned from Dr. Shafai besides MEMS. I am grateful for all the great experiences that I have had while being his student.

My discussions on different issues with professors Douglas Thomson and Gregory Bridges were always fruitful and quite often let me see the problem from a different, and sometimes the correct, perspective. I would like to thank them for doing more for me than what most committee members do.

I benefited from the advices of professor Ted Hubbard from Dalhousie University on the theory and testing of micromachined devices even before he agreed to be on my committee. I am thankful for his time.

Professor Johan van Lierop kindly agreed to be on my committee on short notice. I appreciate the time he spent reading an engineering thesis.

I would like to thank Professor Gwyn Williams who kindly spared his time and offered me his advice when I needed it.

Professors Buchanan and Oliver from the ECE department helped at various times with their insight into the physics of the devices or the testing of them. I appreciate their care about my research matters.

During the course of this project, I benefited from my discussions with professors Gary Fedder (Carnegie Mellon University), Radivoje Popovic (Ecole Polytechnique Federal de Lausanne), and Pavel Ripka (Czech Technical University). I am grateful for their help to a student they met at conferences.

I learned quite a bit about microfabrication from Stephanie Bozic (University of Alberta) and Lianne Lester (University of Manitoba). I am thankful for their patience and attention.

Shafaat Bazaz from CMC Microsystems every now and then helped with information about fabrication processes and many other issues. Sarah Neville and Jim Quinn, also from CMC Microsystems, assisted me at numerous occasions with technical or administrative issues. I am grateful for their care.

Without doubt, the assistance I received a various occasions from our talented technicians Alan McKay, Allen Simmons, Guy Jonatschick, Mount-First Ng, and Ken Biegun played a very important role in completion of my project. Karin Kroeker, Judy Noble, and Shelly Girardin helped me often by taking care of most of the administrative issues for me. I hereby would like to thank them all for their efforts.

Many of my friends discussed different issues with me and helped me understand them better. Other friends had to patiently wait when I was using the equipment they badly needed. I am thankful in particular to: Farshid Najafi, Alireza Foroozesh, Jun Hui Zhao, Kar Mun Cheng, Alireza Motieifar, Chris Rohde, Reza Ghorbani, Zhi Nong Weng, and Jane Cao.

My Canadian friends, Tim and Val Frose and Leslie Baronas let me in their homes when I needed it most. A large portion of my good memories in Canada is about the time I spent with them.

The guidance, encouragement, and support from my parents are at the center of everything in my life that counts as a success. Their selfless love has been my motivation throughout my life. I hope to be able to serve them better one day.

Last but definitely not least, I want to thank the love of my life, my wife, Solmaz. She patiently stood by my side in the not-so-easy student life and had to postpone much of her wishes. I hope I can make our future life together easier for her.

Table of Contents

List of Symbols

B	Magnetic flux density, T
C	Capacitance, F
E	Young's modulus of the material, Pa
$\mathcal{F}$	Distributed force, $N \cdot m^{-1}$
$\mathcal{I}$	Second moment of inertia, m^4
I_{XB}	Current in the crossbars, A
k_a	Axial spring constant of the beam springs, $N \cdot m^{-1}$
k_b	Spring constant of the beam springs , $N \cdot m^{-1}$
K_B	Boltzmann's constant, $1.3806 \times 10^{-23}\, J \cdot K^{-1}$
K_n	Knudsen number
L_{XB}	Length of the crossbars, m
$\mathcal{M}$	Bending moment, $N \cdot m$
M_s	Mass of the shuttle, kg
M_b	Mass of the beam springs, kg
$\mathcal{P}$	Axial force, N
Q	Quality factor of the resonance
q_{gen}	Produced heat per volume, $W \cdot m^{-3}$

N	Number of beam springs
R_{XB}	Resistance of the crossbars, Ω
T	Temperature, K
$\mathcal{V}$	Shearing force, N
V_a	Voltage at node A, V
V_A	DC voltage at node A, V
v_a	AC voltage at node A, V
w	Deflection, m
$\bar{y}$	Fractional frequency deviation
$S_B^{f_0}$	Sensitivity to magnetic fields, $Hz \cdot T^{-1}$
$S_{\mathcal{P}}^{f_0}$	Sensitivity to axial forces, $Hz \cdot N^{-1}$
$S_y(f)$	Spectral density of fractional frequency fluctuations
$S_\phi(f)$	Spectral density of phase fluctuations
α	Thermal expansion coefficient, $m \cdot K^{-1}$
ϵ	Permittivity of the material for electrostatic analysis, $F \cdot m^{-1}$
η	Viscous coefficient of the gas ambient, $kg \cdot m^{-1} \cdot sec^{-1}$
κ	Thermal conductivity, $W \cdot m^{-1} \cdot K^{-1}$
ω	Radian frequency, $rad \cdot sec^{-1}$
ω_0	Resonant frequency of the structure, $rad \cdot sec^{-1}$
ρ	Mass density, $kg \cdot m^{-3}$
σ_{th}	Thermal stress in beams, Pa
$\sigma_y^2(\tau)$	Allan variance of a set of datapoints integrated over period τ
ζ	Damping coefficient, $N \cdot m^{-1} \cdot sec$

List of Figures

List of Tables

Chapter 1

Introduction

The beginning is the most important part of the work.

Plato (427BC – 347BC)

Magnetic field sensors have a ubiquitous presence in the modern life. Numerous applications in different fields of engineering, science, and industry rely on the performance, ruggedness, and reliability of magnetic field sensors. The list of magnetic sensor applications includes, but is not limited to, position-sensing, non-contact switching, vehicle detection, navigation, mineral prospecting, brain function mapping, etc. As an example, there can be as many as 40 magnetic field sensors in a modern automobile which are used for various purposes. Depending on application, different types of magnetic field sensors are employed. Some magnetic field sensors have digital outputs (e.g., magnetic relays and resonators) while others produce analog outputs (e.g., current sensors). Micromachining can be employed to reduce the size, and in

some cases, enhance the performance of the conventional types of magnetic sensors. It also allows for new methods of magnetic field sensing.

In this chapter, the terms and parameters which are used when dealing with the literature about magnetic fields are introduced. This is followed by a description of the most common methods of sensing magnetic fields. Examples of micromachined magnetic field sensors are discussed next. The chapter concludes with a comparison of the new sensor design with other magnetic sensors, emphasizing the novel aspects of the design.

1.1 Common terms

According to *MKS* units, the unit for the strength of a magnetic field (magnetic field intensity), H, is A/m, the unit for magnetic flux is Weber (Wb), and the units for magnetic flux density, B, is Tesla (T) or $Weber/m^2$ [1].

For each material, the ratio of magnetic flux density, B, to magnetic field strength, H, is called *permeability*: $\mu = \mu_r \mu_0 = \frac{B}{H}$, where μ_0 is the permeability of free space ($\mu_0 = 4\pi \times 10^{-7} H/m$) and μ_r is the relative permeability of the material. Except for ferromagnetic materials such as iron, nickel, and permalloy, the relative permeability of most materials is close to 1.

One often has to deal with small numbers in magnetism if *MKS* units are used. The other commonly used system of units is the *CGS* system. In *CGS* system, the unit for magnetic field strength and magnetic flux density are Oersted (Oe) and Gauss (G), respectively. It turns out that $1Oe = 79.55 A/m$ and $1G = 10^{-4} T$. Permeability of free space in *CGS* units is 1: $\mu_0 = 1 G/Oe$.

The magnetic field strength of earth is about $60\mu T$ in the *MKS* system, or $0.6G$ in the *CGS* system.

1.2 Magnetic field sensing technologies

This section describes the most common methods used for magnetic field sensing. Figure 1.1 illustrates the practical limits for some of the common magnetic field sensing techniques [2–4]. For typical applications, a sensor has to detect the difference between a high and a low value of field around an average, which is of the order of $10^{-3}T$ in recording applications, but can exceed $0.1T$ in position sensors.

Magnetic field sensors can also be categorized based on whether their output is analog or digital. Sensors with analog output provide a continuous signal with changes of the present magnetic field. Most magnetic field sensors fall into this category. However, in many cases a sensory system has to communicate with a digital processor and the use of an analog to digital converter is inevitable if an analog sensor is used, which in turns adds to the overall cost of the system. Sensors with digital

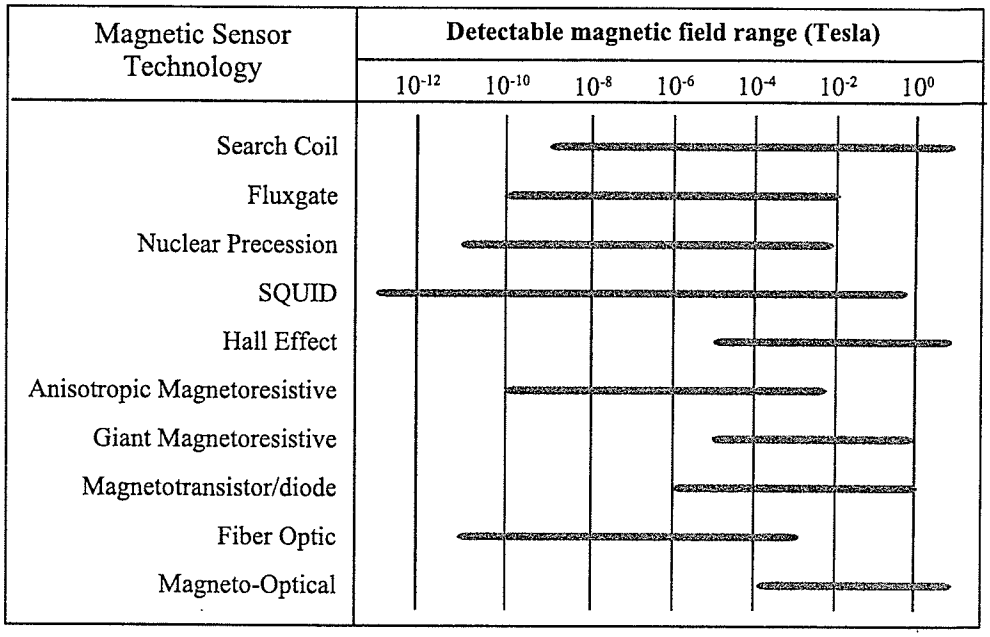

Figure 1.1: *Practical ranges of different magnetic field sensor technologies.*

outputs, on the other hand, can be used more easily for such applications. If the data is embedded in signal frequency rather than its amplitude, the information can be easily read by a digital system. It is sometimes possible to design a resonator sensor with direct frequency output which is relatively simple to measure using a counter for either calculating the frequency or the period of the waveform [5].

1.2.1 Search coil sensors

A search coil sensor is simply made of a coil, with or without a core (see Figure 1.2). Operation of these sensors is based on electromagnetic induction. Faraday's law states that if the magnetic flux inside a coil changes a voltage proportional to the rate of change of the flux is generated between its leads. This voltage is generally known as electromotive force (emf) [2,4,6]. Mathematically, Faraday's law is stated as:

$$emf = -\frac{d\Phi}{dt} \tag{1.1}$$

where Φ is the magnetic flux through the coil.

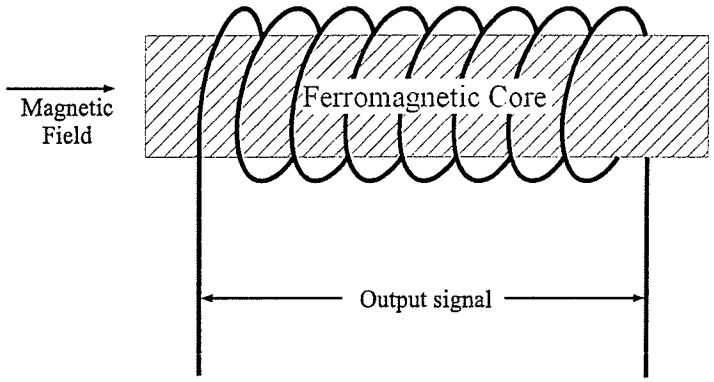

Figure 1.2: *Search coil schematic.*

The flux through the coil changes if the coil is inside a time-varying magnetic field or if the coil moves in a nonuniform field. A ferromagnetic core with high permeability is usually inserted inside the coil to increase the sensitivity. The length of search coil sensors varies between $5cm$ to $150cm$, depending on the desired level of sensitivity and frequency range.

1.2.2 Fluxgate sensors

Fluxgate sensors are similar to search coil sensors in picking up the changes of magnetic field by a coil. However, they also have an excitation coil and will always have a ferromagnetic core as illustrated in Figure 1.3 [2, 4, 6–13]. As a result, the size of fluxgate sensors is on the same scale as search coil sensors. Fluxgate sensors are among the most sensitive magnetic field sensors, being able to sense fields as small as $10pT$ [2,6].

All ferromagnetic materials exhibit hysteresis. In order to sense magnetic fields, a sinusoidal current is applied to the *drive* coil to cause the core to reach its saturation magnetization once every half cycle. The *sense* coil, then, detects a nonlinearly

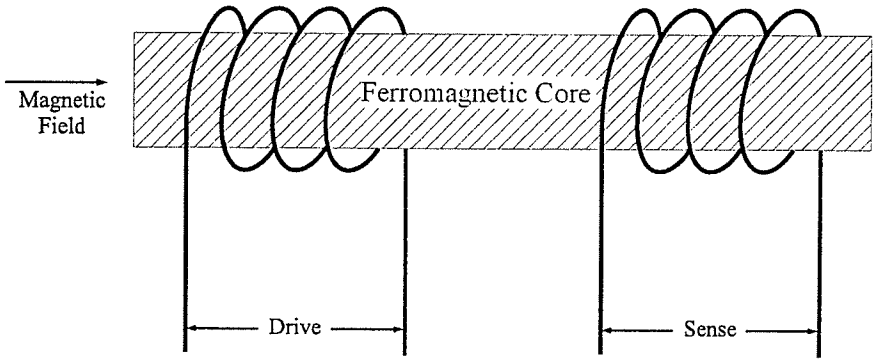

Figure 1.3: *Schematic of a fluxgate sensor.*

distorted signal. The output signal includes even harmonics of the drive signal, and most importantly, the second harmonic. Inside a magnetic field, the resistance of the core to the magnetic field (i.e., reluctance of the core) changes according to the external field strength. The strength of the magnetic field is found after processing the second harmonic of the output signal. Consequently, the signal processing electronics for fluxgate sensors are relatively complicated.

1.2.3 SQUID

The most sensitive low field magnetic sensors are the Superconducting QUantum Interference Devices (SQUID). The sensitivity of these sensors is on the order of femto-teslas [2,4,6,14,15]. The operation of SQUID is based on the work by Brian J. Josephson on the point-contact junction designed to measure extremely low currents [2]. One of the main application areas for SQUIDs is for medical imaging purposes, as the SQUID is used to measure the neuromagnetic field of the human brain, which is only a few tenths of a femto-tesla [4]. SQUIDs require cooling to very low temperatures (a few degrees kelvin) at present, but devices are under development that will operate at higher temperatures.

1.2.4 Fiber optic sensors

Dimensions of some materials, known as magnetostrictive materials, change when exposed to a magnetic field. Fiber optic sensors take advantage of this phenomenon to sense magnetic field. A piece of optical fiber is coated with a magnetostrictive material and is used as a leg of a Mach-Zender interferometer as shown in Figure 1.4. Inside a magnetic field, the length of the leg coated by the magnetostrictive material

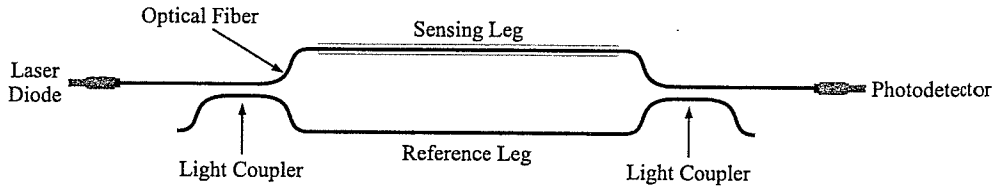

Figure 1.4: Fiber optic magnetic field sensor.

changes, which causes a phase shift between the two legs at the output light coupler [2, 16, 17]. The sensitivity of these sensors is on the order of nT, thanks to the low noise techniques used for accurate phase difference detection.

1.2.5 Other techniques

Nuclear precession magnetometers (also known as nuclear magnetic resonators) take advantage of the response to a magnetic field of nuclei of atoms in a hydrocarbon fluid [2,6]. Protons of an atom have small magnetic moments. When inside a liquid, these protons can be temporarily aligned by generating a uniform magnetic field around them using a coil. When the generated magnetic field is switched off, protons begin to precess about the ambient magnetic field. This transitional state of protons induces a signal in a coil which is a function of the strength of magnetic field. The sensitivity of these magnetic sensors is about $10pT$.

In 1896, Peter Zeeman discovered that the characteristic spectral lines of atoms split inside a magnetic field. This phenomenon is employed in optically pumped magnetometers to sense magnetic fields [2].

Magneto-optical sensors exploit another effect discovered by Faraday: the plane of polarization of a beam of light is rotated when the light travels through magnetic materials. By measuring the amount of the rotation of the polarization plane, the strength of the magnetic field can be deduced [2, 6, 18].

1.3 Integrated magnetic sensors

This section describes the operation of some of magnetic sensors that are fabricated using microelectronic or micromachining processes. It is potentially possible to integrate these transducers with electronic circuitry in one package. This could be achieved by either making the sensor and the circuit on the same chip or packaging the sensor and circuit chips together in a multi-chip module. Either way, integration often results in reduction of system cost and complexity, while improving the performance and reliability.

Many of the micromachined magnetic field sensors are essentially smaller versions of their macro-world counterparts (e.g., micromachined fluxgate sensors). However, the operation of numerous other micromachined magnetic sensors is based on new concepts that are unachievable or impractical at larger scales (e.g., tunneling and resonant magnetic field sensors).

1.3.1 Micromachined fluxgate sensors

Fluxgate sensors can be made using micromachining techniques. The sensitivity of micromachined sensors is about an order of magnitude less than the macro-world

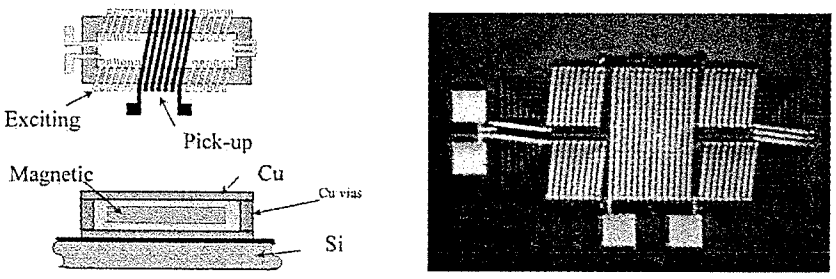

Figure 1.5: *A micromachined fluxgate sensor (after [18]).*

versions due to fabrication limitations [6,19–25]. Micromachined fluxgate sensors use either planar inductors or 3D solenoids with rectangular cross-sections for drive and sense coils. Figure 1.5 illustrates such a sensor designed by Liakopoulos et al. [21].

1.3.2 Hall sensors

Hall sensors are among the most commonly used types of magnetic field sensors [6,26–35]. The operation of the sensor is based on the exertion of a force on moving charges inside a magnetic field. The force that a particle with charge q experiences inside a magnetic field B (i.e., Lorentz force) is found from:

$$\vec{F} = q.\vec{E} + q.\vec{u} \times \vec{B} \tag{1.2}$$

where E and u are the present electric field and the velocity vector of the particle, respectively.

If a current I_x flows through a slab of conducting material inside a magnetic field (see Figure 1.6), the Lorentz force diverts the charge carriers traveling through the material towards one side of the slab according to equation 1.2. This process continues

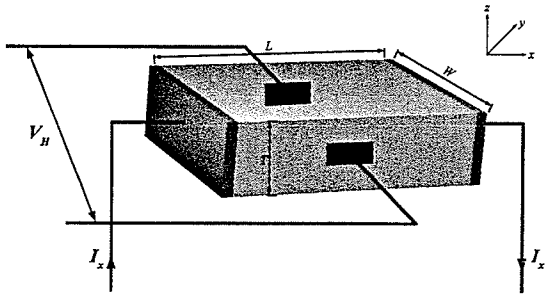

Figure 1.6: *Schematic of a Hall effect sensor.*

until the force from the electric field generated by the charges across the slab equals (and cancels) the force from the magnetic field. Therefore, a potential difference will appear across the slab which is directly proportional to the strength of the present magnetic field. For a rectangular slab as shown in Figure 1.6, it can be shown that this voltage is [6]:

$$V_H = \frac{R_H}{T} I_x B \tag{1.3}$$

where T is the thickness of the slab, I_x is the current through it, and B is the strength of the present magnetic field. R_H is the Hall coefficient which is mainly a function of the number of the charge carriers and the geometry of the sensor.

The most sensitive Hall sensors are made of InSb, a III-V semiconductor. However, sensors made of InSb require dedicated fabrication processes.

1.3.3 Magnetoresistive sensors

There are two types of magnetoresistive sensors: geometrical and physical. An external magnetic field changes the resistivity of physical magnetoresistors due to material specifications [2, 19, 36–40]. Materials such as permalloy (an alloy of nickel and iron) can be given a preferred initial magnetic orientation. Inside a magnetic field, the direction of magnetization rotates, which results in a reduction of the material's resistance as a function of magnetic field strength.

The operation of geometric magnetoresistive sensors (see Figure 1.7) is similar to Hall effect sensors [19, 41–43]. The difference is that one of the electrodes is divided in two equal segments. Without any external field, the current splits evenly between the two electrodes. When there is some external magnetic field, there will be a difference

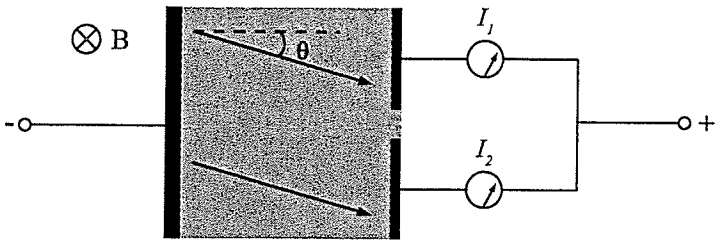

Figure 1.7: *A geometric magnetoresistive sensor.*

between the output currents from each of the segments, which is effectively as a change in the resistance seen between the electrodes.

Magnetoresistive sensors have a sensitivity range of $100pT$ to $10mT$ with proper readout electronics at temperatures between $-55°C$ and $200°C$.

1.3.4 Giant magnetoresistive sensors

The giant magnetoresistive (GMR) effect is based on the behavior of electrons traveling through a magnetic field [44–53]. It is also known that materials such as chrome, copper, and silver couple antiferromagnetically (i.e., at opposite magnetization directions) at precise film thicknesses. In such a material, electrons are scattered differently based on their spin. Typically, as many as 15 nanometer-scale alternating layers of magnetic and non-magnetic materials are stacked on top of each other and electrons are scattered in every other layer. The resistance of GMR sensors changes by as much as 20% in magnetic fields.

Closely related to the GMR effect is the giant magnetoimpedance effect (GMI), in which the impedance of a material, rather than its resistance, changes with magnetic field [50, 54–56]. GMI devices are currently under development and the technology is not as mature as GMR sensor fabrication.

GMR sensors have numerous applications in automotive industry as well as reading heads in magnetic hard drives.

1.3.5 Magnetodiodes

A magnetodiode is essentially a semiconductor diode, or pn junction [2, 57]. In a magnetodiode, however, the p region is separated from the n region by an area of undoped silicon. When the diode is forward biased, electrons are injected from the n region and holes are injected from the p region into the undoped region. Inside a magnetic field, electrons and holes are deflected in the same direction since their direction of movement is opposite to each other. The resistance of this region is a function of the amount of electron-hole recombination, which itself is a function of the external magnetic field.

The sensitivity of magnetodiode sensors is about ten times better than the response of silicon Hall effect devices. However, magnetodiode sensors require a silicon-on-insulator substrate, which makes their fabrication expensive [2].

1.3.6 Magnetotransistors

Magnetotransistors can be made in either bipolar or CMOS technologies. Magnetotransistors made in a bipolar technology are similar to npn bipolar junction transistors, but they have two similar collectors instead of one [58–62]. When exposed to an external magnetic field, charge carriers are deflected toward one of the collectors, producing a net difference between the two collector currents. Operation of magnetotransistors is based on Hall and Suhl effects. The Suhl effect takes place

when the Lorentz force is not compensated. It is possible to optimize the design of magnetotransistors to make either one of these effects dominant.

Compared to magnetodiodes, magnetotransistors are cheaper to fabricate, due to the fact that they can be made on regular silicon substrates. The sensitivity of magnetotransistors is about two orders of magnitude better than Hall effect sensors.

In case that a CMOS technology is used, the device is commonly referred to as a MAGFET [63–66]. The operation of MAGFETs is based on deflection of charge carriers in the inversion layer underneath the gate of a split-drain MOSFET. A magnetic field perpendicular to the gate of a MAGFET causes the charge carriers traveling through the inversion layer under the gate to deflect towards one of the drains. This eventually results in an asymmetry in drain currents, which is a measure of the strength of the present magnetic field.

1.3.7 Micromechanical sensors

While the initial focus was to employ the interaction of electromagnetic fields and mechanical objects for actuator applications [67–73], in recent years various concepts have been used for fabrication of micromechanical magnetic sensors. This section presents a review of some of the micromechanical sensing techniques.

An early example is the work done by Cowburn et al. [74]. Cantilevers were coated with a ferromagnetic material which magnetizes the cantilever. The cantilever, consequently, deflected inside a magnetic field. The deflections were sensed by tracking the position of a laser beam reflected from the backside of the cantilever; similar to what is done in a scanning probe microscopy (SPM) setup. Other sensing techniques (e.g., piezoresistive) may also be used to detect the deflections of the cantilever [75].

Electron tunneling is the other effect used for magnetic field sensing [76, 77]. The external magnetic field causes minute deflections of a beam or a membrane which is held at a small distance from a sharp tip. These deflections change the tunneling current between the tip and the moving object, which can be processed to extract data about the magnetic field strength.

Lorentz force is also used for magnetic field sensing applications. Generally, the exerted Lorentz force will cause a displacement of an anchored object from its equilibrium position. This displacement is then measured with different techniques. The most common method is capacitive sensing, due to its simplicity and ease of integration [78–83].

Resonating microstructures have an amplified response to the excitation signal, and can therefore provide a larger output signal. Many micromechanical sensors take advantage of this fact to improve their sensitivity or dynamic range [81–88]. These sensors use different mechanisms to bring and hold mechanical structures under resonance.

Recently, a miniature optically pumped magnetic sensor (see section 1.2.5) has been developed by researchers at National Institute of Standards and Technology [89, 90]. This sensor is a vertically stacked multi-chip module comprising of a vertical cavity surface emitting laser, a glass spacer, a neutral-density filter, a refractive microlens surrounded by an SU-8 spacer, a quartz quarter waveplate, and a neutral-density filter, rubidium vapor cell with transparent indium-tin-oxide heaters above and below it, and finally a photodiode assembly. Existence of so many layers which have to be fabricated separately and eventually assembled on top of each other makes fabrication of this device challenging. This complex structure is smaller than a grain of rice and has a resolution of $50pT$ with a $10Hz$ bandwidth.

1.4 Design of magnetic sensors

The goal of this project was to design a magnetic field sensor whose operation depended only on the geometry and mechanical properties of the sensor structure. Moreover, it was intended to not use special processing steps or non-standard materials for the fabrication of the device; i.e., the sensor could be manufactured in standard micromachining processes. Furthermore, to be able to transmit the sensor data over long distances, the data should be embedded in the frequency of the signal rather than its voltage or current. A resonating structure can be used to achieve this objective. Additionally, resonating microstructures have an amplified response (depending on quality factor of the system) to the excitation signal, and therefore, provide a larger output signal and better signal to noise ratio.

The designed sensor meets all of the above requirements. The sensor uses a mechanical resonator whose fundamental resonant frequency is modified by a force generated from the interaction of the sensor structure and the magnetic field. Electrostatic actuation is employed to bring and keep the structure under resonance and capacitive sensing is used for signal detection. The sensor is used in a closed loop as a resonator to make an oscillator whose output frequency depends on the direction and strength of the present field. The sensor is generally operated under vacuum to improve its frequency stability and to increase the signal to noise ratio of the sensor signal.

The next chapter describes the design of the sensor and the basics of its operation. The operation of the sensor involves interaction of multiple physical domains with each other: statics, dynamics, magnetostatics, electrostatics, and thermo-electromechanics. The sensor behavior is fully modeled in Chapter 3. Modeling results

from Chapter 3 are verified by finite element simulations in Chapter 4. The results of these two chapters can be used for optimization of future designs. Chapter 5 describes the three different processes which were used for fabrication of the sensors. Chapter 7 describes the electronic circuits that were designed to process the sensor signal with experimental results presented in Chapter 6. Chapter 8 discusses the noise performance of the sensor and the stability of the signal from the oscillator. The thesis concludes with remarks on future work and recommendations for improvement of the sensor performance.

Chapter 2

Design

The value of a good idea is in using it.

Thomas Edison (1847 – 1931)

In this chapter the design and operating principles of the sensor are described. Qualitative description of the sensor operation is given, followed by a closer look at different parts of the sensor and their operation as a whole.

2.1 Sensor design

A schematic of the sensor is shown in Figure 2.1. The centerpiece of the sensor is its shuttle which is the main resonating body. It also connects different parts of the sensor to each other, both electrically and mechanically. The shuttle is connected to

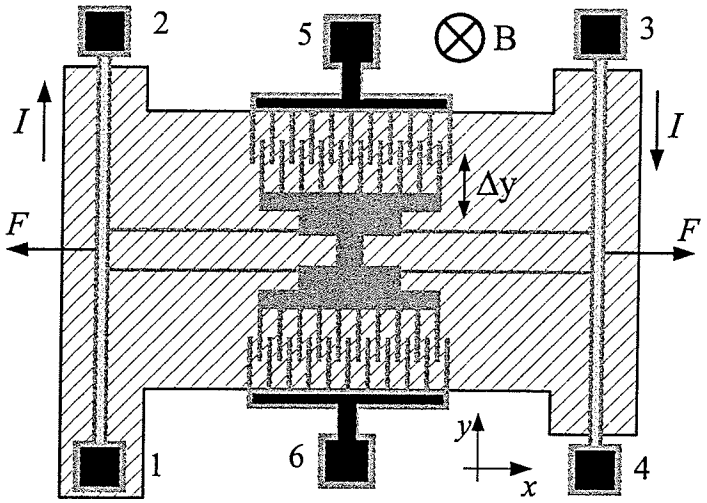

Figure 2.1: *Schematic of the sensor.*

two long crossbars by four beam springs. The flexibility of the beam springs is the most important design parameter of the device, as it directly affects the amplitude and frequency of the resonance. During the sensor operation, a current I flows through the crossbars (from pin *1* to pin *2* and then pin *3* to pin *4* on the illustrated schematic). The crossbars are designed to be much stiffer in the y direction than the x direction. The operating principle of the sensor is based on the shift in the resonant frequency of a beam under axial stress. The shuttle of the resonator is driven to and kept under resonance by means of electrostatic actuation and sensing. When the device is put inside a magnetic field, B, a force, F, is exerted on the current carrying crossbars in accordance to Lorentz's law (Figure 2.1). The distributed force on the crossbars is axially transferred to the beam springs connected to the shuttle of the resonator. This axial force alters the resonant frequency of the structure, which can be detected by the signal processing electronics. The amount of the shift in the resonant frequency of the structure is a function of magnitude of the magnetic field and its direction.

2.2 Electrostatic actuation

Various actuation methods are used in micromachined transducers, such as magnetic [69, 72], electrostatic [91, 92], thermal [93–95], piezoelectric [96], hydraulic [97], etc. Electrostatic actuation is the most popular among these methods for the following reasons:

- The steady state power requirements for electrostatic actuators are almost zero. This is due to the fact that there is no DC current flow through the comb capacitors. The AC current is also small due to the small sizes of the capacitors;
- Electrostatic actuators are easy to fabricate, either for lateral or normal displacements;
- They can be made of polysilicon or metals, which are usually available in micromachining processes;
- The same structure that is used for actuation can be used for capacitive sensing;
- They are easy to use and can be adapted to many different applications.

However, one drawback of using electrostatic actuators is the large voltages they require for operation, which itself is a consequence of the small values of the capacitances. Furthermore, micromachined electrostatic actuators are controlled by applying different voltages to the electrodes rather than directly putting a certain amount of charge on a plate. As a result, the force between two electrodes is always attractive and micromachined electrostatic actuators can only be used to *pull* and not *push*.

Electrostatic forces exist between any structures which are either charged independently from each other or proportionally (e.g., charging the electrodes of a capacitor by applying a voltage to them). The magnitude of these forces depends on the voltage difference between the objects, their geometry, and the distance between them. Electrostatic analysis of a capacitor consisting of two conductors separated by a dielectric medium is relatively straight forward. If a capacitor is charged so that a voltage difference of V appears between its electrodes, the exerted electrostatic force on the electrodes, F_V, is found from:

$$\begin{aligned} F_V &= \nabla W_e = \frac{1}{2}\nabla(CV^2) \\ &= \frac{V^2}{2}\nabla C \end{aligned} \tag{2.1}$$

where W_e is the stored potential energy on the capacitor and ∇C is the gradient of the changes in capacitance. It should be noted that the analyses to find the electric field distribution, and consequently, the forces between micromachined structures assume static field distributions everywhere. This is because the electric field generally stabilizes throughout the device at much shorter times than the mechanical response time of the structure.

Two special cases are of more importance for electrostatic actuation: (1) plates moving parallel to each other and (2) plates moving orthogonal to each other. Ignoring fringing fields, the capacitance of a parallel plate capacitor is found from $C = \epsilon A g^{-1}$, where ϵ is the dielectric constant (for air $\epsilon \approx \epsilon_0 = 8.854 \times 10^{-12} F \cdot m^{-1}$), A is the effective area of the plates, and g is the gap between the plates. Using equation 2.1,

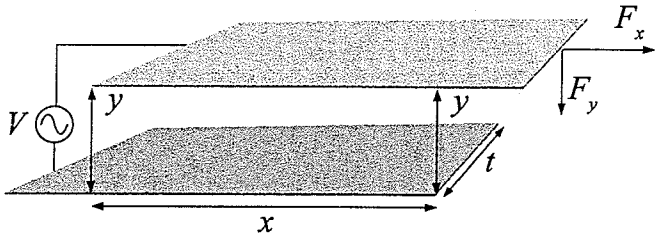

Figure 2.2: *Electrostatic forces on two parallel plates.*

for force components along x and y axes in air as shown in Figure 2.2 we have:

$$F_x = -\frac{1}{2}V^2 \frac{\partial}{\partial x}(\frac{\epsilon_0 xt}{y}) = -\epsilon_0 V^2 \frac{t}{2y} \tag{2.2}$$

$$F_y = -\frac{1}{2}V^2 \frac{\partial}{\partial y}(\frac{\epsilon_0 xt}{y}) = \epsilon_0 V^2 \frac{xt}{2y^2} \tag{2.3}$$

where t is the width of the plates. Equation 2.2 holds as long as the two electrodes cover each other (i.e., $x \gg 0$). On the other hand, equation 2.3 gives reasonable force values if the distance between the electrodes is small compared to their lateral dimensions (i.e., $y \ll x$ and $y \ll t$).

2.3 Electrostatic comb-drive

The thickness of the micromachined devices is typically on the order of micrometers. This is an advantage for moving structures which are stacked on top of each other since the gap between them can be made small (see equation 2.3). However, the electrostatic force between two neighboring structures, which are to move laterally, is directly proportional to the thickness of the structural layers. The small thickness of these structures adversely affects the practical amount of obtainable electrostatic

forces, as the lateral gaps between micromachined structures is often set by lithography. Interdigitated fingers can be used to increase the capacitance between laterally moving structures as shown in Figure 2.3. Interdigitated fingers can also be used when capacitive sensing is the method of choice for different sensory applications.

A regular comb-drive consists of at least one set of comb fingers as shown in Figure 2.3 and some sort of mechanical restoring force or stabilizing mechanism. The comb structure, in its basic or modified form, has been used in many different applications such as actuators [98, 99], microsensors [100, 101], mechanical filters [102, 103], and oscillators [104, 105].

The famous design of the electrostatic comb-drive resonators was first proposed by Howe [106] and was thoroughly investigated by Tang [107, 108]. Electronic signal processing techniques for these devices were later developed by Nguyen [109, 110]. Figure 2.4 shows a basic comb-drive resonator made from a $2\mu m$ polysilicon film. As can be seen, the device comprises of a shuttle with comb fingers on both sides of it, a set of beam springs, two fixed combs, and a ground plane. The ground plane is put underneath the moving shuttle and fingers to define the magnitude and direction

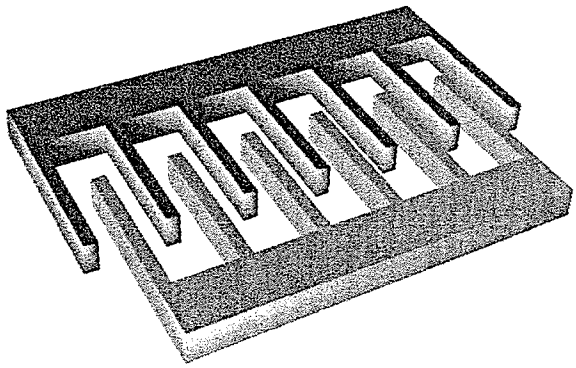

Figure 2.3: *Interdigited capacitors.*

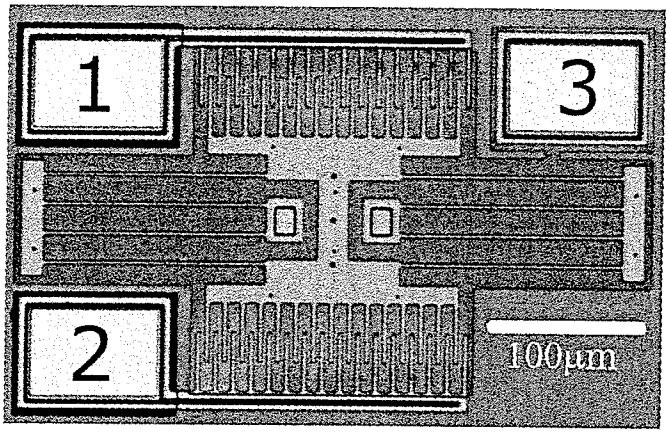

Figure 2.4: A regular comb-drive resonator.

of the electric field. It is reported that resonators without this ground plane stick down to the substrate upon application of a large DC voltage to the shuttle [111–113]. Existence of the ground plane underneath the combs makes the field distribution non-uniform which results in a generally undesirable net force in the vertical direction, and consequently, levitation of the shuttle. The arrangement of the fingers and the shape of the ground plane may be modified to reduce this levitation force [108, 114].

Figure 2.5 illustrates the expected equipotential lines around a comb structure with a ground plane underneath the combs. It can be seen that the fringing fields are *not* negligible, and therefore, the parallel plate capacitor equations must be used with care. It is suggested by Tang that the fringing fields can be accounted for if two new parameters, α and β, are introduced into the parallel plate capacitor equation as shown below [108]:

$$\frac{\partial C}{\partial y} = 2\alpha\epsilon\frac{h}{g^{\beta}} \tag{2.4}$$

where h is the thickness of the fingers and g is the distance between the fingers. Parameters α and β depend on the geometry of the comb structure and are calculated

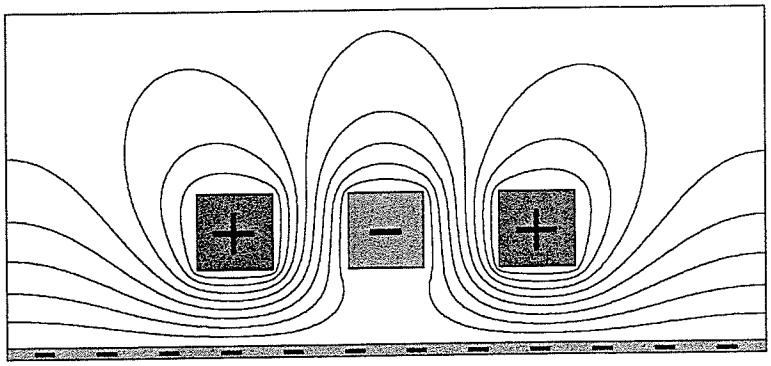

Figure 2.5: *Equipotential lines for the field around the comb fingers in presence of a ground plane.*

from curve fitting to finite element simulation results. Once electrostatic simulations are performed on a given comb geometry, the values of α and β can be derived and used for quick calculations of the value of $\partial C/\partial y$ of similar geometries (i.e., similar distance from the ground plane and finger height to gap ratio).

Depending on signal processing techniques, the stationary combs are used differently. One method is to apply the actuation voltage to one of the stationary combs, while the other comb is used to sense the amount of movement. It is also possible to apply a differential voltage to the combs and use optical methods to sense the motion. Optical sensing is relatively simpler than electrical sensing in a well equipped laboratory environment. However, electrical sensing is favored since it allows for more compact systems, possibility of integration, and simple use of feedback [108,110]. The ground plane is commonly connected to a DC voltage. The intrinsic nonlinearity of the response of the electrostatic transducers to voltage can be used for modulation purposes. If such application is intended, a combination of DC and AC voltages can be applied to the ground plane.

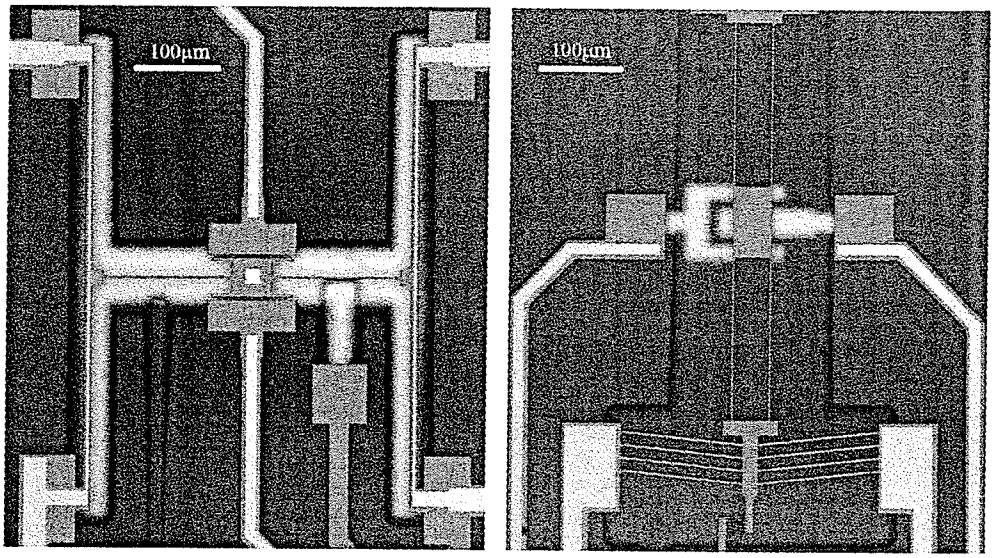

Figure 2.6: *The electrostatic transducers shown above use parallel plate capacitors for in-plane (left) and out-of-plane (right) motion.*

2.4 Parallel plate electrostatic transducers

Parallel plate capacitors are also used in micromachined devices [115]. However, the minimum distance between the structures made from the same layer in common micromachining processes is set by the lithography limits (on the order of micrometers). Consequently, the achievable amount of force for lateral movements is generally less than interdigitated structures (see equation 2.3). To circumvent this problem, novel fabrication techniques are proposed to either increase the thickness of structural layers [116, 117] or to reduce the gap between microstructures below the lithography limits [118, 119].

Parallel plate electrostatic transducers can be effectively used for out-of-plane actuation and sensing. Examples of electrostatic transducers using parallel plate capacitors for in-plane and out-of-plane movements are shown in Figure 2.6.

Chapter 3

Modeling

In mathematics you don't understand things. You just get used to them.

Johann von Neumann (1903 – 1957)

This chapter discusses the modeling of the sensor behavior under normal operating conditions. Electromechanical modeling will be done first. This change in the spring constant of beam springs under axial stress is investigated and the results of the statical analysis are used to study the dynamic behavior of the resonator. The resonant frequency of the structure is analytically derived using Dunkerley's methods. An analytic model is derived to take into account the effect of the heat generated by the current in crossbars on the performance of the sensor. The sensitivity of the sensor is finally derived by combining all of the above modeling results. Validity of the models derived in this chapter is verified with simulations in next chapter and eventually through experiments.

3.1 Electrostatic analysis

The force-voltage relationship of electrostatic actuators is nonlinear as described by equations 2.2 and 2.3. Generally, a combination of DC and AC voltages is used to drive electrostatic resonators. The DC portion has a biasing role, while the AC portion of the input voltage will determine the frequency of the mechanical oscillations.

In the case of comb-drive actuators, asymmetric DC voltages on the stationary combs may cause tilting of the shuttle due to the presence of the ground plane. This is generally undesirable as it reduces the amount of effective capacitance between the teeth and may also result in the excitation of unwanted mechanical modes during AC operation. Consequently, it is common to apply the large DC voltage to the moving shuttle (and the ground plane) instead of the stationary combs. The configuration illustrated in Figure 3.1 is used for the general electrostatic analysis of the structure. In this case, an actuation voltage $v_A = v_a \sin \omega_a t$ is applied to the actuation comb, a voltage $v_G = V_G + v_g \sin \omega_g t$ is applied to the ground blanket, and the top stationary comb is biased at V_B. The current I_{out} is the resonator's output signal and can be used to monitor the resonator behavior or to drive the resonator in a feedback loop. Note that pins *1*, *2*, *3*, and *4* are at the same potential, v_G.

The equation of motion for the mass spring system is:

$$M\ddot{y} + \zeta\dot{y} + Ky = F_{in} \tag{3.1}$$

where M is the effective mass of the vibrating structure, ζ is the damping factor, K is the effective spring constant, and F_{in} is the force applied to the structure, while $\ddot{y}$, $\dot{y}$, and y are the acceleration, velocity, and displacement of the mass, respectively. The

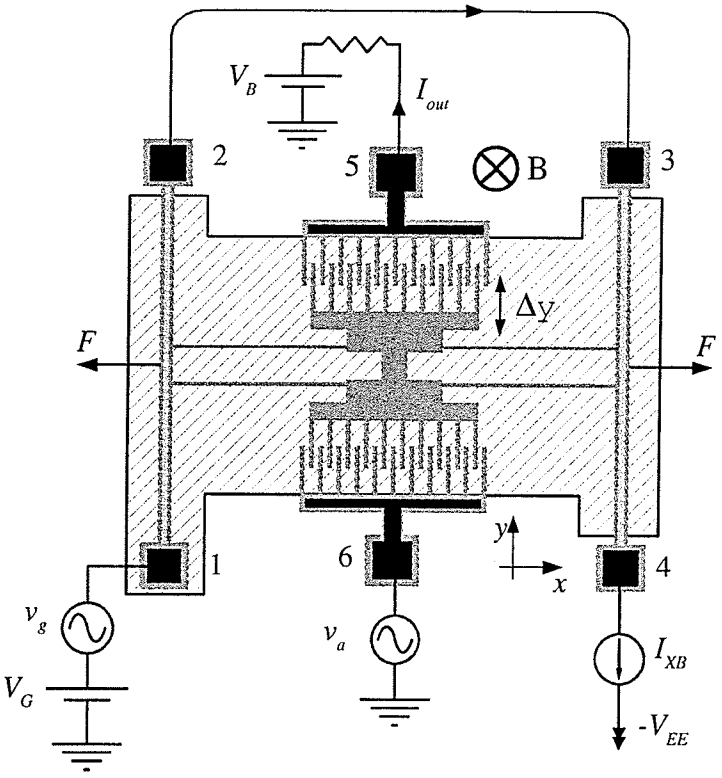

Figure 3.1: *The magnetic field sensor with the sources connected to its ports. Current I_{XB} flows through the crossbars (from pin 1 to pin 2 and then from pin 3 to pin 4). The DC voltage source V_B and V_G bias the output electrode and the ground plane, respectively, and v_a is the main input drive signal. The AC voltage source v_g may be used to modulate the output signal, I_{out}.*

spring constant K is modified by the axial force, which itself is proportional to the magnetic field flux and current I_{XB} through the crossbars. Equation 3.1 is based on the common assumption that damping in the system is proportional to the velocity of the structure.

During the sensor operation, it is kept under continuous resonance, and therefore, the analysis of the sensor response is limited to the steady state case. The transient response of the resonator is similar to that of a second order system and is ignored. For a sinusoidal input force $F_{in} = F \sin \omega t$, the steady state displacement y can be

easily found from:

$$y = \frac{F}{\sqrt{(K - M\omega^2)^2 + \zeta^2\omega^2}} \sin\Big(\omega t - \arctan\big(\frac{\zeta\omega}{K - M\omega^2}\big)\Big) \tag{3.2}$$

The force F_{in} in the equation 3.2 is from the voltages v_a, V_B, and v_G on the stationary and moving combs. Using equation 2.2 it can be seen:

$$\begin{aligned} F_{in} =& \frac{1}{2}\left(\frac{\partial C}{\partial y}\right)\left((v_A - v_G)^2 - (V_B - v_G)^2\right) \\ =& \frac{1}{2}\left(\frac{\partial C}{\partial y}\right)\left(\frac{v_a^2}{2} - V_B^2 + 2V_BV_G - 2v_aV_G\sin\omega_a t + 2v_gV_B\sin\omega_g t\right. \\ & \left. - \frac{v_a^2}{2}\cos 2\omega_a t + v_av_g\cos(\omega_a + \omega_g)t - v_av_g\cos(\omega_a - \omega_g)t\right) \end{aligned} \tag{3.3}$$

The amount of shuttle displacement is now found by combining equations 3.2 and 3.3:

$$\begin{aligned} y = \frac{1}{2}\left(\frac{\partial C}{\partial y}\right)\Bigg(& \frac{4V_BV_G - 2V_B^2 + v_a^2}{2K} \\ & - \frac{v_a^2\cos\big(2\omega_a t - \phi_{2a}\big)}{2\sqrt{(K - 4M\omega_a^2)^2 + (2\zeta\omega_a)^2}} \\ & - \frac{2v_aV_G\sin\big(\omega_a t - \phi_a\big)}{\sqrt{(K - M\omega_a^2)^2 + (\zeta\omega_a)^2}} \\ & + \frac{2v_gV_B\sin\big(\omega_g t - \phi_g\big)}{\sqrt{(K - M\omega_g^2)^2 + (\zeta\omega_g)^2}} \\ & + \frac{v_av_g\cos\big((\omega_a + \omega_g)t - \phi_{a+g}\big)}{\sqrt{\big(K - M(\omega_a + \omega_g)^2\big)^2 + \big(\zeta(\omega_a + \omega_g)\big)^2}} \\ & - \frac{v_av_g\cos\big((\omega_a - \omega_g)t - \phi_{a-g}\big)}{\sqrt{\big(K - M(\omega_a - \omega_g)^2\big)^2 + \big(\zeta(\omega_a - \omega_g)\big)^2}}\Bigg) \end{aligned} \tag{3.4}$$

where:

$$\phi_{2a} = \arctan\left(\frac{2\zeta\omega_a}{K - 4M\omega_a^2}\right)$$

$$\phi_a = \arctan\left(\frac{\zeta\omega_a}{K - M\omega_a^2}\right) \quad , \quad \phi_g = \arctan\left(\frac{\zeta\omega_g}{K - M\omega_g^2}\right)$$

$$\phi_{a+g} = \arctan\left(\frac{\zeta(\omega_a + \omega_g)}{K - M(\omega_a + \omega_g)^2}\right) \quad , \quad \phi_{a-g} = \arctan\left(\frac{\zeta(\omega_a - \omega_g)}{K - M(\omega_a - \omega_g)^2}\right)$$

Current I_{out} can be found from:

$$\begin{aligned} I_{out} &= \frac{\partial\,(CV)}{\partial t} = \frac{\partial}{\partial t}\Big(C\,(V_B - V_G - v_g \sin\omega_g t)\Big) \\ &= \left(\frac{\partial C}{\partial t}\right)(V_B - V_G - v_g \sin\omega_g t) - C\,v_g\omega_g \cos\omega_g t \end{aligned} \tag{3.5}$$

Using chain rule for differentiation, we have $\dfrac{\partial C}{\partial t} = \dfrac{\partial C}{\partial y}\dfrac{\partial y}{\partial t}$. Differentiating equation 3.4 with respect to time and inserting the result in equation 3.5 yields:

$$\begin{aligned} I_{out} =& \frac{1}{2}\left(\frac{\partial C}{\partial y}\right)^2 (V_B - V_G - v_g \sin\omega_g t) \\ & \left(\frac{v_a^2\,\omega_a\,\sin[2\omega_a t - \phi_{2a}]}{\sqrt{(K - 4M\omega_a^2)^2 + (2\zeta\omega_a)^2}}\right. \\ & - \frac{2v_a V_G\,\omega_a\,\cos[\omega_a t - \phi_a]}{\sqrt{(K - M\omega_a^2)^2 + (\zeta\omega_a)^2}} + \frac{2v_g V_B\,\omega_g\,\cos[\omega_g t - \phi_g]}{\sqrt{(K - M\omega_g^2)^2 + (\zeta\omega_g)^2}} \\ & - \frac{v_a v_g\,(\omega_a + \omega_g)\,\sin[(\omega_a + \omega_g)t - \phi_{a+g}]}{\sqrt{\left(K - M(\omega_a + \omega_g)^2\right)^2 + \left(\zeta(\omega_a + \omega_g)\right)^2}} \\ & \left. + \frac{v_a v_g\,(\omega_a - \omega_g)\,\sin[(\omega_a - \omega_g)t - \phi_{a-g}]}{\sqrt{\left(K - M(\omega_a - \omega_g)^2\right)^2 + \left(\zeta(\omega_a - \omega_g)\right)^2}}\right) - C\,v_g\omega_g \cos\omega_g t \end{aligned} \tag{3.6}$$

This equation provides the basis for electrical testing of the device.

Resonant frequency and quality factor are the two parameters that are often used when addressing the performance of resonators. Quality factor is a measure of the amount of losses during resonator operation and is defined as:

$$Q = 2\pi \frac{\text{Average stored energy}}{\text{Energy loss per cycle}} \tag{3.7}$$

Natural frequencies of a linear system are the poles of the system transfer function. The natural frequency of an undamped second order mass-spring system is given by $\omega_0 = \sqrt{\frac{K}{M}}$ where K and M are the effective spring constant and mass in the system, respectively. The driving frequency that causes maximum vibration amplitude is called the *resonant frequency*, ω_r. The relationship between the resonant frequency and the undamped natural frequency of a second order system is:

$$\omega_r = \omega_0 \sqrt{1 - \frac{1}{2Q^2}} \tag{3.8}$$

It can be seen that the two frequencies are close to each other for large values of Q. The quality factor of the micromachined devices which are analyzed in this thesis is on the order of 100 in air and 15000 in vacuum. Therefore, the resonant frequencies of these devices are nearly identical to their undamped natural frequencies.

The quality factor of a second order mechanical resonator is given by:

$$Q = \frac{M\omega_0}{\zeta} = \frac{K}{\zeta\omega_0} \tag{3.9}$$

It can further be shown that the quality factor of second order resonators can be

measured from the experimental data using the following equations:

$$Q = \frac{f_0}{\Delta f_{-3dB}} = \frac{\omega_0}{2}\frac{d}{d\omega}\angle H(j\omega) \tag{3.10}$$

where Δf_{-3dB} is the bandwidth around the resonant frequency of the device where the signal amplitude drops by $-3dB$ and $H(j\omega)$ is the transfer function of the resonator.

The shuttle displacement can be specified as a function of Q and ω_0:

$$\begin{aligned} y = \frac{1}{2K}\left(\frac{\partial C}{\partial y}\right)\Bigg(&\frac{v_a^2}{2} - V_B^2 - 2V_BV_G \\ &- \frac{v_a^2\cos\left(2\omega_a t - \phi_{2a}\right)}{2\sqrt{\left(1-\left(\frac{2\omega_a}{\omega_0}\right)^2\right)^2 + \left(\frac{2\omega_a}{\omega_0 Q}\right)^2}} \\ &- \frac{2v_aV_G\sin\left(\omega_a t - \phi_a\right)}{\sqrt{\left(1-\left(\frac{\omega_a}{\omega_0}\right)^2\right)^2 + \left(\frac{\omega_a}{\omega_0 Q}\right)^2}} - \frac{v_av_g\cos\left((\omega_a-\omega_g)t - \phi_{a-g}\right)}{\sqrt{\left(1-\left(\frac{\omega_a-\omega_g}{\omega_0}\right)^2\right)^2 + \left(\frac{\omega_a-\omega_g}{\omega_0 Q}\right)^2}} \\ &+ \frac{2v_gV_B\sin\left(\omega_g t - \phi_g\right)}{\sqrt{\left(1-\left(\frac{\omega_g}{\omega_0}\right)^2\right)^2 + \left(\frac{\omega_g}{\omega_0 Q}\right)^2}} + \frac{v_av_g\cos\left((\omega_a+\omega_g)t - \phi_{a+g}\right)}{\sqrt{\left(1-\left(\frac{\omega_a+\omega_g}{\omega_0}\right)^2\right)^2 + \left(\frac{\omega_a+\omega_g}{\omega_0 Q}\right)^2}}\Bigg) \end{aligned} \tag{3.11}$$

The output current of the resonator as a function of Q and ω_0 is given by:

$$\begin{aligned} i_{out} = &-C\,v_g\,\omega_g\cos\omega_g t + \frac{1}{2\,K}\left(\frac{\partial C}{\partial y}\right)^2(V_B - V_G - v_g\sin\omega_g t) \\ &\Bigg(\frac{v_a^2\,\omega_a\sin\left(2\omega_a t - \phi_{2a}\right)}{\sqrt{\left(1-\left(\frac{2\omega_a}{\omega_0}\right)^2\right)^2 + \left(\frac{2\omega_a}{\omega_0 Q}\right)^2}} \\ &- \frac{2v_aV_G\,\omega_a\cos\left(\omega_a t - \phi_a\right)}{\sqrt{\left(1-\left(\frac{\omega_a}{\omega_0}\right)^2\right)^2 + \left(\frac{\omega_a}{\omega_0 Q}\right)^2}} - \frac{v_av_g(\omega_a+\omega_g)\sin\left((\omega_a+\omega_g)t - \phi_{a+g}\right)}{\sqrt{\left(1-\left(\frac{\omega_a+\omega_g}{\omega_0}\right)^2\right)^2 + \left(\frac{\omega_a+\omega_g}{\omega_0 Q}\right)^2}} \\ &+ \frac{2v_gV_B\,\omega_g\cos\left(\omega_g t - \phi_g\right)}{\sqrt{\left(1-\left(\frac{\omega_g}{\omega_0}\right)^2\right)^2 + \left(\frac{\omega_g}{\omega_0 Q}\right)^2}} + \frac{v_av_g(\omega_a-\omega_g)\sin\left((\omega_a-\omega_g)t - \phi_{a-g}\right)}{\sqrt{\left(1-\left(\frac{\omega_a-\omega_g}{\omega_0}\right)^2\right)^2 + \left(\frac{\omega_a-\omega_g}{\omega_0 Q}\right)^2}}\Bigg) \end{aligned} \tag{3.12}$$

3.2 Calculation of spring constants

3.2.1 Spring constant of a beam with no axial stress

The shuttle of the resonator is connected to the crossbars by either two or four beam springs. The crossbars are much stiffer in y-direction than in x-direction by design. Moreover, their stiffness in x-direction is designed to be less than one tenth of the axial stiffness of the beam springs to minimize the probability of excitation of unwanted mechanical modes of the structure during its operation.

Euler's beam theory can be used to calculate the spring constant of beams [120, 121]. This theory assumes that the length of the beam is much bigger than its width or thickness, the beam cross-section is constant along its axis, the beam is loaded in its plane of symmetry, deformations remain small, the material is isotropic, and plane sections of the beam remain plane. These assumptions are approximately true for the beam springs of the sensor. The differential equation for finding beam deflections is:

$$\frac{\mathcal{M}}{E\mathcal{I}} = \frac{\partial^2 w}{\partial x^2}\left[1+\left(\frac{\partial w}{\partial x}\right)^2\right]^{-\frac{3}{2}} \tag{3.13}$$

where w is the deflection of the beam in y-direction, E is the Young's modulus of elasticity, and $\mathcal{M}$ is the applied moment. Parameter $\mathcal{I}$ is the second moment of inertia. The value of $\mathcal{I}$ for a beam along the x axis with deflections in xy plane is given by [121]:

$$\mathcal{I} = \int_A y^2 dA \tag{3.14}$$

For a beam with rectangular cross section of thickness b and width a the moment

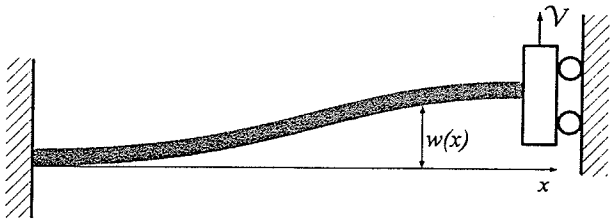

Figure 3.2: *Conceptual drawing of one of the beam springs.*

of inertia is found to be:

$$\mathcal{I} = \int_{-\frac{b}{2}}^{\frac{b}{2}} \int_{-\frac{a}{2}}^{\frac{a}{2}} y^2 dx dy = \frac{ab^3}{12} \tag{3.15}$$

For small deflections (relative to the length of the beam), it can be seen that $\left(\frac{\partial w}{\partial y}\right)^2 << 1$, and therefore, this term can be ignored. Differentiating equation 3.13, it can be seen:

$$E\mathcal{I}\frac{\partial^2 w}{\partial x^2} = \mathcal{M} \tag{3.16}$$

$$E\mathcal{I}\frac{\partial^3 w}{\partial x^3} = \mathcal{V} \tag{3.17}$$

$$E\mathcal{I}\frac{\partial^4 w}{\partial x^4} = \mathcal{F} \tag{3.18}$$

where $\mathcal{V}$ is the shearing force and $\mathcal{F}$ is the distributed load along the length of the beam. Each of the above equations may be used to calculate the deflection of a beam, depending on types of loads on a beam and boundary conditions. Boundary conditions for a beam of length L as shown in Figure 3.2 are:

$$\begin{aligned} w(0) &= 0 & w'(0) &= 0 \\ w''(\frac{L}{2}) &= 0 & w'(L) &= 0 \end{aligned} \tag{3.19}$$

Solving equation 3.17 with the above boundary conditions yields:

$$w(x) = \frac{\mathcal{V}x^2}{12E\mathcal{I}}(3L - 2x) \tag{3.20}$$

$$k_b = \frac{\mathcal{V}}{w(L)} = \frac{12E\mathcal{I}}{L^3} \tag{3.21}$$

These two equations are of great importance to electromechanical analysis of the sensor. For example, it is now possible to evaluate the value of parameter K_{eff} in section 3.1 when there is no axial load. The shuttle is connected to the crossbars by two or four of the beam springs analyzed above. Therefore, noting that beams have rectangular cross sections, the effective spring constant is $K_{eff} = N \times k_b = \frac{NEab^3}{L^3}$, where N is the number of the beam springs.

3.2.2 Spring constant of a beam under axial stress

The design of the sensor is based on the shift in the resonant frequency of the sensor structure. This is essentially due to the change in the spring constant of the beams under applied axial stress. This effect has been used for fine tuning of spring constants in other applications [122,123]. An analytic model for the spring constant can be used later on for design optimization.

The differential equation for static bending of a beam under axial stress is [120, 124]:

$$E\mathcal{I}\frac{\partial^4 w}{\partial x^4} - \mathcal{P}\frac{\partial^2 w}{\partial x^2} = \mathcal{F} \tag{3.22}$$

where $\mathcal{P}$ is the applied axial force (positive for a tensile force) and $\mathcal{F}$ is the load distributed along the beam. This equation is generally solved numerically. Approximate solutions have also been derived for this equation (e.g., by using power series) and

can be found in literature [120, 125–127]. An exact solution can be obtained for this equation for the beam-springs used in the sensor design as explained below.

We would like to calculate the bending of the beam in Figure 3.2 when an axial load is also present. The boundary conditions that we have to use are basically those given by the set 3.19. This equation can be solved for this set of boundary conditions using power series, for example. However, it can be seen that this problem is essentially the same as finding the bending of half of a bridge with a load applied to the middle of the bridge (see Figure 3.3), since: (a) bending of both structures is governed by equation 3.22 and (b) both structures satisfy the boundary conditions in 3.19 (with proper scaling of the length).

The bridge structure, however, is symmetric, and therefore, it is easier to solve the problem for a bridge. The following equation has to be solved for a bridge structure with a length $2L$, as shown in Figure 3.3:

$$E\mathcal{I}\frac{\partial^4 w}{\partial x^4} - \mathcal{P}\frac{\partial^2 w}{\partial x^2} = \mathcal{V}\,\delta(x - L) \tag{3.23}$$

where $\mathcal{V}$ is the transverse force that causes the bending (applied at distance L from the ends of the bridge; i.e., the middle of it), and δ is the Dirac impulse function, since

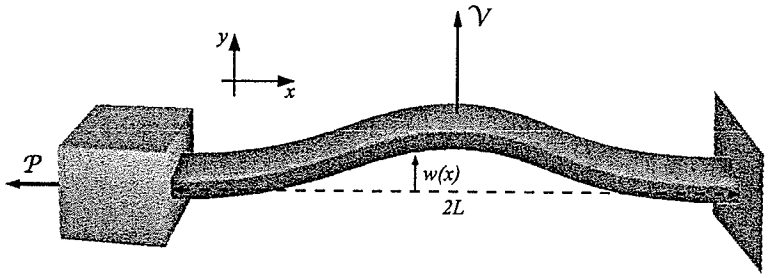

Figure 3.3: *The schematic of the bridge under axial stress.*

the load distribution is simply a point force in this case [126, 128, 129]. An excellent reference on usage and handling of singularity functions is [130].

Boundary conditions for this bridge structure are:

$$w(0) = 0 \qquad w'(0) = 0 \tag{3.24}$$

$$w(2L) = 0 \qquad w'(2L) = 0 \tag{3.25}$$

Taking the Laplace transform of both sides of equation 3.23 and applying boundary condition set 3.24 yields [131]:

$$W(s) = \frac{\mathcal{V}}{E\mathcal{I}} \times \frac{e^{-Ls}}{s^4 - \gamma^2 s^2} + \frac{As + B}{s^4 - \gamma^2 s^2} \tag{3.26}$$

where $\gamma^2 = \dfrac{\mathcal{P}}{E\mathcal{I}}$. Taking the inverse Laplace transform of the above equation and applying boundary condition set 3.25 and also noting that the amount of bending obtained from the solution for a bridge is half of that of the beam structure shown in Figure 3.2, the formula for the deflection of the beam springs is finally given by:

$$w(x) = \frac{\mathcal{V}}{E\mathcal{I}\gamma^3}\Big(\big(\cosh(\gamma x) - 1\big)\ \tanh(\frac{\gamma L}{2}) - \sinh(\gamma x) + \gamma x\Big) \tag{3.27}$$

From equation 3.27, the nonlinear spring constant is found to be:

$$k = \frac{\mathcal{V}}{w_{max}} = \frac{E\mathcal{I}\gamma^3}{\gamma L - 2\tanh\frac{\gamma L}{2}} \tag{3.28}$$

For infinitesimal values of the axial force, equation 3.27 yields the same result as equation 3.20.

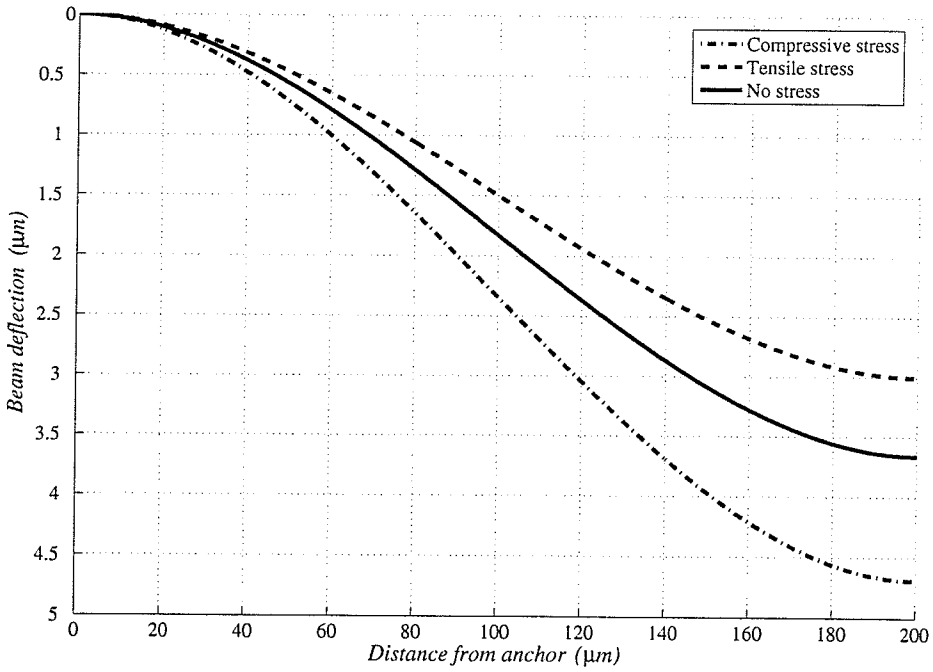

Figure 3.4: *Deflection of a beam under different axial loads.*

Deflection diagrams of a $200\mu m$ silicon beam with a $2.5\mu m \times 10\mu m$ rectangular cross section under axial forces of $-100\mu N$, 0, and $+100\mu N$ when a $10\mu N$ shearing force is applied to the free end of the beam are illustrated in Figure 3.4. As can be seen, a tensile force increases the spring constant of a beam (*stress stiffening*), while a compressive force reduces the spring constant. There are limits to the amount of both compressive and tensile forces that a beam can accept without buckling or breaking [124]. The breaking limit is set by the material properties (on the order of a few GPa for silicon). The buckling limit for a slender beam of length L can be found from Euler's beam theory [132]:

$$\mathcal{P}_{cr} = \chi \frac{\pi^2 E\mathcal{I}}{L^2} \tag{3.29}$$

where χ is a constant depending on the type of supports.

3.3 Calculation of resonant frequency

In this section the resonant frequency of the sensor is analytically calculated. Two different methods are used: Rayleigh's and Dunkerley's. Dunkerley's method was originally developed for estimating the shift in the resonant frequency of rotating shafts under different loads. This method provides a lower bound to the resonant frequency of a structure [133, 134]. Depending on the problem, using Dunkerley's method can be simpler than Rayleigh's method for the same level of accuracy. Since Dunkerley's method has not been often used for micromachined devices, the theoretical basis for the method is also provided.

Rayleigh's method is an energy method and is well known among the micromachining researchers [108, 120]. Rayleigh's method requires the mode shapes to calculate the resonant frequency of a structure. However, even relatively poor approximations to mode shapes generally yield results with acceptable accuracies [134].

3.3.1 Dunkerley's method

The equation of motion for free vibrations of a lossless mass-spring system with n masses and m springs ($m \geq n$) can be written as:

$$[M][\ddot{\vec{x}}] + [A]^{-1}[\vec{x}] = 0 \tag{3.30}$$

where $[M]_{n\times n}$ and $[A]_{n\times n}$ are the mass and flexibility matrices, respectively. Vector $[\vec{x}]_{n\times 1}$ is the displacement vector; i.e., x_i is the displacement of mass m_i. Vector $[\ddot{\vec{x}}]_{n\times 1}$ is the second derivative of the displacement vector with respect to time and represents the acceleration of the masses. To calculate element a_{ij} of the flexibility matrix, the

amount of displacement of mass i is calculated when a unit force is applied to mass j when all other force components are zero [134]. If $[A]$ and $[\vec{x}]$ are constructed this way, matrix $[M]$ will be diagonal and $m_{ii} = m_i$. It should be noted that the flexibility matrix is the inverse of the more familiar stiffness matrix $[A] = [K]^{-1}$.

For harmonic oscillations at frequency ω we have $[\ddot{\vec{x}}] = -\omega^2[\vec{x}]$. From equation 3.30, it follows that:

$$-\omega^2[M][\vec{x}] + [A]^{-1}[\vec{x}] = 0 \tag{3.31}$$

$$([A][M] - \lambda[I])\,[\vec{x}] = 0 \tag{3.32}$$

where $[I]$ is the unity matrix and $\lambda = \omega^{-2}$. The resonant frequencies of the system can be found by finding the roots, λ_i, of the characteristic equation:

$$|[A]\,[M] - \lambda[I]| = 0 \tag{3.33}$$

$$\begin{vmatrix} a_{11}m_1 - \lambda & a_{12}m_1 & \cdots & a_{1n}m_1 \\ a_{21}m_2 & a_{22}m_2 - \lambda & \cdots & a_{2n}m_2 \\ \vdots & \vdots & \vdots & \vdots \\ a_{n1}m_n & a_{n2}m_n & \cdots & a_{nn}m_n - \lambda \end{vmatrix} = 0 \tag{3.34}$$

The left side of the equation 3.34 is a polynomial of degree n, and therefore, has n roots. This equation can be rewritten as:

$$\lambda^n - (a_{11}m_1 + a_{22}m_2 + \cdots + a_{nn}m_n)\,\lambda^{n-1} + \cdots = 0 \tag{3.35}$$

It is well known from algebra that the sum of the roots of an equation is equal to the negative of the coefficient of the second highest power in that equation [134]. For

equation 3.35, we will have:

$$\sum_{i=1}^{n} \lambda_i = \sum_{i=1}^{n} a_{ii} m_i \tag{3.36}$$

From equation 3.36 and knowing that $\lambda_i = \omega_i^{-2}$ we can write:

$$\frac{1}{\omega_0^2} < \sum_{i=1}^{n} a_{ii} m_i \tag{3.37}$$

As mentioned earlier, a_{ii} is found by applying a unit force to mass i while keeping all other forces equal to zero, which effectively translates into removing all other masses from the system. If the resonant frequencies of higher modes of the system are much larger than that of the first mode, we will have:

$$\frac{1}{\omega_0^2} \approx \sum_{i=1}^{n} a_{ii} m_i \tag{3.38}$$

Equation 3.38 is known as *Dunkerley's equation.* As it is obvious from equation 3.37, Dunkerley's equation will give a lower bound on the resonant frequency of the first mode of the system.

To use Dunkerley's method, we divide the structure into beam springs, shuttle, and crossbars. However, the crossbars do not move in y-direction, and hence, act as rigid supports for the beam springs. The spring constant of a guided beam when applying a force at a distance x from its base is found by solving equation 3.18 with boundary conditions 3.19 and is given by: $12E\mathcal{I}L \times (4Lx^3 - 3x^4)^{-1}$. The resonant frequency of each of the beams is then given by:

$$\frac{1}{\omega_b^2} = \frac{\rho A}{12E\mathcal{I}} \int_0^L x^3 (4 - 3\frac{x}{L})\, dx = \frac{\rho A}{30E\mathcal{I}} \times L^4 = \frac{2M_b}{5k_b} \tag{3.39}$$

where M_b is the mass and k_b is the spring constant for each of the beams.

The shuttle will see an effective spring constant of Nk_b, where k_b is found from equation 3.28 for different values of axial force. Dunkerley's method then yields:

$$\frac{1}{\omega_0^2} = \frac{M_s}{Nk_b} + \frac{N}{\omega_b^2} \tag{3.40}$$

where ω_0 is the resonant frequency of the first mechanical mode of the structure and ω_b is the resonant frequency of each of the beams, obtained from equation 3.39 or by solving the characteristic equation for each of the beams under the axial load.

3.3.2 Rayleigh's method

Rayleigh's method is based on the fact that, at resonance, the maximum kinetic energy and the maximum potential energy are equal for linear systems. Calculating the kinetic energy of a vibrating structure requires knowledge of the mode shapes, which are generally difficult to obtain.

If $[M]$ and $[K]$ are the mass and stiffness matrices for a system, respectively, and $[\vec{x}]$ is the corresponding displacement vector for the amplitude of vibration, the maximum potential energy, U_{max}, and the maximum kinetic energy, T_{max}, are found from:

$$U_{max} = \frac{1}{2}[\vec{x}]'[K][\vec{x}] \tag{3.41}$$

$$T_{max} = \frac{1}{2}[\vec{x}]'[M][\vec{x}] = -\frac{1}{2}\omega^2[\vec{x}]'[M][\vec{x}] \tag{3.42}$$

where $[\vec{x}]'$ is the transpose of $[\vec{x}]$. Equating maximum potential and kinetic energies, it can be seen:

$$\omega^2 = \frac{[\vec{x}]'[K][\vec{x}]}{[\vec{x}]'[M][\vec{x}]} \tag{3.43}$$

Rayleigh's method gives an upper bound for the resonant frequency of a structure [134]. This is because usually a finite number of the mechanical modes are accounted for in computation of the kinetic energy of the system. Consequently, the calculated kinetic energy is less than the actual value, and as a result, the estimated resonant frequency is larger than the actual value.

Vector $[\vec{x}]$ is obtained from superposition of different mechanical modes of the structure, which may not be available. A very good way of estimating the kinetic energy is to assume that under sinusoidal excitation, the system motion is equal to a static trial function multiplied by sinusoidal time dependence [120]. If the static deflection of a structure is given by the function $y(x)$, the trial function under sinusoidal excitation will be $\hat{y}(x,t) = y(x)\cos\omega t$. The maximum velocity of the points on the beam is then given by:

$$\left.\frac{\partial\,\hat{y}(x,t)}{\partial t}\right|_{t=\frac{\pi}{2\omega}} = -\omega\,y(x) \tag{3.44}$$

This equation can now be employed to calculate the resonant frequency of the structure using equation 3.43. The closed form expression for calculation of the resonant

frequency of a structure, whose deflection is given by $y(x)$, is [134]:

$$\omega_0^2 = \frac{\int_0^L EI \left(\frac{d^2y}{dx^2}\right)^2 dx + \int_0^L \frac{EA}{4} \left(\frac{dy}{dx}\right)^4 dx}{\int_0^L y^2 \, dm} \tag{3.45}$$

The above formula, however, yields a rather sophisticated result for a beam under axial stress, and therefore, cannot serve as an easy to use design tool.

If the resonant frequencies of higher modes are required, trial functions for each of those mode shapes should be found and a procedure similar to the above should be followed [134].

3.4 Electro-thermo-mechanical effects

When passing a current through the crossbars, a certain amount of heat is generated. The generated heat affects the operation of the sensor in two ways: (1) a stress develops inside the crossbars whose ends are anchored to the substrate; and (2) the material properties, especially the Young's modulus, change with temperature. Simulations showed that the later phenomena was the dominant source of the shift in the resonant frequency of the structure as discussed in the next chapter. Modeling of the change in the resonant frequency of the sensor due to the developed stress inside the crossbars is not simple. If necessary, however, energy methods can be employed to analytically model this phenomenon. The procedure to follow is described briefly here using the Maxwell-Mohr method [121, 135, 136]. In this method, the original system is relieved from redundant constraints until it becomes statically determinate but geometrically unchanged. The modified system is called the *basic system.* A

series of forces and moments need to be applied to the system to replace the removed constraints. The strain energy of the system can now be written as a function the original and redundant forces and moments. Castigliano's theorem states that the partial derivative of the strain energy, considered as a function of the applied forces acting on a linearly elastic structure, with respect to one of these forces, is equal to the displacement in the direction of the force of its point of application. Using the results of Castigliano's theorem, all of the reactions in the system can be calculated. Next, the total strain energy of the system is found as a function of the applied loads. The final step is to relate the calculated potential energy of the system to its kinetic energy, which can be accomplished through employing Rayleigh's method.

Most of the mechanical and electrical properties of materials are temperature dependent. The properties which affect the operation of the sensor most are Young's modulus, electrical resistivity, specific heat, thermal expansion coefficient, and thermal conductivity. Modeling the effect of the change in Young's modulus due to temperature shifts is straight forward. The change in the Young's modulus of silicon as a function of temperature is given by [137–139]:

$$E(T) = E_0 \left(1 - 9.4 \times 10^{-5} T\right) \tag{3.46}$$

where E_0 is the Young's modulus of silicon at room temperature (i.e., $140GPa$) and T is the structure temperature in kelvins.

The sensor is operated under vacuum, and therefore, heat transfer through thermal conduction to the medium can be ignored. Moreover, the temperature changes are generally small (i.e., less than $100°C$) which means that the heat transfer by radiation is also negligible. Therefore, the dominant heat transfer mechanism is thermal

conduction through the arms. Temperature distribution along the crossbars can be found by solving the heat equation [140, 141]:

$$\frac{d^2T}{dy^2} = -\frac{1}{\kappa}\, q_{gen} \tag{3.47}$$

where κ is the thermal conductivity of the material in $Wm^{-1}K^{-1}$. q_{gen} is the produced heat per volume; i.e., $I_{XB}^2\, R_{XB}/(L_{XB}\, A_{XB})$, where I_{XB} is the current through the crossbars and R_{XB}, L_{XB}, and A_{XB} are the resistance, length, and cross-sectional area of the crossbars, respectively. Fabricated devices have a thin layer of gold on top of the crossbars to reduce their resistance. The large thermal conductivity of silicon causes a uniform temperature distribution in the cross section of the crossbars, although almost all of the current flows through the gold layer on silicon beams. This simplifies the problem by allowing to ignore the metal layer in thermal calculations. Solving equation 3.47 with boundary conditions $T(0) = T(L_{XB}) = T_{env}$, yields the following temperature distribution along the length of the crossbars:

$$T(y) = -\frac{1}{2}\frac{q_{gen}\, y^2}{\kappa} + \frac{1}{2}\frac{q_{gen}\, L_{XB}\, y}{\kappa} + T_{env} \tag{3.48}$$

Equation 3.48 can be used to calculate the thermally induced stress in the crossbars. The shuttle and the beam springs of the resonator will be at the same temperature as the center of the crossbars, which can be found from:

$$T_C = \frac{1}{8}\frac{I_{XB}^2\, R_{XB}\, L_{XB}}{\kappa\, A_{XB}} + T_{env} \tag{3.49}$$

In addition to Young's modulus, the resistivity, specific heat, thermal expansion coefficient, and thermal conductivity of the structural materials are generally func-

tions of temperature. However, changes of specific heat affect the transient thermal response of the sensor but have little effect on the steady state response, and therefore, are not considered here. The thermal expansion coefficient of silicon increases with temperature according to the following empirical formula for $120\,K \leq T \leq 1500\,K$ [139]:

$$\alpha_{si}(T) = 3.725 \times 10^{-6} \left(1 - e^{-5.88 \times 10^{-3}(T-124)}\right) + 5.548 \times 10^{-10}\,T \tag{3.50}$$

Variation of the thermal expansion coefficient with temperature causes the developed internal stress to be higher from the expected value when assuming a constant thermal expansion coefficient. However, as will be shown in the next chapter, the internal thermal stresses in crossbars affect the sensor performance less significantly than the changes in Young's modulus, and therefore, 10–15% of change in thermal expansion coefficient of silicon does not cause a significant error in modeling results.

The change in thermal conductivity affects the steady state thermal behavior of the structure. For temperatures between 300 and $400\,K$ the thermal conductivity of silicon increases with temperature according to [139]:

$$\kappa_{si}(T) = 309 - 0.51\,T \tag{3.51}$$

Most of the current in crossbars passes through the gold layer on top of the crossbars. The resistivity of gold for $200\,K \leq T \leq 1000\,K$ is given by [137]:

$$\rho_{au}(T) = 8.36 \times 10^{-11}\,T - 2.37 \times 10^{-9} \tag{3.52}$$

If the temperature dependence of thermal conductivity of silicon and resistivity

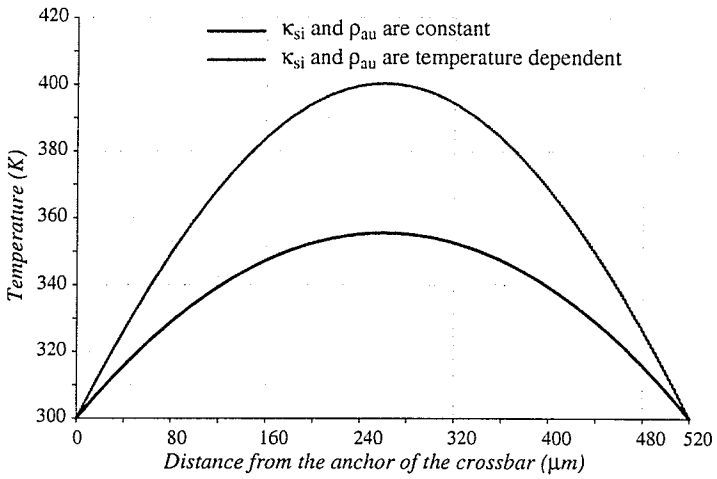

Figure 3.5: *Temperature distribution along the crossbars for a* $10mA$ *current.*

of gold are incorporated into equation 3.47, the heat equation becomes nonlinear. An analytic solution to this nonlinear heat equation could not be found. However, this equation could be solved numerically. The temperature distribution along the length of the crossbars is illustrated in Figure 3.5 for a $10mA$ current in crossbars. It can be seen that the combined effect of smaller thermal conductivity and higher resistivity at higher temperatures results in an increase in the temperature of the crossbars compared to the case where these parameters were assumed constant. The temperature at the center of the crossbar for the two cases are $400\,K$ and $356\,K$, respectively; i.e., 12% of difference in the estimated temperature.

Noticing that the model of the sensor is desired to be as simple as possible, only the temperature dependences of the Young's modulus of silicon is incorporated into the model and the other parameters are assumed to be constant with temperature. The designer, however, should bear in mind that the estimated temperature of the sensor will be less than the actual value and employ numerical simulations if necessary to investigate those effects more precisely.

3.5 Sensitivity of the sensor

The sensitivity (i.e., the amount of change in the resonant frequency as a function of the applied axial force) of the sensor can now be obtained using the mechanical parameters derived in sections 3.2 and 3.3. The sensitivity of the resonant frequency of the structure to the axial force on beam springs in $rad \cdot sec^{-1} \cdot N^{-1}$ is found from:

$$S_{\mathcal{P}}^{\omega} = \frac{d\omega}{d\mathcal{P}} = \frac{d\omega}{dk_b} \times \frac{dk_b}{d\gamma} \times \frac{d\gamma}{d\mathcal{P}} \tag{3.53}$$

The required relationships to calculate the sensitivity are all derived in sections 3.2 and 3.3 and are repeated here for convenience:

$$\omega = \sqrt{\frac{k_b}{\frac{1}{N}M_s + \frac{2N}{5}M_b}} \tag{3.54}$$

$$\gamma = \sqrt{\frac{\mathcal{P}}{E\mathcal{I}}} \tag{3.55}$$

$$k_b = \frac{E\mathcal{I}\gamma^3}{\gamma L - 2\tanh\frac{\gamma L}{2}} \tag{3.56}$$

It should also be remembered that the Young's modulus of silicon is a function of the current in the crossbars according to:

$$E(I_{XB}) = E_0\left(1 - 9.4 \times 10^{-5}\left(\frac{I_{XB}^2 R_{XB} L_{XB}}{8\,\kappa\, A_{XB}} + T_{env}\right)\right) \tag{3.57}$$

Parameter γL takes very small values for practical limits of current in crossbars, physical dimensions of the device, and magnetic field strengths. Therefore, it is valid to replace the hyperbolic tangent in equation 3.56 with its Taylor's series expansion.

Doing so, we can write:

$$\frac{d\omega}{dk_b} = \frac{1}{2\sqrt{k_b.(\frac{1}{N}M_s + \frac{2N}{5}M_b)}} \tag{3.58}$$

$$\frac{d\gamma}{d\mathcal{P}} = \frac{1}{2\sqrt{\mathcal{P}E\mathcal{I}}} \tag{3.59}$$

$$\begin{aligned}\frac{dk_b}{d\gamma} &= \frac{d}{d\gamma}\left(\frac{E\mathcal{I}\gamma^3}{\gamma L - 2\,(\frac{\gamma L}{2} - \frac{(\gamma L)^3}{24} + \frac{(\gamma L)^5}{240})}\right) \\ &\approx \frac{12E\mathcal{I}\gamma}{5L} - \frac{E\mathcal{I}L\gamma^3}{175} + \frac{E\mathcal{I}L^3\gamma^5}{10500}\end{aligned} \tag{3.60}$$

Ignoring the nonlinear terms in equation 3.60, the sensitivity of the sensor is:

$$S^{\omega}_{\mathcal{P}} = \left(\frac{1}{2\sqrt{k_b.(\frac{1}{N}M_s + \frac{2N}{5}M_b)}}\right) \cdot \left(\frac{1}{2\sqrt{\mathcal{P}E\mathcal{I}}}\right) \cdot \left(\frac{12E\mathcal{I}}{5L}\sqrt{\frac{\mathcal{P}}{E\mathcal{I}}}\right) \tag{3.61}$$

which simplifies to:

$$\begin{aligned}S^{\omega}_{\mathcal{P}} &= \frac{3}{5L\sqrt{k_b.(\frac{1}{N}M_s + \frac{2N}{5}M_b)}} \\ &= \frac{3}{5ab^2} \times \sqrt{\frac{1}{\rho E}} \times \sqrt{\frac{1}{\frac{A_s}{NbL} + \frac{2N}{5}}}\end{aligned} \tag{3.62}$$

where a, b, and L are the thickness, width, and length of the spring beam, respectively and A_s is the area of the shuttle. This relationship indicates that the resonant frequency of the structure increases with a tensile force and also predicts a practically linear response for the sensor.

Noting that a distributed load along the crossbars exerts the axial force to the beam springs, it can be seen that $|\vec{\mathcal{P}}| = \frac{1}{N} I_{XB} |\vec{L}_{XB} \times \vec{B}|$ and the sensitivity of the

sensor to present magnetic fields can be obtained. For a magnetic field normal to the plane of the sensor, the sensitivity in rad/T is given by:

$$\begin{aligned} S_B^{\omega} &= \frac{3\, I_{XB}\, L_{XB}\, \omega_0}{5\, N\, L\, k_b} \\ &= \frac{3\, I_{XB}\, L_{XB}}{5Nab^2} \times \sqrt{\frac{1}{\rho E}} \times \sqrt{\frac{1}{\frac{A_s}{NbL} + \frac{2N}{5}}} \end{aligned} \tag{3.63}$$

To account for the changes in material properties with temperature, the value of the Young's modulus from equation 3.57 should be used in equations 3.63 and 3.62. The changes in resonant frequency and sensitivity of a sensor for various values of magnetic field are illustrated in Figure 3.6. The modeled device has a shuttle with a mass of $190.8ng$ which connected to two $520\mu m$ crossbars with two $200\mu m \times 2.5\mu m$ beam springs. (device d in Table 4.1). The current in crossbars is assumed to be $10mA$ and the device layer thickness is $10\mu m$.

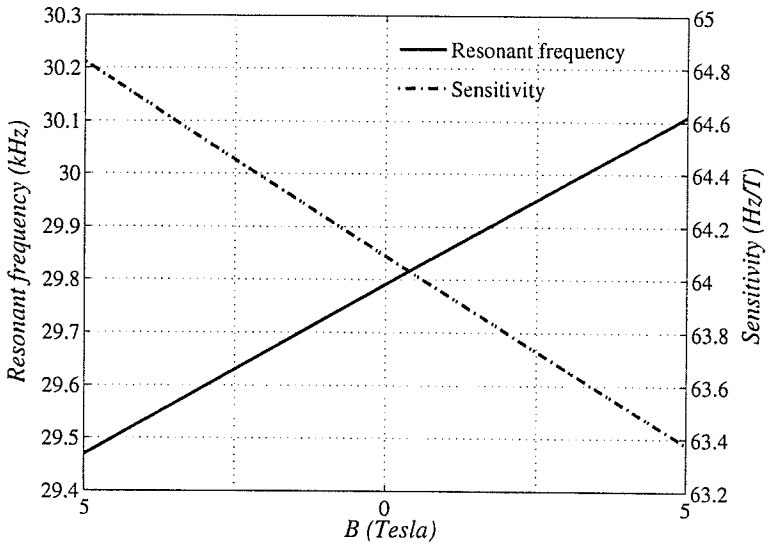

Figure 3.6: *Resonant frequency and sensitivity of a sample sensor for a crossbar current of* $10mA$.

3.6 Modeling of damping

Numerous damping mechanisms can contribute to energy loss in micromachined resonators. The friction between the micromachined structure and the gaseous environment is one source of loss as is the coupling of resonator energy to the substrate through anchors. In addition to air damping, there are other sources of energy loss in micromachined structures (e.g., thermoelastic and through-anchor losses). For example, the irreversible conversion of elastic energy to heat (thermoelastic loss) is another source of loss that one may need to consider. The transfer of energy between a resonating structure and phonons or the photons impinging on the surface of a micromachined structures also contribute to the total losses in the system. All of these sources contribute to the total losses in the system, and will therefore, damp the signals. However, the overall effect of these sources is much less than air damping at normal operating pressure ranges for resonators with moving parts (in contrast to bulk-mode resonators).

Various methods have been used to model the damping mechanisms in micromachined devices. *Couette* and *squeezed-film* damping effects are the two common types of damping models used when dealing with micromechanical structures with moving parts whose dimensions are on the order of 10's of micrometers. Both Couette and squeezed-film damping models are derived from solving the Reynold's equation under different boundary conditions [142–148]. This equation is valid as long as the gap between the structures is much smaller than their dimensions, there is no pressure gradient between the plates, the temperature across the plates is uniform, the gas is ideal, the inertial forces are smaller than viscous forces, the velocity of the surface is

low enough to prevent the heating of the gas, and the amplitude of the oscillation is small compared with the length of the surface.

If the gap between two plates sliding past each other does not change, the damping mechanism is said to be of Couette type. The source of this damping mechanism in classical mechanics is the required energy for shaping the gas flow between the sliding structures. The formula that is often used for extracting a frequency independent Couette damping factor for laterally moving micromachined structures is [108, 149–151]:

$$\zeta_c = \eta_{eff} \frac{A}{g} \tag{3.64}$$

where η_{eff} is the effective viscous coefficient of the gas ambient surrounding the resonator ($\eta_0 = 1.78 \times 10^{-5}\, kg{\cdot}m^{-1}{\cdot}sec^{-1}$ for air at atmospheric pressure), A is the surface area of the moving structure, and g is the gap between the moving and fixed substrate. As expected, η_{eff} depends on the gas pressure. Solving the gas dynamic equations and using experimental data, it has been shown that [152]:

$$\eta_{eff} = \frac{\eta_0}{1 + 2\,K_n + 0.2\,K_n^{0.788}\, e^{-0.1 K_n}} \tag{3.65}$$

where K_n is the Knudsen number which is the measure of the rarefaction effect. It is the ratio of the mean free path of the ambient gas molecules, λ, and the gap between the structures: $K_n = \frac{\lambda}{g}$. The value of the mean free path can be calculated from [153]:

$$\lambda = \frac{K_B\, T}{\sqrt{2}\,\pi\, d^2 P_{env}} \tag{3.66}$$

where K_B is Boltzmann's constant ($1.3806 \times 10^{-23} J/K$), T is the ambient temperature in kelvin, P_{env} is the pressure, and d is the diameter of gas molecules.

Couette damping decreases almost linearly for devices that are vibrating at frequencies higher than a cutoff frequency given by [154]:

$$f_{cc} = \frac{\eta_{eff}}{2\pi\, g^2\, \rho} \tag{3.67}$$

where ρ is the gas density.

If the gap between the moving structures changes during their movement, another damping mechanism known as squeezed-film damping will occur [142, 155–157]. This damping is a result of the energy required to push the ambient gas out of the gap between two structures when they move toward each other. Squeezed-film damping can be calculated from [142]:

$$\zeta_{sf} = \frac{96}{\pi^4} \times \frac{\eta_{eff}\, L\, W^3}{g^3} \tag{3.68}$$

where L is the length of the moving beam, W is its width, and g is the gap between structures. It can be seen that, similar to Couette damping, squeezed-film damping is a function of ambient gas pressure. Squeezed-film damping coefficient is constant for low frequencies up to a cutoff frequency that is given by [142]:

$$f_{cs} = \frac{\pi\, g^2\, P_0}{24\, \eta_{eff}\, W^2} \tag{3.69}$$

where P_0 is the pressure between the structures at their rest position. The squeezed-film damping coefficient drops with frequency for frequencies higher than f_{cs}.

Chapter 4

Simulation

94.5% of all statistics are made up.

Woody Allen

Different types of simulations were performed to predict the device performance. Simulations were also used to verify the modeling results and to validate the assumptions made during the modeling of the device. Moreover, simulations provided insight into aspects of the device performance whose modeling was not possible or did not yield an easy-to-use result (e.g., the effect of the stress in crossbars on the resonant frequency of the device).

ANSYS was used to perform the finite element simulations [158]. ANSYS is quite flexible in terms of meshing options and types of elements. ANSYS Parametric Design Language (APDL) can be used to quickly build models for different simulations with full control on simulation parameters.

Table 4.1: Structural material properties.

Device	*a*	*b*	*c*	*d*
	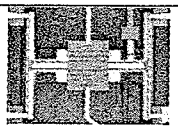	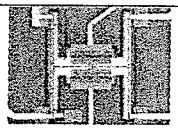	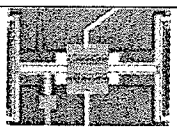	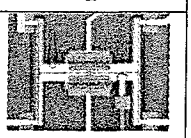
Number of springs	4	2	4	2
Length of springs	$150\mu m$	$150\mu m$	$200\mu m$	$200\mu m$
Width of springs	$3\,\mu m$			
Number of fingers	15			
Finger $L \times W$	$35 \times 3\,\mu m^2$			
Finger gap	$2.5\,\mu m$			
Crossbar $L \times W$	$520 \times 9\,\mu m^2$			

Table 4.2: Physical dimensions of the micromachined structure used in simulations.

Material	**Silicon**	**Gold**
Young's modulus (MPa)	140×10^3	75×10^3
Poisson's ratio	0.22	0.42
Density $(kg\,\mu m^{-3})$	2.33×10^{-15}	19.3×10^{-15}
Thermal conductivity $(pW\,\mu m^{-1}\,{}^{\circ}K^{-1})$	150×10^6	315×10^6
Thermal expansion coefficient	2.9×10^{-6}	14.2×10^{-6}
Resitivity $(\Omega\,\mu m)$	112×10^{-9}	92.3×10^{-15}

The simulations were performed on models based on the fabricated devices. Physical dimensions of the fabricated devices are summarized in Table 4.1 along with their optical images. The material properties as used for modeling and simulations of the devices are listed in Table 4.2 in $\mu MKSV$ system of units (i.e., SI units scaled for ease of use for analysis of MEMS in ANSYS) [159, 160]. The simulation codes for all of the analyses in this chapter are listed in Appendix B.

Most of the simulations were performed in one physical domain (e.g., mechanical or electrostatic) to avoid the complexities of setting up multiphysics simulations. However, electro-thermo-mechanical effects were simulated in the multiphysics domain due to the continuous interactions of electric, thermal, and statical domains.

The simulations were used to investigate the performance of all of the fabricated devices. However, most of the illustrations in this chapter correspond to devices a and d. The reason for choosing these two devices is that device a has the stiffest structure with the smallest sensitivity and the highest resonant frequency among the tested devices, while device d has the most flexible structure and is also the most sensitive device with the lowest resonant frequency.

4.1 Electrostatic simulation

The first parameter that is needed to analyze the behavior of an electrostatic actuator is the rate of the change in capacitance between the electrodes. To calculate this parameter, the capacitance of the comb structure was calculated for different finger engagements and the rate of the change in capacitance was interpolated from that data. To perform the electrostatic simulation the structure is constructed first. The air volume that fills the space between the mechanical structures is then created and meshed. A large enough air volume has to surround the structure to account for the fringing fields. Figure 4.1 illustrates the results of the electrostatic simulations on a pair of the combs used in the structure of the devices. The comb attached to the shuttle has fifteen $35\mu m \times 3\mu m$ fingers with a $2.5\mu m$ gap between the fingers and an initial finger engagement of $15\mu m$. About $20,000$ 20-node brick elements were used for building of the FE model.

ANSYS has the capability to solve an electrostatic problem with the assumption that the ground is at infinity. The technique is called Trefftz method and simply closes the FEM region far enough by an artificial Dirichlet boundary condition [158].

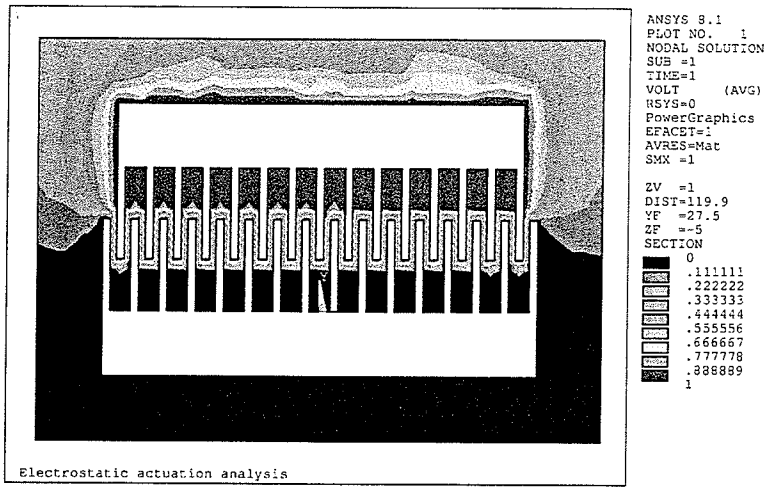

Figure 4.1: *Electric potential distribution in the space between the fingers (cross sectional top-view). The applied voltage between the combs is* $1V$.

The comb structure was modeled with different air volumes and it was found out that a box extending $25\mu m$ beyond the edges of the structure results in the same degree of accuracy as the Trefftz method without dealing with additional steps required for using the Trefftz method.

Existence of a ground plane in the actual device makes the effect of the fringing fields more prominent. As can be seen in Figure 4.2, the field distribution above and below the combs is not symmetric due to the effect of the ground plane. As discussed

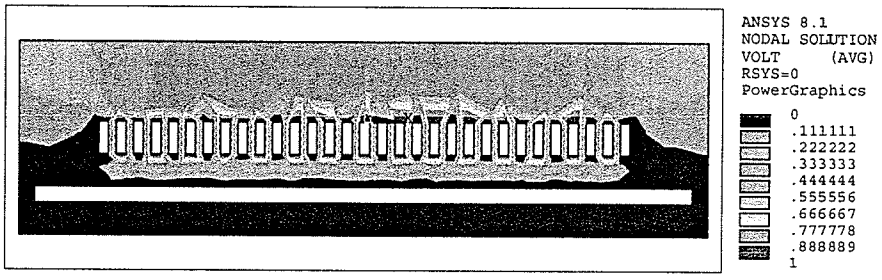

Figure 4.2: *Electric potential distribution above and below the combs.*

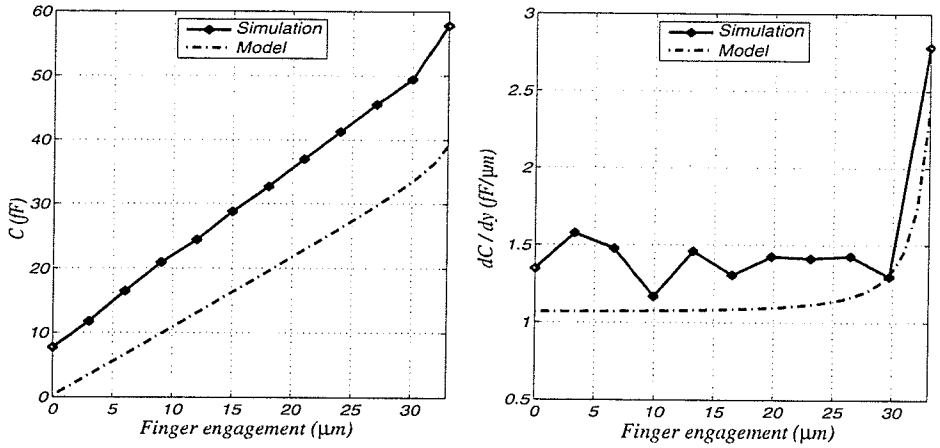

Figure 4.3: *The changes in capacitance as a function of finger engagement.*

before, the ground plane is required to be able to produce a predictable field around the combs. However, the asymmetry caused by the ground plane will push the shuttle of the comb-drive out of plane of motion, which may lead to instabilities during sensor operation at high frequencies. Methods to compensate for the effect of the ground plane are discussed in [108, 114]. Devices made in MicraGEM process, however, are not affected significantly by the asymmetry in electric fields thanks to the large gap between the substrate and the shuttle and the relatively large thickness of the structural layer in this process (i.e., $10\mu m$), which causes the structures to be stiff in the direction normal to the substrate.

The CMATRIX macro in ANSYS was then used to calculate the capacitance between the electrodes. After the electrostatic simulation of the structure is completed, CMATRIX executes a series of solutions to compute self and mutual capacitance between conductors. The simulation and modeling results for the capacitance between the combs and also the rate of the change in capacitance versus finger engagement are compared in Figure 4.3.

4.2 Mechanical simulation

The statical simulation of the structure aids in estimation of the spring constants and the amount of deflections and displacements. Modal analysis can then be used to estimate the resonant frequencies of different mechanical modes of the structure. Transferring the results from the static simulation to modal simulation allows for investigation of the changes of the resonant frequency of the structure under different loading conditions. This technique was used to calculate the sensitivity of the sensors.

4.2.1 Statical simulation

The electrostatic force on the shuttle of the sensor between the combs can be calculated using the results from electrostatic simulations (section 4.1). For a voltage V between the combs, the force can be calculated from:

$$F_{es} = \frac{1}{2}\frac{\partial C}{\partial y}V^2 \tag{4.1}$$

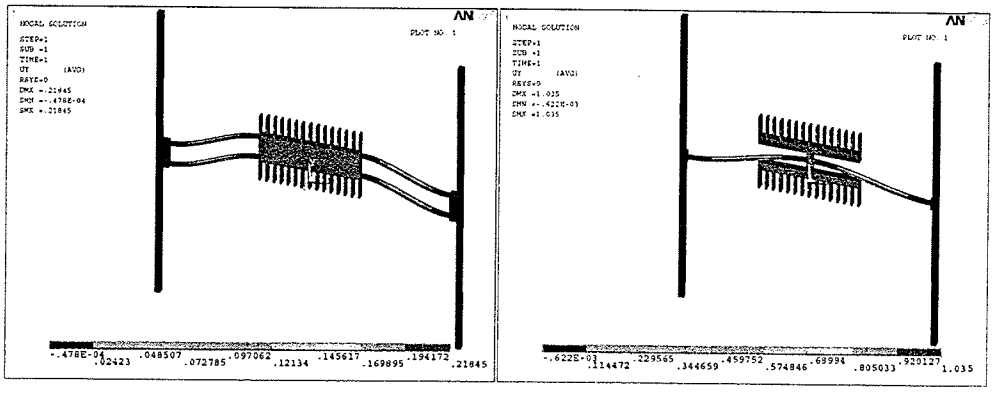

Figure 4.4: Static deflection of devices a and d for a 100V actuation voltage.

This electrostatic force is then applied to the ends of the fingers of the shuttle and the simulation is run to find the amount of the deflections. Figure 4.4 illustrates the static deflections of devices a and d for a $100V$ voltage difference between the combs.

4.2.2 Modal simulation

The resonant frequencies of different mechanical modes of the unloaded structure can be estimated by modal simulation. The model in Section 3.3 does not provide the means for the estimation of higher mode resonant frequencies. However, knowledge about different modes of the structure is required to prevent undesirable device

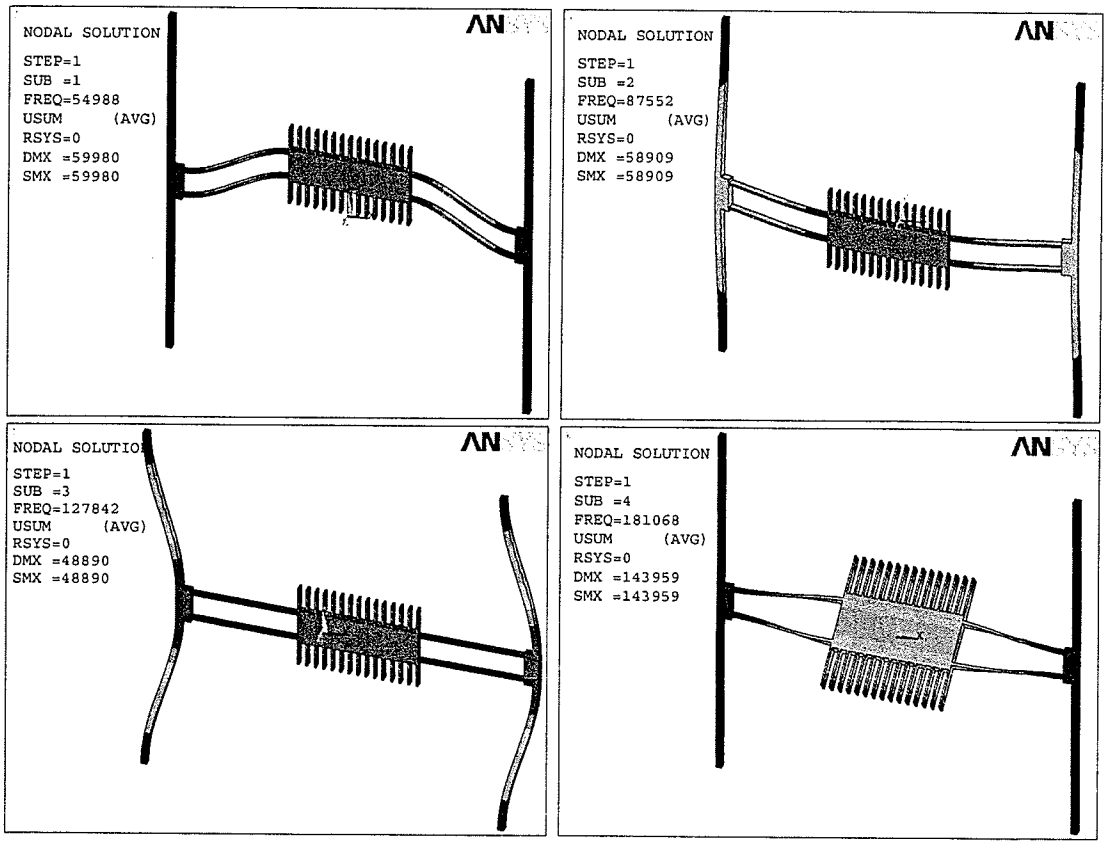

Figure 4.5: *The first four mechanical modes of device a.*

behavior during its operation. For example, if the resonant frequency of a higher mode of a device is close to its operational resonant frequency (i.e., resonant frequency of its first mode), that mode can be excited during the sensor operation and cause malfunctioning. The first four resonant modes of device a are illustrated in Figure 4.5, with resonant frequencies of $54.988kHz$, $87.552kHz$, $127.840kHz$, and $181.070kHz$, respectively. The resonant frequencies of the first four modes for device d are $29.612kHz$, $59.991kHz$, $61.808kHz$, and $72.837kHz$.

4.2.3 Simulation of the sensitivity

The sensitivity of the devices was simulated by combining the statical and modal analyses (Figure 4.6). Each device is first statically simulated with all of the external loads applied to it (i.e., electrostatic and magnetostatic forces). The magnetostatic force is applied as a distributed load along the length of the crossbars. After each

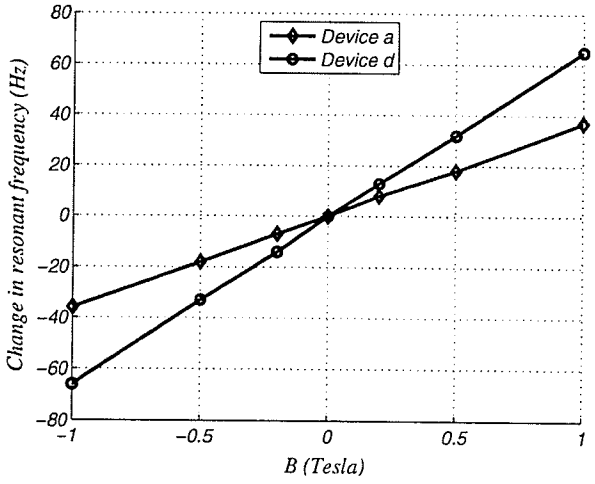

Figure 4.6: *Comparison of the change in resonant frequencies of the devices a and d versus the strength of the magnetic field.*

static analysis, the results are saved and passed to the modal analysis simulator to calculate the resonant frequency of the stressed structure. The shift in the resonant frequencies of devices a and d are compared in Figure 4.6 for a $10mA$ current in their crossbars.

4.3 Simulation of thermal effects

As discussed in Section 3.4, when a current passes through the crossbars, it heats them up. A coupled-field FE simulation can be performed to find out the rise in temperature due to the current in crossbars. The model is based similarly to what was done in Section 4.2 with the difference that the metal layer is added on top of the crossbars. The boundary conditions for this coupled-field problem include the mechanical support, electrical potentials, and the substrate temperature at the ends of the crossbars. The elements used to build the FE model have thermal, electrical, and mechanical degrees of freedom. Figure 4.7 illustrates the simulation results for temperature distribution in the cross section and along the crossbars for a $2mA$ current. The modeling results compare quite well with the simulation results and predict a $2.31°C$ rise in the temperature of the shuttle for this current. The simulation results justify the simplifying assumptions made during the electro-thermal modeling of the structure; i.e., neglecting the metal layer and assuming a constant temperature across the cross sections of the crossbars.

4.4 Resonant frequency shift due to thermal stress

As discussed in Chapter 3, the Joule heating from the current in crossbars affects the resonant frequency of the device through the the changes in material properties

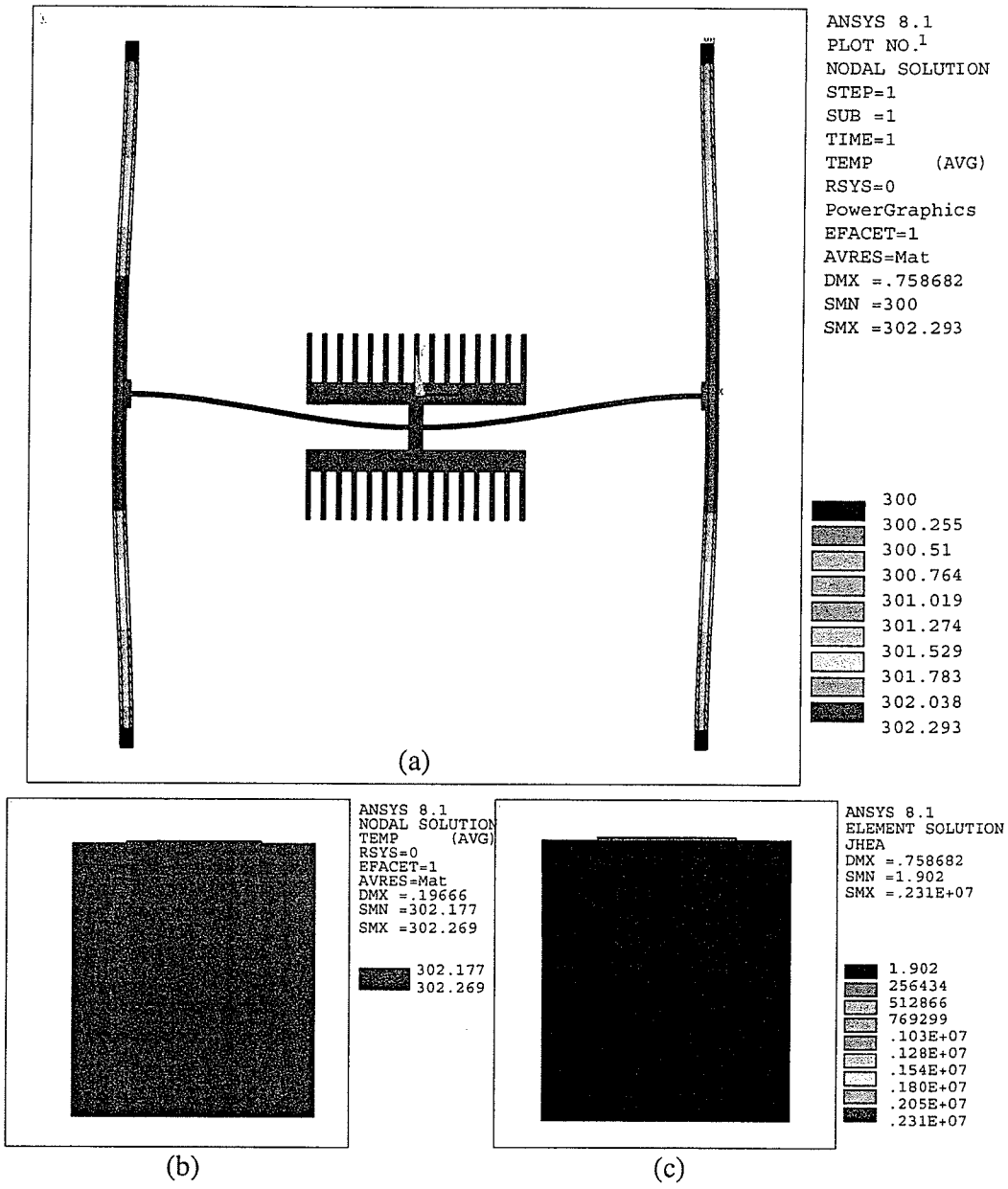

Figure 4.7: *Thermo-electro-mechanical simulation results. Figure 4.7-(a) shows the temperature distribution over the device structure, Figure 4.7-(b) depicts the temperature distribution at a cross section of the crossbar, and Figure 4.7-(c) illustrates the amount of Joule heating at the same cross section.*

and stresses that develop in the crossbars. The change in material properties was analytically modeled in Section 3.4. However, it was decided to leave the investigation of the shift in resonant frequency from the developed thermal stress in crossbars to simulations.

The effect of thermal stress in the crossbars can be analyzed by transferring the results from the thermal analysis of the structure to the modal simulations. The temperature gradient between the heated structure and the substrate, which is assumed to be at a constant temperature, causes a thermal stress in crossbars. If one end of the crossbars was free to move, they would expand due to the increase in the temperature. The amount of the change in their length can be calculated using the results from equation 3.48:

$$\begin{aligned}\Delta L_{XB} &= \int_0^{L_{XB}} dL = \int_0^{L_{XB}} \alpha\,(-\frac{1}{2}\frac{q_{gen}\,y^2}{\kappa} + \frac{1}{2}\frac{q_{gen}\,L_{XB}\,y}{\kappa})\,dy \\ &= \frac{1}{12}\frac{\alpha\,q_{gen}\,L_{XB}^3}{\kappa}\end{aligned} \tag{4.2}$$

or if the generated heat per volume, q_{gen}, is specified in terms of the current in crossbars:

$$\Delta L_{XB} = \frac{\alpha\,I_{XB}^2\,R_{XB}\,L_{XB}^2}{12\,\kappa\,A_{XB}} \tag{4.3}$$

where α is the coefficient of thermal expansion, κ is the thermal conductivity, and A_{XB} is the cross sectional area of the crossbars.

Since both ends of the crossbars are anchored to the substrate, a stress has to develop inside the beam to keep its length unchanged. Noticing that the axial spring constant of the crossbars is $k_a = E(T_C)\,A_{XB}\,L_{XB}^{-1}$, the thermally induced stress is

Table 4.3: *Simulation results for the shift in the resonant frequency of devices a and d (in Hz) due to the change in material properties (column $E(T)$), the thermally induced stress (column σ_{th}), and both phenomena together.*

		Device a			Device d		
Current	**Temperature rise**	$E(T)$	σ_{th}	**Both**	$E(T)$	σ_{th}	**Both**
$0\,mA$	$0\ ^{\circ}C$	54988			29612		
$1\,mA$	$0.578\ ^{\circ}C$	54987	54988	54986	29611	29611	29610
$5\,mA$	$14.44\ ^{\circ}C$	54951	54977	54939	29591	29601	29581
$10\,mA$	$57.78\ ^{\circ}C$	54839	54942	54792	29531	29568	29488

found from:

$$\sigma_{th} = -\frac{k_a\,\Delta L_{XB}}{A_{XB}} = -\frac{\alpha\,E(T_C)\,I_{XB}^2\,R_{XB}\,L_{XB}}{12\,\kappa\,A_{XB}} \tag{4.4}$$

where the negative sign implies a compressive stress.

Simulations were performed to investigate the effects of the thermally induced stress as well as the change in material properties on the resonant frequency of the device. The temperature rise due to passing of a certain amount of current through the crossbars was calculated. Three separate static simulations were performed for each value of the current in the crossbar. At first, only the change in material properties was considered. In the second simulation, only the thermally induced stress was applied as a load to the structure. Finally, both effects were considered simultaneously and appropriate loads were applied. The developed internal stresses from statical simulations were then used in setting up the FE model for modal simulations and the resonant frequencies of the devices under stress were calculated. Simulation results for devices a and d are compared in Table 4.3. As can be seen, the change in material properties causes a larger change in the resonant frequency of the device than the thermally induced stress.

Chapter 5

Fabrication

It is a fundamental fact of life that first steps in experimentation are bound to fail.

Philip R. Bevington

Various techniques have been investigated for fabrication of magnetic sensors, either in-house or in a standard process. Details of each of the process steps can be found elsewhere in literature [19, 108, 120, 124, 153, 161]. Some of the devices were fabricated at the NanoFab laboratory at the University of Alberta on silicon-on-insulator (SOI) wafers. The device designs were also adjusted for fabrication through two MEMS fabrication processes offered by companies outside the university: MUMPs from MEMSCAP Inc. and MicraGEM from Micralyne Inc. Access to both of these fabrication processes was made possible through services provided by Canadian Microelectronic Corporation (CMC).

5.1 Fabrication on SOI wafers

The sensor design was fabricated with a single mask process on SOI wafers. The process flow is illustrated in Figure 5.1. The use of SOI wafers in this process greatly simplified the process flow. Details of process steps are given in Appendix A.

The SOI wafers had a $5\mu m$ device layer (silicon) on top of a $2.5\mu m$ buried oxide layer (step *a* in Figure 5.1). The process starts by cleaning the wafers in a piranha etch solution. Photoresist is spun on top of the device layer and patterned. The top silicon layer is etched in a deep reactive ion etching (DRIE) system using the photoresist as the masking layer (step *b* in Figure 5.1). Polymerized photoresist is then removed in a piranha etch solution. The buried oxide layer is etched in a 50% buffered hydrofluoric (BHF) acid solution. The wafers are then transfered to a critical-point drying system to avoid stiction of the released structures to the substrate (step *c* in Figure 5.1). A device made with this process flow is shown in Figure 5.2

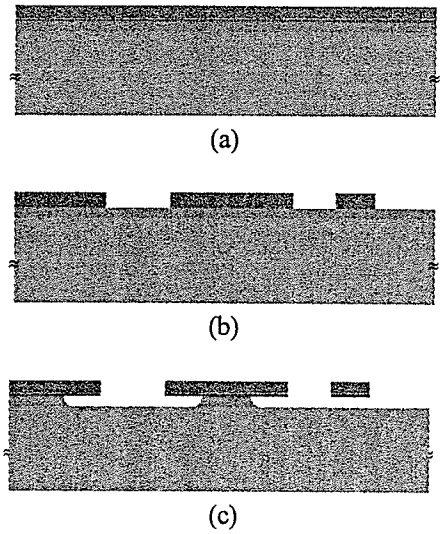

Figure 5.1: *SOI fabrication process steps: (a) wafer preparation, (b) DRIE of the device layer, and (c) buried oxide removal.*

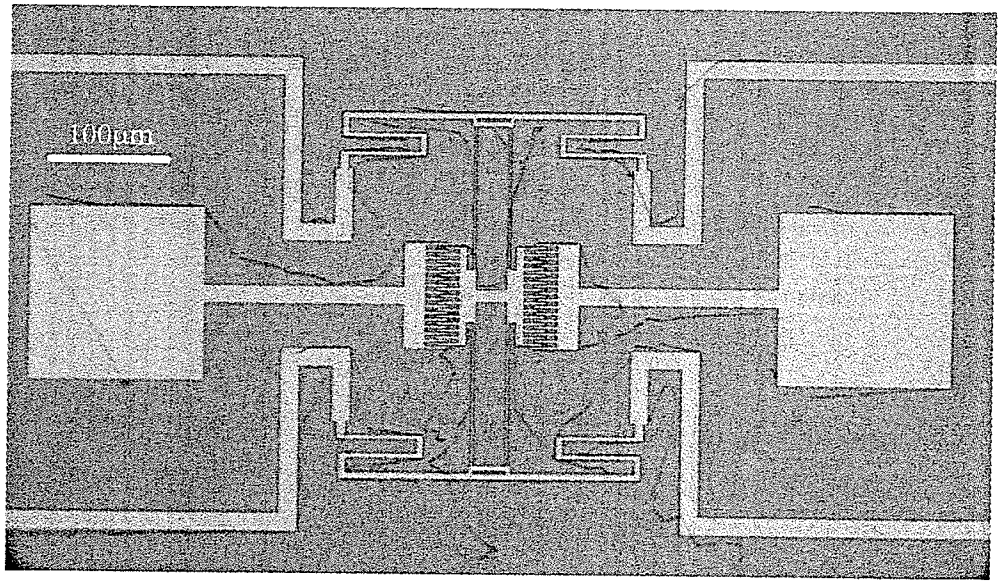

Figure 5.2: *Optical image of a sensor made by the SOI process. The hair like strands are released pieces of silicon dioxide after removal of the buried oxide layer.*

These devices eventually failed to operate as expected. The reason for failure was delamination of the buried oxide layer underneath the structures which were supposed to stay anchored to the substrate. As a result of this delamination the moving and stationary electrodes of the comb structure did not stay in the same plane. This reduced the capacitance between the electrodes to impractically small values.

5.2 MUMPs process

Devices were also fabricated in MUMPs technology available from MEMSCAP. The MUMPs process is a three-layer polysilicon surface micromachining process derived from the work performed at the University of California, Berkeley in the late 1980's and early 1990's [108]. The process is modified to make it more versatile for average MEMS designers [162].

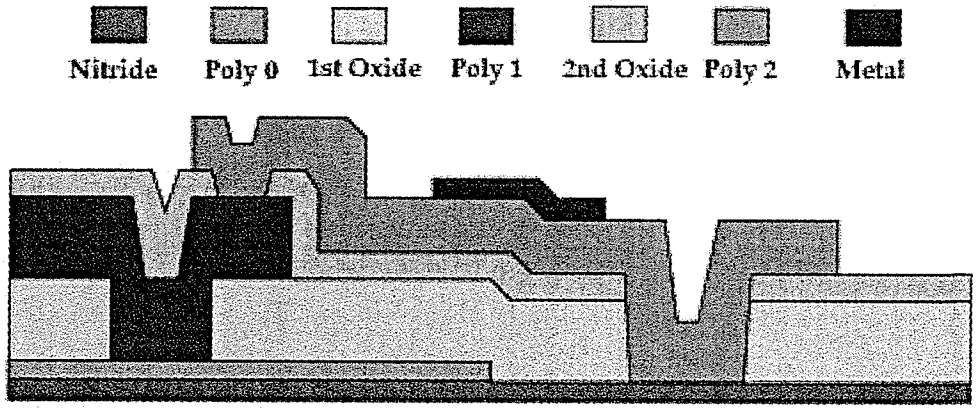

Figure 5.3: *Cross section of layers in MUMPs technology.*

The process starts by depositing an insulating nitride layer (Nitride in Figure 5.3) on heavily doped $100mm$ silicon wafers by LPCVD (low pressure chemical vapor deposition). Then the following layers are deposited and patterned in subsequent steps:

1. A $500nm$ LPCVD polysilicon film (*Poly 0*);
2. A $2\mu m$ LPCVD phosphosilicate glass (PSG) sacrificial layer (*1st Oxide*);
3. A $2\mu m$ LPCVD structural polysilicon film (*Poly 1*);
4. A $750nm$ LPCVD phosphosilicate glass sacrificial layer (*2nd Oxide*);
5. A $1.5\mu m$ LPCVD polysilicon film (*Poly 2*);
6. A $500nm$ metal film (*Metal*).

Sacrificial oxide layers are etched last. A critical-point drying process is used to avoid stiction of the released devices to the substrate.

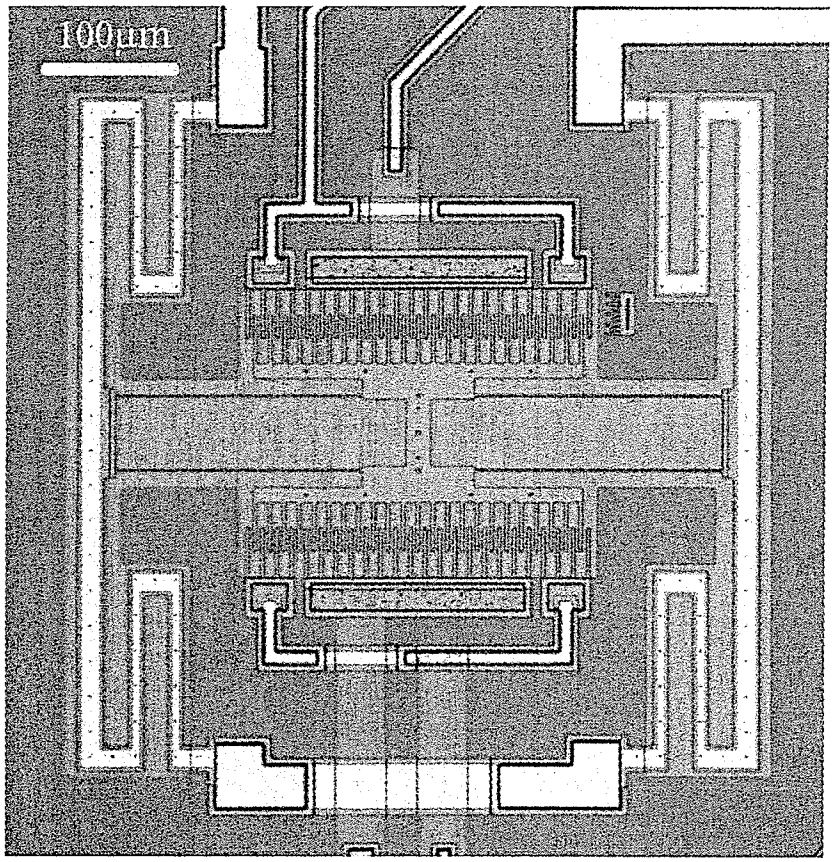

Figure 5.4: *Optical image of a sensor made in MUMPs process.*

A sensor made in the MUMPs process is shown in Figure 5.4. These sensors also failed to operate as expected. After investigating the structure of the sensor, it was observed that the released combs were not in plane with the stationary combs. The cause of this problem was the development of an internal stress in deposited thin films during their fabrication, especially in the metal layer on the crossbars.

5.3 MicraGEM process

The sensors were fabricated in MicraGEM technology available from Micralyne [159]. The process steps for fabrication of devices in MicraGEM technology are illustrated in Figure 5.5 and are:

1. A Pyrex substrate with a thickness of $525\mu m$ is isotropically etched in two subsequent steps to depths of $2\mu m$ and $10\mu m$, respectively;
2. Bottom metal electrodes are patterned inside the etched cavities;
3. An SOI wafer is anodically bonded to the Pyrex substrate;
4. Handle wafer and buried oxide layers are etched away in a wet process;
5. Top metal layer is deposited (750Å of gold on top of 100Å of chrome) and patterned;
6. The silicon layer (device layer of the original SOI wafer) is patterned and etched in a DRIE system.

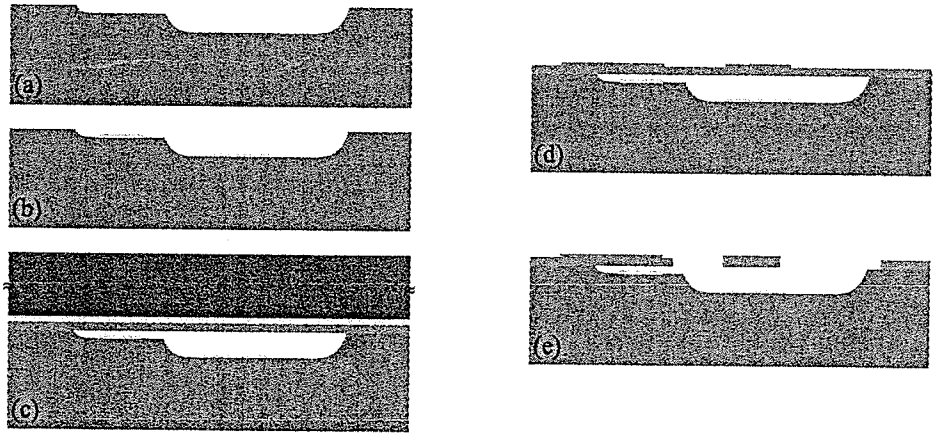

Figure 5.5: *MicraGEM process flow.*

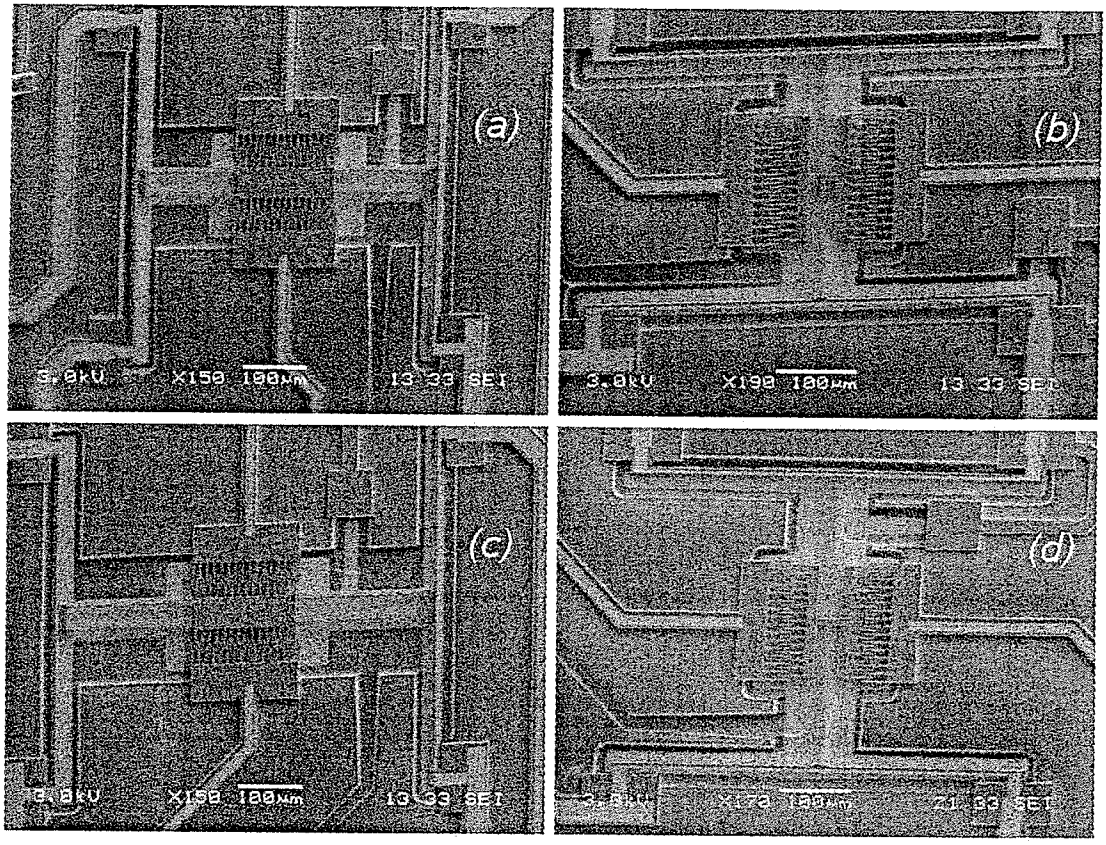

Figure 5.6: *SEM images of the sensors fabricated in MicraGEM process.*

MicraGEM is a bulk micromachining process and the structures made in this process do not suffer from preexisting stresses. The device layer of the SOI wafers used in this technology is $10\mu m$ thick, which translates into $10\mu m$ tall devices. Deposited thin films, on the other hand, have thicknesses on the order of a few micrometers. The thicker structural films result in higher capacitance values between neighbor structures, which is often a favorable design parameter for electrostatic device applications. The lithographic resolution of MicraGEM process is $2\mu m$.

The sensors fabricated in MicraGEM process are shown in Figure 5.6. These images were taken with a Jeol 5900LV scanning electron microscope (SEM). To reduce

Table 5.1: *Physical dimensions of the micromachined structure.*

Device	***a***	***b***	***c***	***d***
Number of beam springs	4	2	4	2
Length of beam springs (μm)	150	150	200	200
Mass of shuttle (ng)	256.3	190.8	256.3	190.8
Width of beam springs (μm)	3			
Number of fingers	15			
Finger $L \times W(\mu m^2)$	35×3			
Finger gap (μm)	2.5			
Crossbar $L \times W(\mu m^2)$	520×9			

the charge build up on the surface of the glass substrate, the microscope was used in *low vacuum* mode with a probe current of $\sim 10pA$. The differences between these devices are in the number of beam springs that attach the shuttle to the crossbars (2 or 4) and the length of these beam springs ($150\mu m$ or $200\mu m$). Dimensions of the devices are summarized in Table 5.1.

Due to the undercut during the DRIE etch step, the lateral dimensions of the silicon structures was reduced by $0.25\mu m$ at the surface on each side of any of the structures. Consequently, the cross section of a beam, which was designed to be rectangular, is trapezoidal (see Figure 5.7). The change in the geometry of a structure

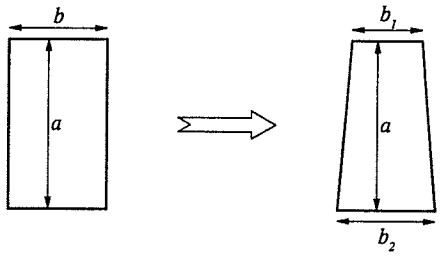

Figure 5.7: *Effect of undercut on beam geometry.*

affects its mechanical behavior. The most important of these structures are the beam springs that connect the shuttle to the crossbars since their spring constant is proportional to the third power of the width of the beams. This can be taken into account by modifying the value of the moment of inertia for the beams. For a beam with a trapezoidal cross section, as the one shown in Figure 5.7, the moment of inertia can be found from equation 3.14 and is given by:

$$\mathcal{I} = \frac{a}{48}(b_1 + b_2)(b_1^2 + b_2^2) \tag{5.1}$$

which reduces to $\mathcal{I} = \frac{1}{12}ab^3$ for $b_1 = b_2 = b$; i.e., for a rectangular cross section. The reduction of the value of $\mathcal{I}$ due to the undercut causes the spring constant of the beam springs to be less than the designed value (see equations 3.21 and 3.28). Consequently, the resonant frequencies of the fabricated devices are lower than the expected values unless the change in geometry is taken into account at the design stage.

Chapter 6

Experiments

Experience teaches slowly and at the cost of mistakes.

James A. Froude (1818 - 1894)

This chapter describes the methods used to test the fabricated devices. The devices were initially tested in air and their resonant frequencies were optically measured. The use of standard laboratory equipment, such as a spectrum analyzer or a lock-in amplifier, for testing of the devices is discussed. Air damping causes the quality factor of the micromachined resonators to be low when operated in air. The low quality factor deteriorates the accuracy of frequency measurements. To increase the quality factor of the resonators, a custom vacuum chamber with electrical feedthroughs was made to allow testing of the devices under vacuum. For practical applications of the sensor, it may be packaged under vacuum at the end of the fabrication process. Details of the electronic circuits used to process the sensor signal are explained in the next chapter.

6.1 Sensing techniques

Using equation 3.11, the amplitude of shuttle displacements at resonance (i.e., $\omega_a = \frac{1}{2}\omega_0$) for $V_G = v_g = 0$ for a setup similar to Figure 7.1 is given by:

$$y = \left(\frac{\partial C}{\partial y}\right) \frac{v_a^2 Q}{4K} \tag{6.1}$$

This equation can be used to analyze the data from optical detection of shuttle displacements or to estimate the maximum shuttle displacement for a given signal amplitude.

For electrical testing, the input or output currents of the device have to be processed. However, the input port of electrostatic transducers is a high-impedance node, and therefore, measuring the input current may cause interference with device operation. Consequently, it is the output current of the resonator that is usually processed.

Using equation 3.12, the magnitude of the resonance current (i.e., $\omega_a = \frac{1}{2}\omega_0$) for $V_G = v_g = 0$ is:

$$i_{out} = \left(\frac{\partial C}{\partial y}\right)^2 \frac{v_a^2 V_B \omega_0 Q}{4K} \tag{6.2}$$

This equation provides the necessary information to analyze the data from electrical testing of a resonator at resonance.

6.1.1 Optical measurement

Movements of the shuttle of an electrostatic device can be observed optically. Techniques that have been employed to optically detect the movements of the shuttle employ a strobe light, a laser beam-bounce setup, or an optical interferometer

[108, 150, 163]. Although these techniques are easy to use and can provide accurate measurements, integration of the optical apparatus with the device is difficult and these techniques are not discussed further.

6.1.2 Baseband sensing

Baseband sensing is the term used to refer to the case when the signal processing is performed at the same frequency as the drive signal. If v_g is set to $0V$ for the system shown in Figure 7.1, the output current will have frequency components at the first two harmonics of the drive signal (see Figure 6.1). In practice, there is also a large feedthrough/interference signal at the actuation signal frequency which makes precise electrical measurements (amplitude or phase) of the actual signal very difficult. Consequently, this method is not used unless the level of the feedthrough signal has been reduced through operation in vacuum and use of integrated electronics [103].

6.1.3 Frequency doubling

The output signal will be a single frequency signal at $2\omega_a$ if V_G and v_g are both set to $0V$. Interference and feedthrough signals still pose problems in taking accurate

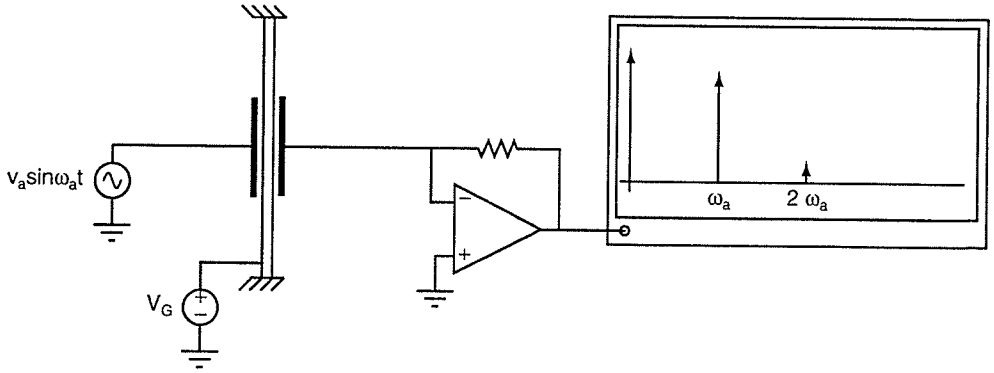

Figure 6.1: *Baseband electrostatic sensing.*

measurements. However, since the output signal of the device is at twice the frequency of the interfering signals, it is possible to recover the sense signal with proper filtering of the output signal. This generally means employing high-order highpass filters. A technique to reduce the order of the required filters in discussed in section 7.2.1.

6.1.4 Electrostatic modulation

As mentioned in section 6.1.2, existence of large interfering signals makes precise baseband signal detection very difficult. The quadratic relationship between the electrostatic force and the voltage difference between the electrodes can be employed to modulate two signals at different frequencies and then investigate the signals at $\omega_a \pm \omega_g$ to extract information about the shuttle movements as illustrated in Figure 6.2. The drive and modulation frequencies can be chosen such that the output signal filtering requirements are relaxed [103, 108]. In practice, however, the nonlinearity of the electronic elements used in signal path also causes generation of interfering signals

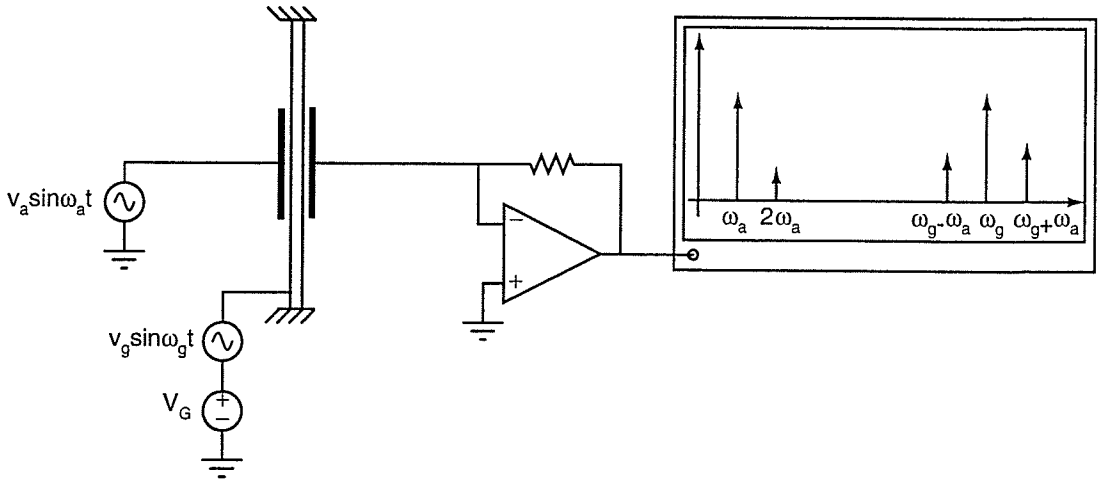

Figure 6.2: *Electrostatic modulation sensing.*

at $\omega_a \pm \omega_g$. Moreover, this technique needs two stable signal sources, adding to the cost and complexity of the overall system.

6.1.5 Gated spectrum analysis

Another method of taking electrostatic measurements while avoiding the interference from the drive signal is to use a square wave for the actuation signal. Micromachined devices have relatively large quality factors (500 – 50000), which causes the shuttle of the sensor to oscillate after applying a step input. If measurements of a spectrum analyzer can be synchronized with the input pulse generator, the output signal can be processed without worrying about interference [103, 108]. The main drawbacks of this method are the need for specific equipment and the difficulty in taking precise amplitude measurements.

6.2 Optical measurements

In order to find out the resonant frequency of the devices, they were initially tested in air and the oscillations were observed with an optical microscope. At resonance, the amplitude of vibrations dramatically increases (by as much as Q times). This

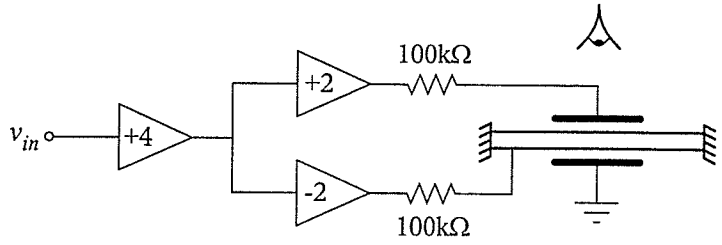

Figure 6.3: *The setup used for optical measurements in air.*

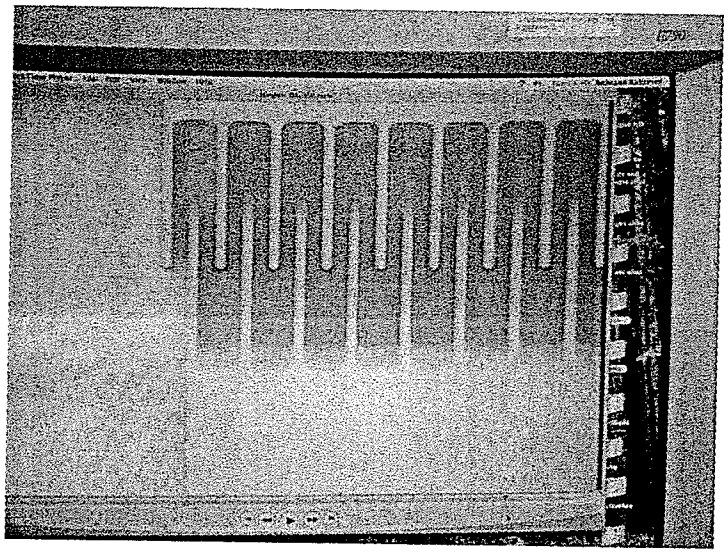

Figure 6.4: *Resonance envelope for a device operating in air.*

increase in amplitude appears as a blurry envelope under the microscope (see Figure 6.4). However, the required voltages for driving the sensor into visible resonance are relatively large (e.g., $80V$). Such large voltages were applied differentially to avoid the use of multiple power supplies as illustrated in Figure 6.3.

6.3 Operation in air

The most straight forward testing method is to use a spectrum analyzer to view the output signal of the sensor and monitor the changes in its frequency. However, the signal may be too small and can be lost in the noise produced by the spectrum analyzer. A low noise amplifier should be added between the output of the device and the input of the spectrum analyzer to improve the signal level. The other problem that arises is the existence of feedthrough signals. These interfering signals, especially the ones through the substrate, can easily be orders of magnitude larger than the desired

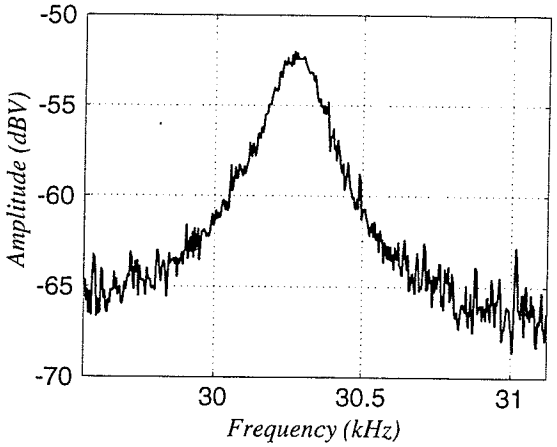

Figure 6.5: *Output spectrum of an electrostatic resonator in air using a preamplifier with a gain of $10^7\Omega$. A $2V$ sine wave was differentially applied between the comb and the shuttle. The sensing comb was biased at $-45V$.*

output signal of the sensor. Signal modulation techniques can be used to isolate the main and feedthrough signals in the frequency domain [108–110]. The other way to reduce the level of feedthrough signals is to lower the applied signal levels, which affects the amount of structure movements and eventually the level of the output

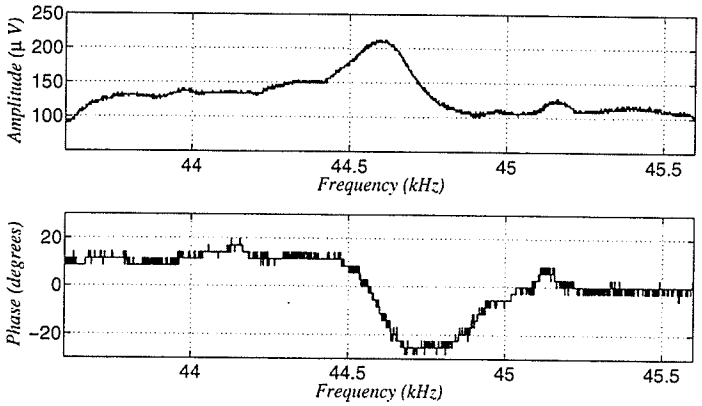

Figure 6.6: *Measured amplitude and phase response of an electrostatic resonator in air using a lock-in amplifier. The input voltage was a $10V$ sine wave applied to the drive comb while the shuttle was biased at $40V$.*

signal. Figure 6.5 illustrates the measured spectrum of the sensor output after a preamplifier with a gain of $10^7\Omega$.

A more sensitive technique to test the devices is to use a lock-in amplifier to monitor the output signal of the sensor (see Figure 6.6). Changes in the resonant frequency of the sensor can be detected by sweeping the frequency of the output of the function generator which is applied to the input comb of the resonator. Using a lock-in-amplifier eliminates the need for the low noise preamplifier. However, feedthrough signals are still a problem, since they are at the same frequency as the output signal and modulation of the signals may be needed.

6.4 Operation under vacuum

The sensor can be operated under vacuum in order to reduce the air damping effects. The increased quality factor makes frequency measurements more precise and, as discussed in the next chapter, improves the signal to noise ratio of the sensor output. Moreover, the larger quality factor results in smaller voltages that are needed for operating the device at resonance. Applying smaller drive voltages reduces the interference at the output and relaxes the requirements on the signal processing electronics.

To test the sensors, the packaged chip is transfered to a vacuum chamber (see Figure 6.7). Using a roughing pump, the pressure inside the chamber during the sensor operation is brought down to $15 - 20mTorr$. Electrical connection with the sensor is maintained through vacuum electrical feedthroughs. The signal from the lock-in amplifier for a sensor operated under vacuum is shown in Figure 6.8. When a

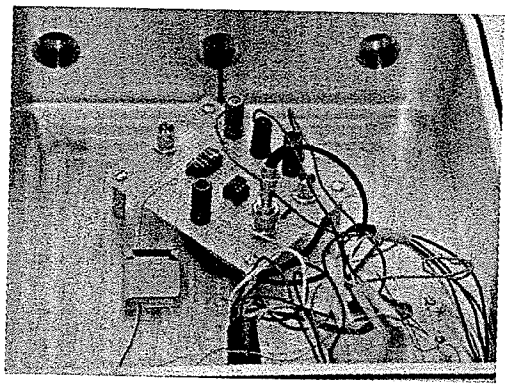

Figure 6.7: *The packaged sensor and the preamplifier inside the vacuum chamber.*

lock-in amplifier is not used, a transresistance preamplifier with a gain of $10^7\Omega$ is also put inside the chamber to amplify the sensor signal before it is buried in the interfering signals during its transmission to the outside of the chamber. The measured output spectrum of device c with a $4V$ drive signal and a $30V$ bias voltage on the output comb

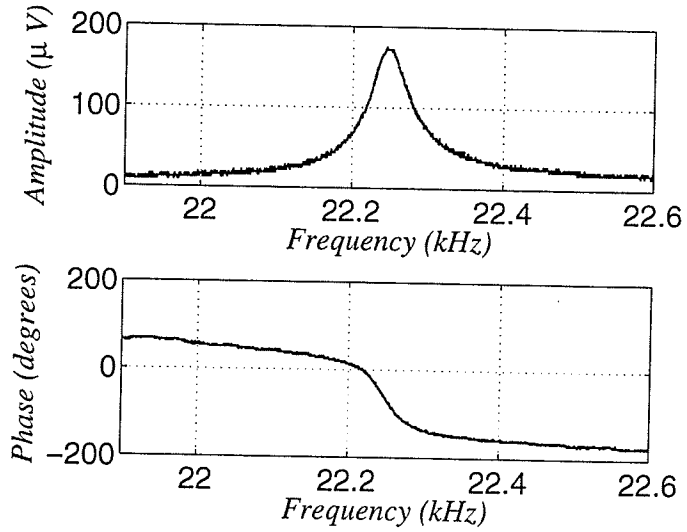

Figure 6.8: *Amplitude and phase of the sensor output when operated under vacuum with an unbiased shuttle. The input voltage was a $3V$ sine wave whose frequency was swept about half the resonant frequency of the device.*

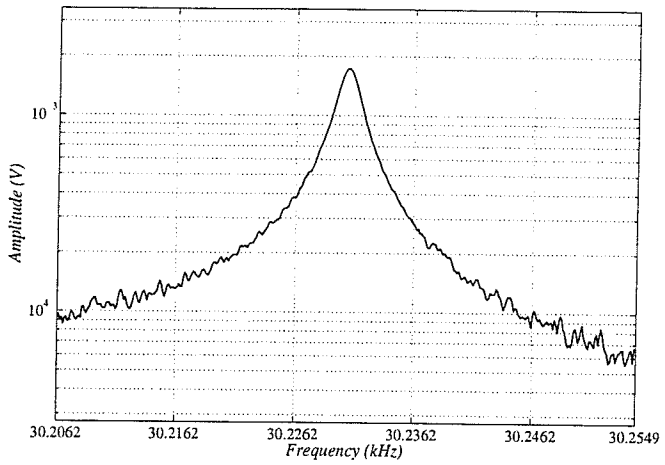

Figure 6.9: *Output spectrum for device c.*

is shown in Figure 6.9. The frequency of the input signal was swept from $15101.5Hz$ to $15128.5Hz$ in $200sec$ and the output of the amplifier was monitored on a spectrum analyzer (Stanford Research model SR760). The quality factor of the resonance for this device was measured to be 15478 at its resonant frequency of $30.2306kHz$ by locating the frequencies where the amplitude of the signal droped by $-3dB$ and using equation 3.10. Knowing the gain of the preamplifier and using equation 6.2, parameter $\partial C/\partial y$ is found to be $0.283fF/\mu m$, which is less than the expected value of $1.1fF/\mu m$. The possible reasons for the existing discrepancy are the differences between the geometry of the fabricated device and the designed structure (e.g., the gap between the fingers), inaccuracy in the provided material properties (e.g., Young's modulus of silicon), and the variation of the actual gain of the preamplifier from its designed value due to the nonidealities of the circuit elements (e.g., finite gain and input capacitance of the OpAmps). Using equation 6.1, the amount of the shuttle displacements at resonance can be calculated and is $1.43\mu m$ for this device. To avoid the nonlinear operation of the sensors at resonance (see Figure 7.11), the amount of

shuttle displacement at resonance was kept in the range of 0.8 to 1.9μm by adjusting the input signal amplitude. The output current of the resonating devices is on the order of 0.8 to 4nA for most cases.

6.5 Thermal effects

The heat produced by passing a current through the crossbars affects the resonant frequency of the structure as discussed in Sections 3.4 and 4.4. Figure 6.10 is the measured output spectrum for device a with crossbar currents of 0 to 6mA. The plot was produced by setting the current in crossbars to a given value and sweeping the frequency of the input signal for the illustrated range. The measurement was then paused, the value of the current was set to a different value, and the frequency of the signal was swept again. The spectrum analyzer was setup such that the signal at a frequency was updated only if the current value of the signal is larger than the previous measurements. As can be seen, the resonant frequency of the device decreases with increasing current. The frequency difference between the resonant peaks is proportional to the square of the current, an indication of the fact the generated heat is responsible for the shift in the frequency. The slight increase in the resonant peak of the device for larger currents can be explained by considering that the Young's modulus of silicon decreases as it is heated up. Consequently, the spring constant of the beams decreases with temperature, and therefore, the amplitude of vibrations for a given drive signal amplitude increases. This in turn causes an increase in the output current of the device.

Figure 6.11 illustrates the changes in the resonant frequencies of all of the devices versus the current in their crossbars.

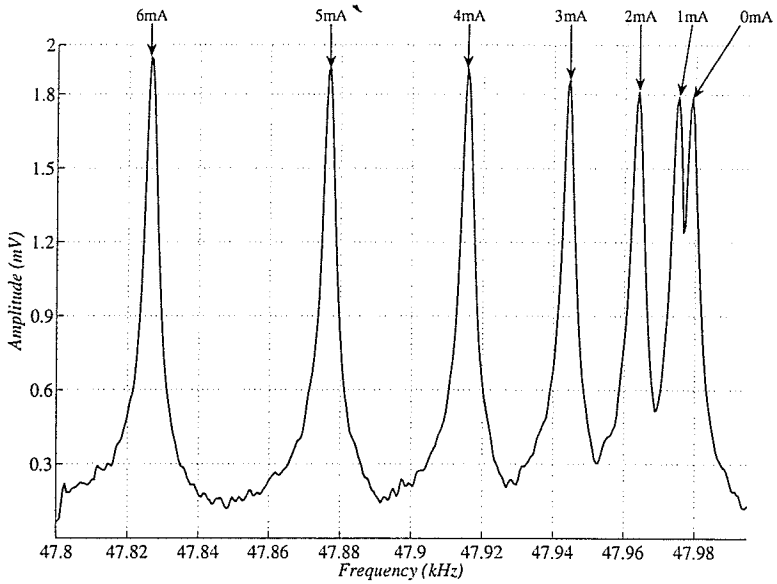

Figure 6.10: *The change in resonant frequency of device a due to the heat generated by the current in crossbars.*

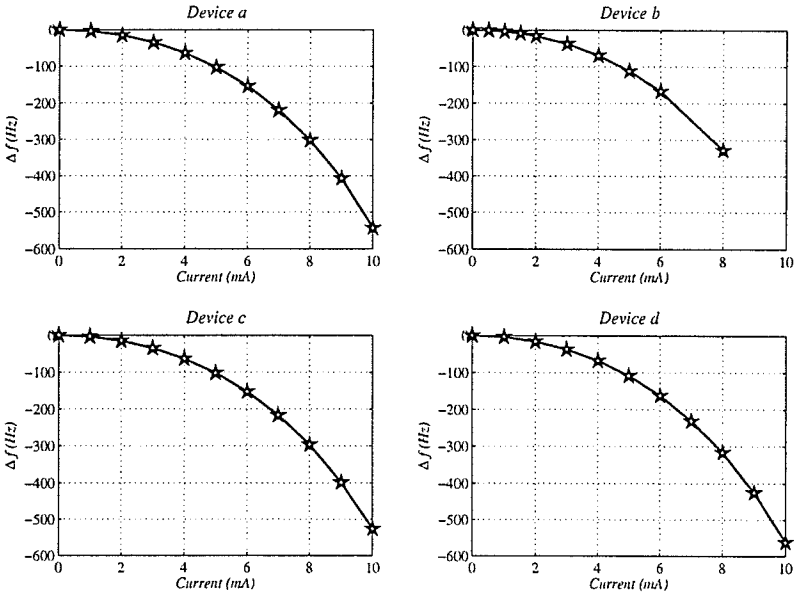

Figure 6.11: *The change in resonant frequency of devices a to d with the current in crossbars.*

6.6 Sensitivity measurements

In order to measure the sensitivity of the sensor to magnetic fields, one should put the sensor inside a variable magnetic field and monitor its output. The standard technique for creating an easily controllable magnetic field is using Helmholtz coils [164–166]. The Helmholtz pair is composed of two parallel similar thin coils separated by a distance equal to their radius. This combination can generate small but uniform magnetic fields along the axis that connects the centers of the two coils in the space between them. However, it proved not to be easy to use the Helmholtz coil to test the fabricated sensors. The sensors operate under vacuum and to use Helmholtz coils, either the chamber has to be made small enough to fit in the space between the coils or the coils have to be built such that they can be put inside the vacuum chamber. Neither of these two solutions are easy to implement, considering the number of vacuum connections and electrical feedthroughs which are needed for proper characterization of the sensor operation.

Remembering that:

$$S_B^{\omega} = \frac{3\, I_{XB}\, L_{XB}\, \omega_0}{5\, N\, L\, k_b} \tag{6.3}$$

and also noting that the sensor has a linear response for feasible values of magnetic fields (i.e., $B \leq 5T$), it can be seen that one could change the current in crossbars in order to measure the sensitivity of the sensor. Therefore, to test the sensors, they were put inside a constant and uniform magnetic field produced by two permanent magnets and the current through the crossbars was varied. The produced field in between the magnets was measured with a Gaussmeter and was found to be $0.4T$. The problem with this method is that the resonant frequency itself is a function of

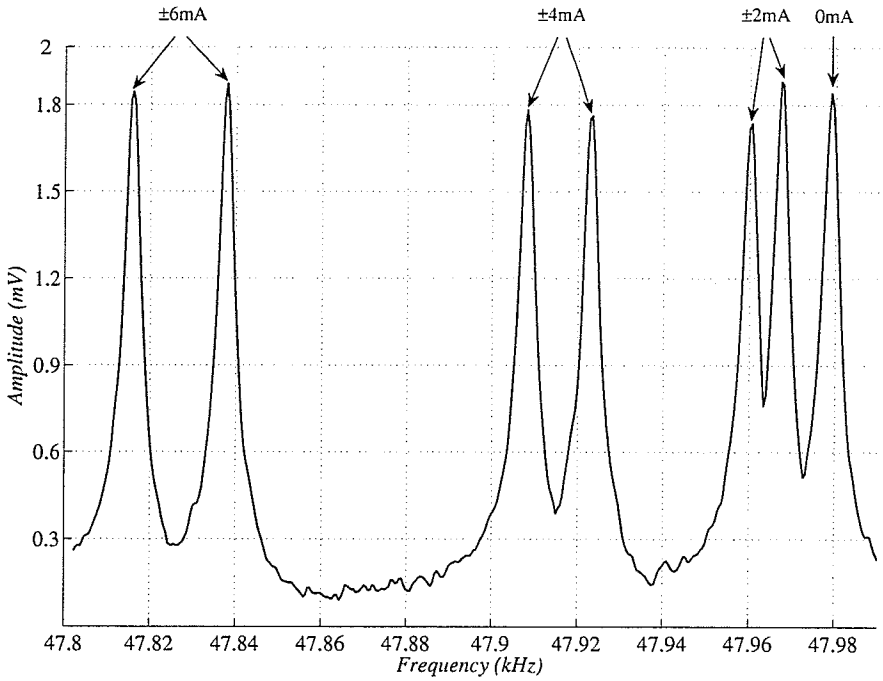

Figure 6.12: *The output spectrum of device a for* 0, $\pm 2mA$, $\pm 4mA$, *and* $\pm 6mA$ *of current in crossbars inside a* $0.4T$ *field.*

the current in the crossbars, and so, as the structure heats up differently for different values of current, the resonant frequency shifts accordingly. However, the frequency shift due to the generated heat does not depend on the direction of the current while the Lorentz force on crossbars switches direction if the direction of the current flow in the beams is reversed. Consequently, it is possible to take a differential measurement by switching the direction of the current in crossbars which alleviates the effect of temperature changes (see Figure 6.12). An added advantage of this technique is that it also removes the offsets that are produced by electronics, variations of the pressure inside the chamber, changes in the absolute value of the current in crossbars, etc. The only remaining factor to consider is the change in the material properties of the heated sensor which causes an increase in the sensitivity of the sensor at larger

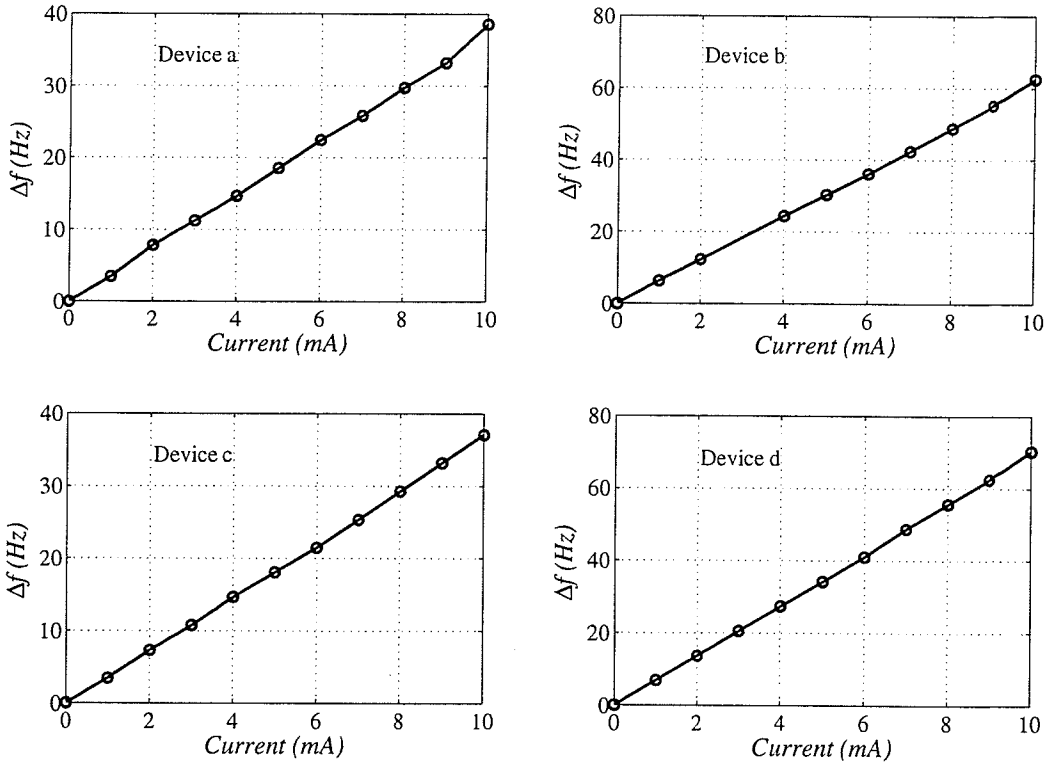

Figure 6.13: *The measured differential change in the resonant frequency of devices a to d for crossbar currents of* 0 *to* $\pm 10mA$ *inside a* $0.4T$ *field.*

currents. This is because the Young's modulus decreases with temperature, which in turn causes a reduction in the spring constant of the beams. As can be seen from equation 6.3, the reduction of the spring constant enhances the sensitivity. However, this effect can be accounted for when processing the output signal of the sensor.

Figure 6.12 illustrates the output spectrum of the device a for different values and directions of the current in crossbars. For differential measurements, the difference in frequencies of the peaks for the two opposite directions of the current should be measured. Figure 6.13 illustrates the differential measurement results for all of the devices. Note that the net change in the resonant frequency of the devices is half

Table 6.1: *Comparison of modeling, simulation, and experimental results.*

Device	*a*	*b*	*c*	*d*
Number of beam springs	4	2	4	2
Length of beam springs (μm)	150	150	200	200
Modeled F_r (Hz)	52462.09	46581.80	32974.20	29880.82
Simulated F_r (Hz)	54838.7	45438.9	35485.1	29611.6
Measured F_r (Hz)	47983.398	41515.625	30230.469	26986.328
Modeled $S_B^{F_r}$ for $\Delta T = 0$ (Hz/T)	31.60	56.12	35.25	63.89
Simulated $S_B^{F_r}$ for $\Delta T = 0$ (Hz/T)	36.5	57.6	41.9	65.8
Modeled $S_B^{F_r}$ for $I_{XB} = 10mA$ (Hz/T)	32.16	57.10	35.87	65.01
Simulated $S_B^{F_r}$ for $I_{XB} = 10mA$ (Hz/T)	36.6	57.6	41.9	66.1
Measured $S_B^{F_r}$ for $I_{XB} = 10mA$ (Hz/T)	48.22	78.13	46.39	87.89

of the plotted value for each value of the current in the crossbars. This figure also illustrates the linear response of the sensor even for large values of crossbar current in a relatively large field (i.e., $0.4T$).

The measurements are compared with simulation and modeling results in Table 6.1. It can be seen that the simulation and modeling results agree with each other since both results were based on similar assumptions for properties of materials and geometry of fabricated devices. Compared to experimental values, both simulation and modeling results overestimate the resonant frequencies but underestimate the sensitivity of the devices. The possible reasons for the existing discrepancies are:

- MicraGEM process that was used to fabricate these devices is a new process and still under development. Consequently, the material properties stated for the device layer in MicraGEM manual might not be accurate;

- One of the simulations and modeling assumptions was that the crossbars are connected to stiff anchors. This is not true since the crossbars are attached to the substrate through pieces of silicon which deform during the sensor operation;

- It was assumed during the thermal analysis of the structures that the temperature at the ends of crossbars is constantly kept at room temperature. However, since the thermal dissipation happens through the structural silicon layer which is on top of a glass substrate (i.e., an insulating material), the temperature at the ends of the crossbars will be higher than room temperature;
- Geometry of the structures and the device layer thickness can be different from expected values due to process variations and fabrication tolerances.

If necessary, the accuracy of the modeling results can be improved by proper addressing of the above points.

Chapter 7

Electronics

If they had really wanted to do that, they probably could have done many of those functions with discrete components.

Jack Kilby

This chapter describes the methods employed for electrostatic actuation and sensing. The drive electronics are discussed first. Different techniques for electrostatic sensing are explained. In its most basic form, the shuttle of the sensor is grounded and the actuation voltage is a combination of DC and AC voltages. In this case, the output signal is composed of a DC term and two AC signals at the first two harmonics of the drive signal. The sensing electronics were designed to work with this configuration as explained below. Details of the developed signal processing electronics are discussed in Appendix C. It must be noted that, if possible, it is generally best to design the signal processing circuitry on the same chip with the micromachined structures in order to minimize the effects of interference noise.

7.1 Drive electronics

Electrostatic actuators can be driven by controlling the charge or the voltage on electrodes. From the practical point of view, it is easier to control a voltage, and consequently, electrostatic transducers are often driven by a voltage source (amplifier). The drive signal is generally a DC voltage (for electrostatic actuation purposes), a sine wave (for electrostatic resonators), or a square wave (for gated-spectrum analysis or for actuation) [103, 108]. A general setup with sources for actuation, biasing, and sensing for electrostatic transducers is illustrated in Figure 7.1. Relatively large voltages are required if the resonator is operated in air (e.g., $25 - 100V$). This is a consequence of small $\partial C/\partial y$ values for micromachined devices and the air damping effects. However, if these devices are driven to resonate under vacuum, thanks to the increased large quality factors, the required actuation voltages become much smaller

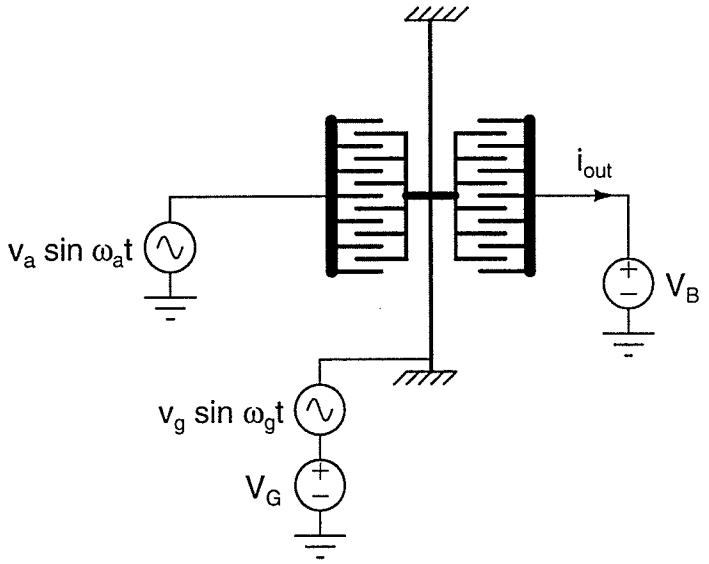

Figure 7.1: *Electrostatic sense and drive circuit illustrating the actuation (i.e., $v_a sin\omega_a t$), modulation (i.e., $v_g sin\omega_g t$), and biasing (i.e., V_B and V_G) sources.*

$(50 - 100mV)$. If packaged under vacuum, the electrostatic transducers can even be integrated with active electronics [103, 105].

7.2 Electronic system design

This section describes the steps taken to extract and process the signal from the sensor. The shuttle of the designed sensor is at ground potential during sensor operation. To take advantage of isolation of input and output signals in frequency domain, the actuation voltage is chosen to be purely AC. A transresistance preamplifier with a gain of 10^7 is put inside the chamber to avoid signal loss during its transmission to the rest of signal processing circuitry. However, the feedthrough signal at the drive frequency can be as much as three orders of magnitude larger than the desired signal at twice the frequency of the actuation voltage. This difference in amplitude does not pose a problem if a spectrum analyzer or a lock-in amplifier is used for signal detection. However, if integration of the sensor with electronics is intended, the interfering signal must be removed, because the large unwanted signal causes nonlinear behavior of the electronic devices (e.g., saturation of the amplifiers).

Filtering of the signal will be the first processing step. The filter design theory is a very mature field and is not discussed here [167–170]. Techniques to overcome beating between interfering signals are then discussed. Design of the circuitry required to use the sensor as a magnetic-field controlled oscillator is explained next. The final step after extracting the desired signal will be to measure the small frequency shifts in the resonant frequency.

7.2.1 Filter design

The small separation of the two signals in the frequency domain and the needed amount of attenuation requires high order highpass filters to extract the sensing signal. For example, if it is intended to attenuate the interference signal by a factor of about 5×10^3 or $74dB$, a highpass filter with a minimum of 12 poles is needed [171]. Designing such a filter is not a straightforward process, nor is its implementation which requires careful attention to the practical limits of the devices, their tolerances, and matching of components between the cascaded stages.

An alternative to relying on achievable attenuation from poles, it is possible to remove the interference signal by placing the zeros of the transfer function of a filter at the frequency of the interference. Such a filter is often referred to as a notch filter. The transfer function of a second order notch filter is given by:

$$T_n(s) = \frac{s^2 + \omega_z^2}{s^2 + \frac{\omega_p}{Q}s + \omega_p^2} \tag{7.1}$$

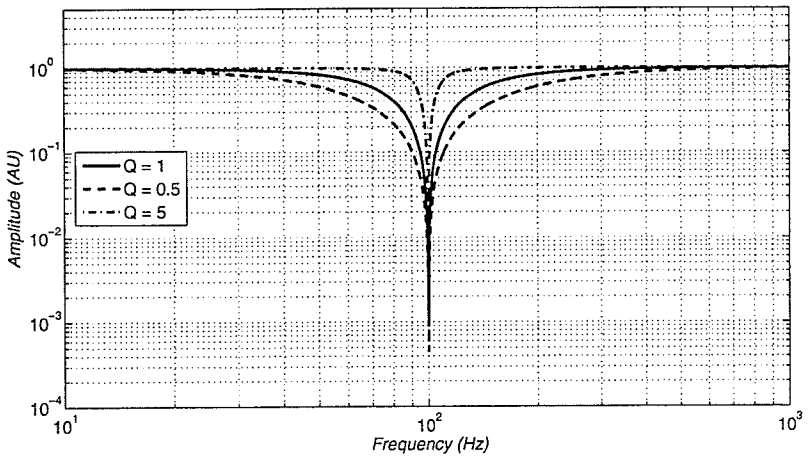

Figure 7.2: *Frequency response of a notch filter.*

where ω_z and ω_p are the frequencies of the zeros and poles of the filter, respectively.

Although the theoretical signal amplitude at the output of the filter is zero, mismatches between component values and their tolerances cause a finite amount of attenuation. Consequently, there is a trade off between the rejection bandwidth of the filter (i.e., Q) and the possible attenuation (see Figure 7.2).

After the notch filter, a high-Q bandpass filter at twice the frequency of the drive signal was used to simultaneously amplify the signal and reduce the noise. Figure 7.3 illustrates the measured frequency response of the filters used for processing the signal from a sensor with a resonant frequency of $38kHz$. As can be seen the frequencies around the interference signal are attenuated by as much as $70dB$ compared to the frequencies about the desired signal.

Noting that the resonant frequencies of the designed devices are different from each other, testing each of them would require designing of a dedicated filter block (notch + bandpass). Using switched-capacitor filters allows the user to tune the frequency response by simply adjusting the clock frequency of the filter. Therefore, both notch and bandpass filters were realized using switched-capacitor filters. The clock frequency used for the bandpass filter was divided by two and used for the notch filter. The frequency response of the filter is therefore adjusted by choosing the proper clock frequency for the notch filter. The output of switched-capacitor filters is a sampled waveform and further lowpass filtering is required to remove the spikes from digital switching (see Figure 7.4).

7.2.2 Beating

Although the desired sensor signal can be recovered with the filter block described in Section 7.2.1, beating between the output signal from the sensor and interfer-

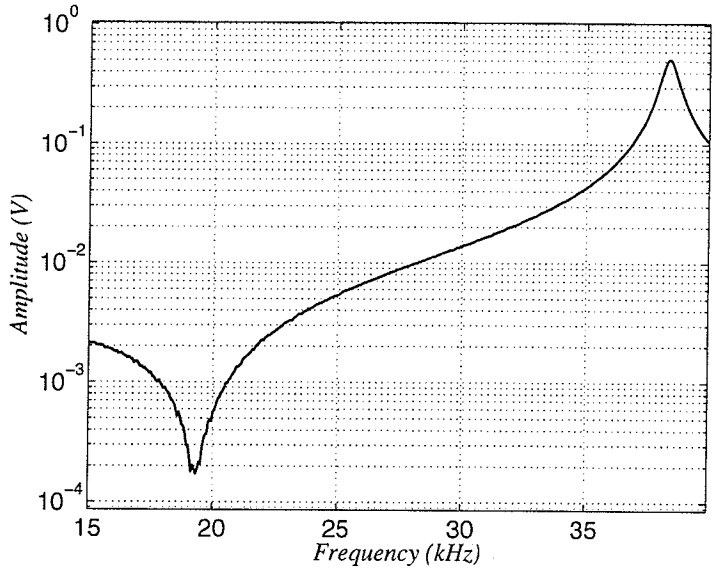

Figure 7.3: *Measured response of the filters (notch + bandpass) used for signal processing for a* $100mV$ *sinusoidal input signal whose frequency was swept from* 15 *to* $40kHz$.

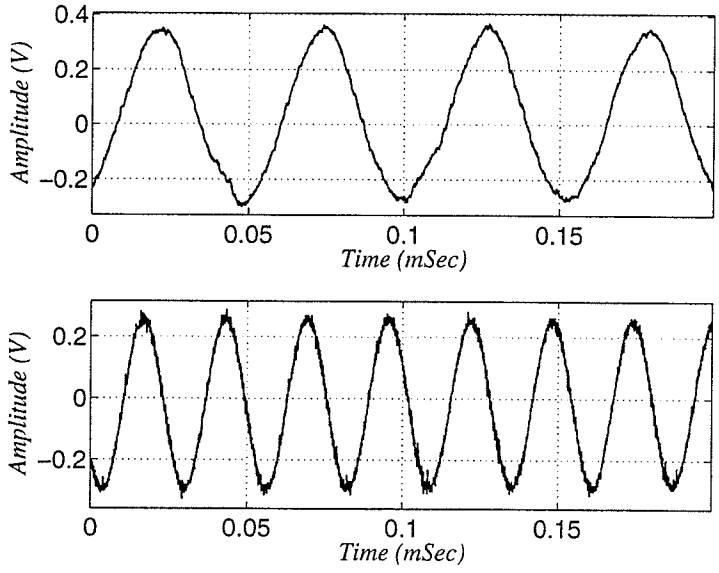

Figure 7.4: *The input signal from the sensor (top) and the output signal (bottom) of the active filter block (notch + bandpass).*

ing signals from various sources (e.g., computer monitors and digital measurement equipment) causes considerable variation in the amplitude of the filter block output. Beating occurs when adding two sinusoidal signals whose frequencies are close to each other. In practice, neither the amplitude nor the frequency of the interfering signals is stable, which makes accurate measurements on the desired signal more difficult. Figure 7.5 illustrates an example of how beating affects the signal properties in time domain where the main signal is $1\ \sin(\omega t)$ and the interfering signal is $[1 \pm rand(0.5)]\ \sin[(\omega + 900 \pm rand(100))t]$, where $\omega = 2\pi \times 4000$. As can be seen, measurements of the signal properties can be quite difficult, especially when the signals interfere destructively. This graph also illustrates the possibility that the comparator may miss pulses for small input signal amplitudes.

Two different techniques were developed to overcome the beating problem and are explained below.

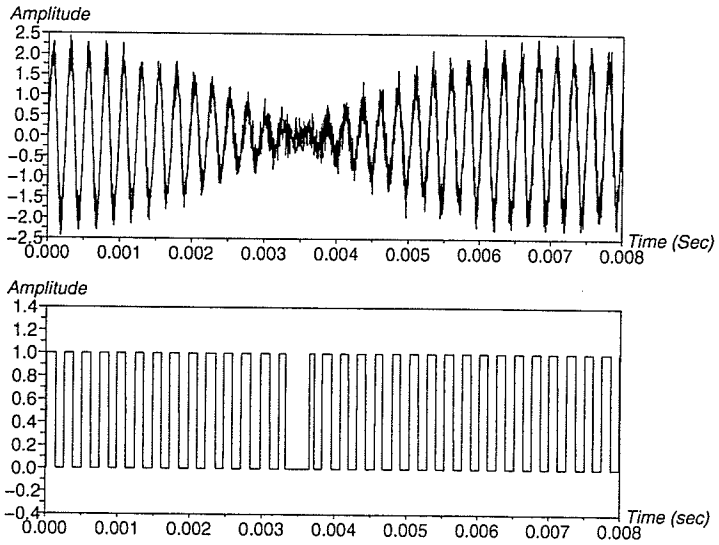

Figure 7.5: *Illustration of the effect of beating on signal properties. The bottom figure shows the output of an ideal comparator with a $0.5V$ hysteresis level when the signal on top is applied to its input.*

Design with a PLL

A phase-locked loop (PLL) can be used to reduce the beating effects on the signal. The PLL can produce pulses to replace the ones that the comparator could not produce because of the small amplitude of the input signal. Consequently, the frequency of the signal from the PLL is more stable and measurements on the PLL signal are more precise than measurements on the resonator signal. On the other hand, PLL cannot track the frequency changes of the input if they are out of its dynamic range. As a result, the output frequency of the PLL does not change significantly if too many pulses are produced by the superimposed noise at the input. The schematic of the implemented design based on a PLL is shown in Figure 7.6. After converting the input signal to a train of pulses, a monostable circuit is used to produce a well-defined pulse width. The output of the monostable circuit is then fed to the PLL input. The dynamic range and tracking speed of the PLL are determined by the gain of the voltage controlled oscillator (VCO) inside the loop and the frequency response of the loop filter. Measured response of the system is illustrated in Figure 7.7. As expected, the pulse width of the PLL output is well defined. This figure also illustrates how the missing pulses were replaced by the PLL.

The use of a PLL, however, adds to the complexity of the system and can adversely affect its performance. For example, the quality of the output signal depends on the

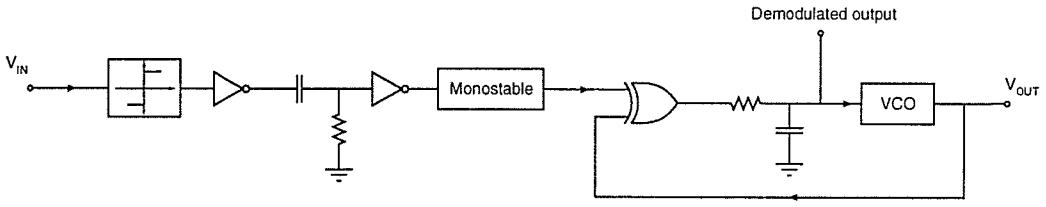

Figure 7.6: *The design based on using a PLL to reduce the beating effects.*

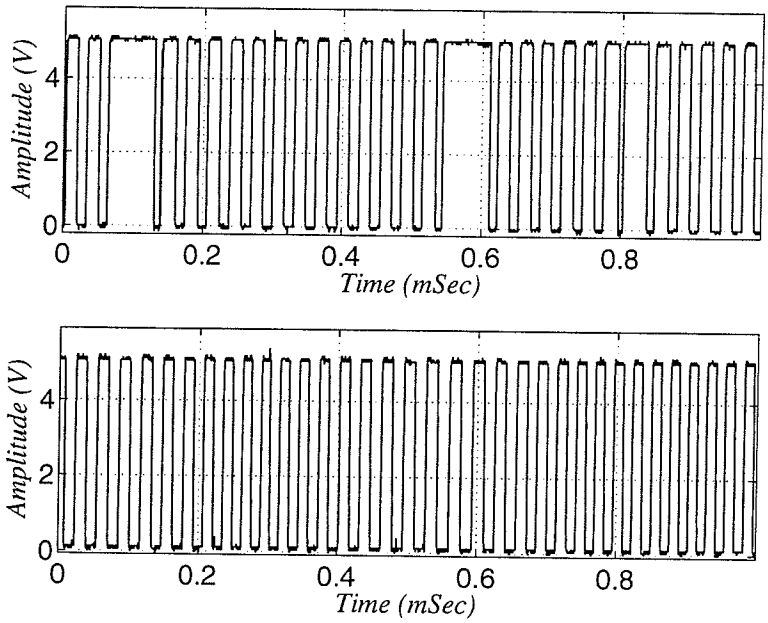

Figure 7.7: *Measured response of the PLL based design to reduce the beating effects. The top figure is the voltage at the output of the comparator while the bottom figure shows the output voltage of the PLL.*

stability of the VCO of the PLL as well as the performance of the employed phase detector. Furthermore, the loop filter of the PLL limits the bandwidth, and hence, the dynamic range of the measurements. Finally, the input signal of the system has to be constantly monitored to make sure that the output signal is actually from the sensor and not from the free-running frequency of the VCO.

Design with high-Q bandpass filters

High-Q bandpass filters may be employed to shrink the bandwidth around the desired signal frequency and reject the signals outside of this band. However, tuning of these filters can be troublesome due to their narrow frequency response. Once more using switched capacitor filters greatly simplifies the design flow, especially since the

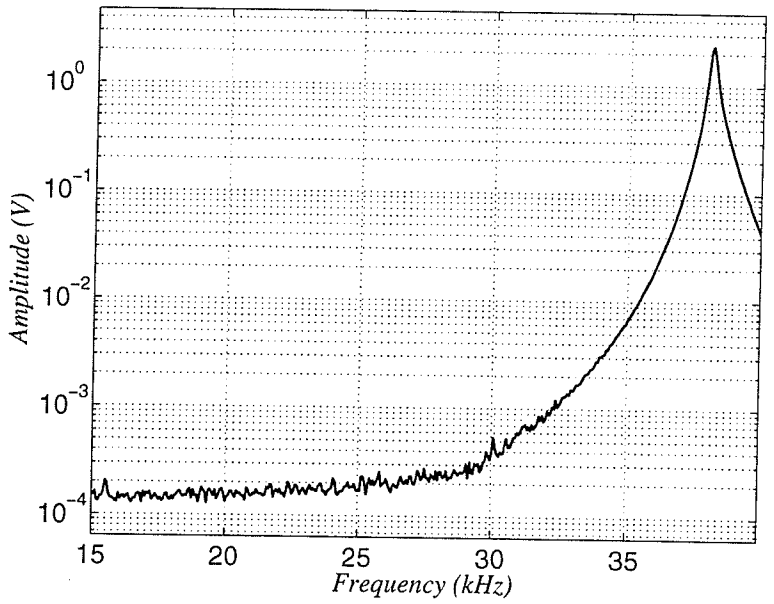

Figure 7.8: *Frequency response of the cascaded filters for a 50mV input signal.*

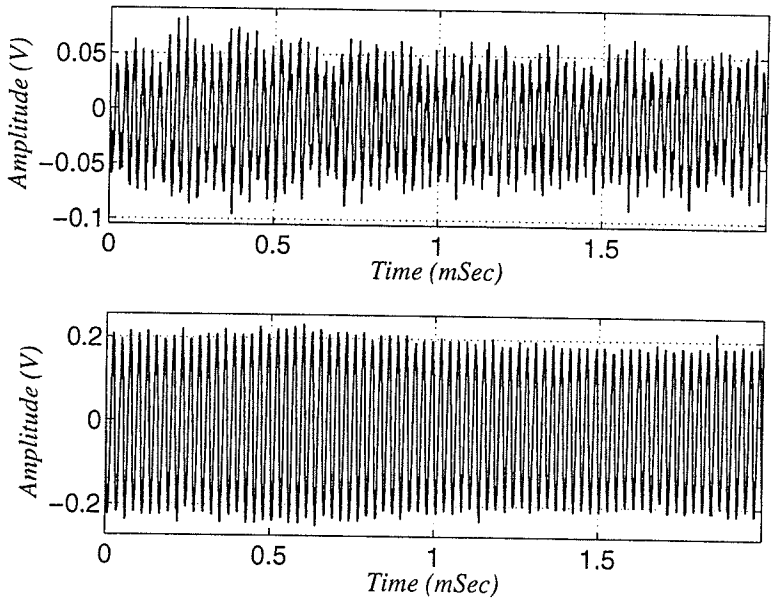

Figure 7.9: *Outputs of the first filter block (top) and the high-Q bandpass filters (bottom).*

clock signal of the filter block in section 7.2.1 can be used for these high-Q filters. Two second-order high-Q filters were cascaded to obtain the desired performance. Therefore, tuning of the electronics for each of the sensors is simply performed by adjusting just one signal; i.e., the clock signal of the notch filter. The measured output spectrum of the combination of the first filter block (notch + bandpass) and the two high-Q bandpass filters is shown in Figure 7.8.

Input and output signals to the filter block in time domain are shown in Figure 7.9. It can be seen that the variation in the amplitude of the sensor signal is reduced from about 40% to around 8%. It should be noted that most of the noise in the output signal is from the switchings inside the filters. This noise can be reduced with a properly designed lowpass filter.

7.3 Measurement setup for driven sensor

Using the circuits discussed so far, the final measurement setup is shown in Figure 7.10. This setup functions as expected and the output signal, V_{out}, may be used to extract various information about the sensor behavior, including data about the strength of the magnetic field.

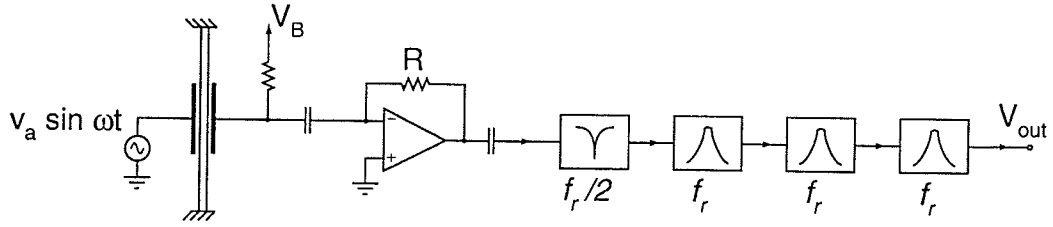

Figure 7.10: Driven sensor and the signal processing electronics.

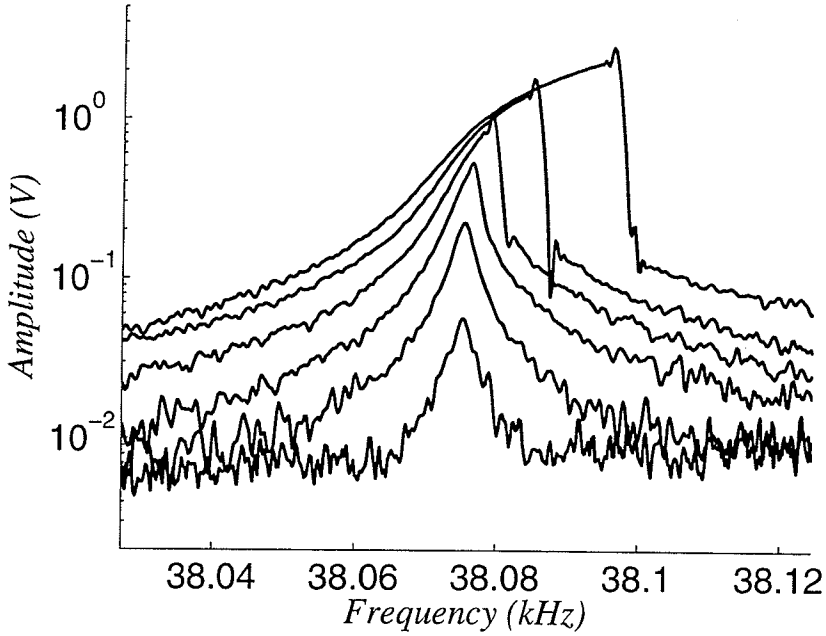

Figure 7.11: *Output spectrum of the sensor response for input signal amplitudes from* $0.5V$ *to* $3V$ *in* $0.5V$ *steps with the frequency swept from low to high in* $100sec$.

As an example, the setup in Figure 7.10 was used to observe the nonlinear behavior of the resonator (see Figure 7.11). A common feature of mechanical resonators with nonlinear springs is the dependence of the resonant frequency of the structure on the signal amplitude [115, 134, 163, 172–174]. The output spectrum of the system was recorded when the input signal was slowly swept around half the resonant frequency of the structure for different input signal amplitudes. The reason for the positive shift in the resonant frequency of the device is the nonlinear behavior of the beam springs. When the signal frequency approaches the resonant frequency of the structure, the amplitude of vibrations increases dramatically due to the high Q of the micromachined device. As the signal amplitude increases, the beam springs become stiffer (i.e., their spring constants increase). This results in an increase in the resonant frequency of

the structure which is roughly proportional to the square root of the spring constant of the beam springs. This nonlinear behavior of the beam springs can be modeled by adding a cubic term to their spring constants [120, 163].

7.4 Oscillator design

The setup discussed in section 7.3 needs a stable signal source with frequency sweeping capability to drive the sensor. Furthermore, the output signal of the sensor was monitored on a spectrum analyzer. For general purpose applications of integrated sensory systems, it is often necessary to be able to read and use the sensor signal with minimal requirements on equipment.

The need for a signal source can be lifted if the sensor is used as part of a self-oscillating network. A linear oscillator (as opposed to relaxing oscillators and such) may functionally be similar to what is shown in Figure 7.12. The oscillations occur at the frequency set by the high-Q block which can be an LC network, a quartz crystal, or a micromachined resonator. If the phase of the input signal to the high-Q network is set properly, a signal with proper frequency is amplified inside the loop. The loop gain in the ideal case has to be unity at desired output frequency. However, in practice the loop gain is designed to be slightly larger than one to assure that the poles of the system are initially in the right half plane. The amplitude of the oscillations is limited by some nonlinear effect in the signal path (e.g., the saturation of the amplifier).

The setup shown in Figure 7.12 is often used for harmonic oscillators in electronic systems. A similar setup can be used with a micromachined resonator incorporated

as the high-Q element. However, employing an electrostatic resonator in this simple configuration yielded poor results in terms of the frequency stability of the oscillator. The main reason for the low quality of the oscillator is the large feedthrough signal at the drive signal frequency which effectively masks the high quality factor of the resonator. Therefore, using this simple configuration is best feasible when the micromachined resonator can be integrated with signal processing electronics, since in such cases the interference signals are greatly reduced for the reasons discussed earlier [104, 175].

The problem of the feedthrough signal in the oscillator design case can be circumvented with the same circuitry described in section 7.3. However, the sensor has to be driven at half the resonant frequency of the device in this setup. Therefore, the frequency of the processed signal has to be divided by two. Also, it should be remembered that beating caused variations in the amplitude of the output signal. Since the magnetic field data is extracted from the frequency shifts of the signal from the sensor, the amplitude information can be discarded. This is done by converting the sinusoidal signal to a square wave with a comparator. Dividing the signal frequency

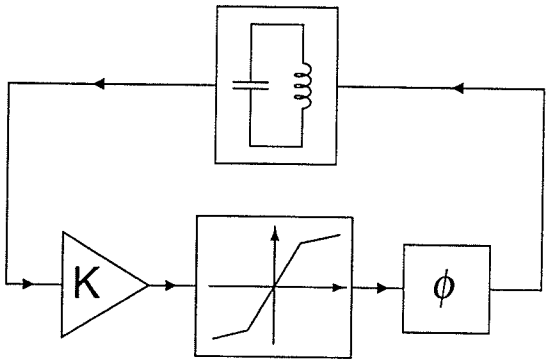

Figure 7.12: *Simplified diagram of a linear oscillator.*

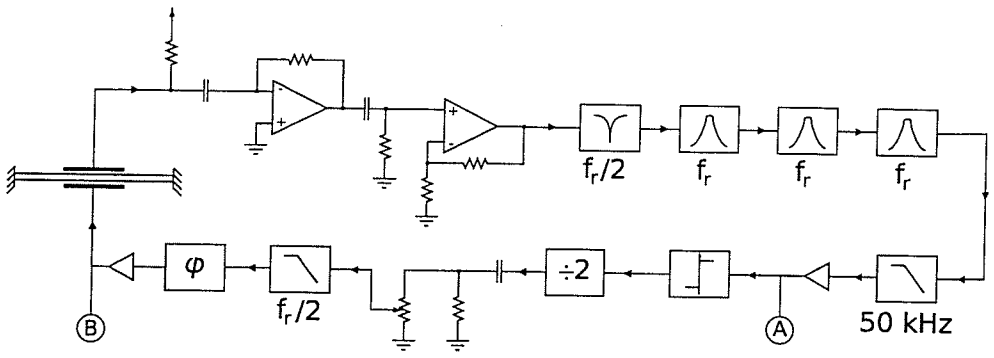

Figure 7.13: *Resonator used in a self-oscillating configuration.*

by two can then be simply done with a T-flipflop. To minimize the spurious signals at the output of the oscillator, the output of the frequency divider is converted back to sinusoidal with a 4^{th} order lowpass filter which attenuates the 3^{rd} harmonic of the output of the frequency divider by about $40dB$. The amplitude of the excitation signal is controlled by changing the gain of an amplifier. The final piece needed to make an oscillator is a phase adjustment circuit to assure excitation of the resonator at the correct frequency and phase. Figure 7.13 illustrates the diagram of the oscillator network.

Using the above configuration, the amplitude of the excitation signal is completely defined and set by the user and does not rely on the properties of the linear and nonlinear elements in the loop. Figure 7.14 shows the input signal to the comparator and the output signal which was applied to the resonator (nodes A and B in Figure 7.13). This configuration improves the quality of the oscillator as a whole and greatly reduces phase-noise and jitter. The measured signal amplitude at a $0.122Hz$ offset from the oscillation frequency of the system (i.e., $38074Hz$) is $50.8dB$ less than the signal level. Figure 7.15 illustrates the measured spectrum of the oscillator output.

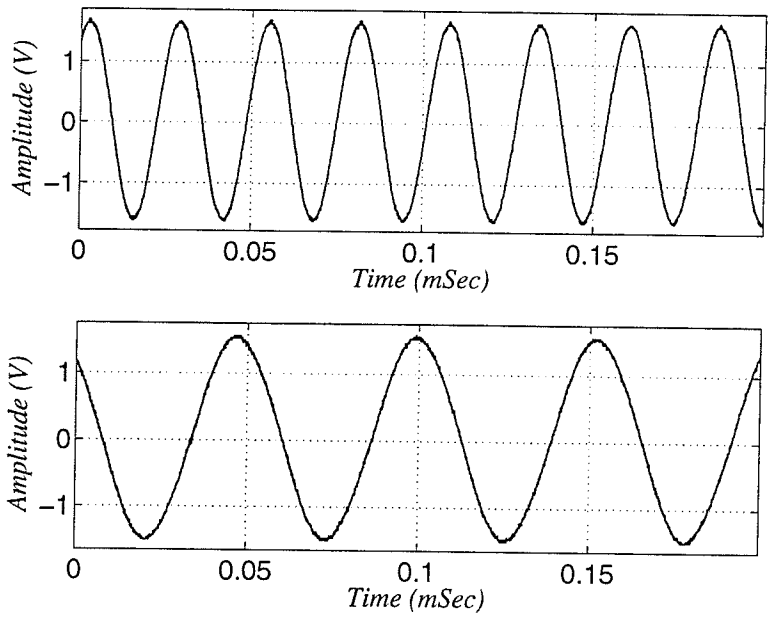

Figure 7.14: *Comparator input from the filtering circuit (top) and excitation signal sent to the resonator (bottom).*

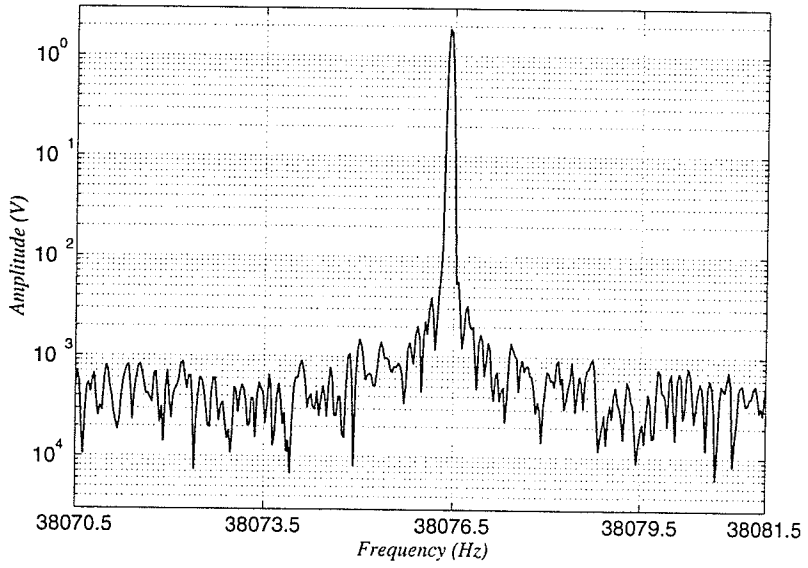

Figure 7.15: *Resonator signal spectrum when operated in self-oscillating configuration.*

7.5 Frequency shift measurement

The output of the sensor is a shift in its resonant frequency. However, the frequency shift is small relative to the signal frequency (e.g., less than $1Hz$ of shift in the frequency of a $40kHz$ signal) and precise measurements are required in order to measure small magnetic fields. In a laboratory environment, it is possible to use a spectrum analyzer or an precise frequency meter to monitor the frequency shifts. Moreover, measurement time can be prohibitively long if standard equipment is used. As an example, it takes $32sec$ to measure a $30mHz$ shift in the frequency of a signal using a Stanford Research model SR760 spectrum analyzer or $1.3sec$ using an Agilent 34401A precision multimeter. Therefore, precise frequency measurement circuitry with enough bandwidth has to be designed if integration of the sensor and electronics is intended.

The simplest method of measuring the period or frequency of a signal is to use an external clock. To measure the frequency of the signal, the number of signal pulses are counted in a time window defined by the clock signal. Measurement of the signal period can be done similarly by counting the number of clock signal pulses inside a time window set by the signal. These techniques are illustrated in Figure

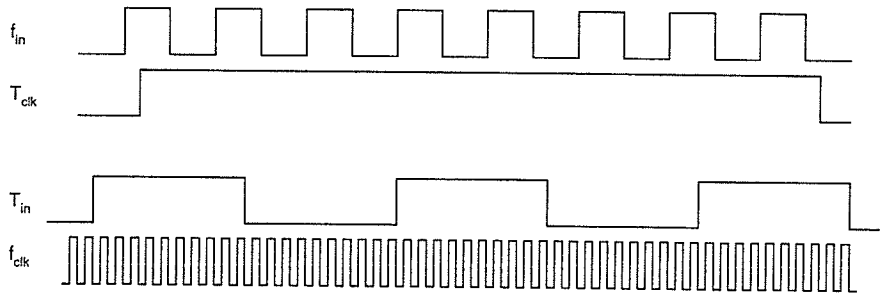

Figure 7.16: *Measuring the frequency (top) and the period (bottom) of a waveform.*

7.16. Both of these techniques, however, are slow. For example, it takes $10sec$ to measure a $0.1Hz$ shift in frequency of the signal. Vernier measurement techniques can be employed to enhance the precision and the bandwidth of these techniques at the expense of system complexity [176, 177].

7.5.1 FM to AM conversion

The setup in Figure 7.10 can be used to convert the variations in the frequency of the signal to changes in its amplitude. This technique takes advantage of the high Q of the oscillating element, which causes a dramatic change in signal amplitude in the vicinity of the resonant frequency. For example, if the sensor is driven at a frequency slightly less that the resonant frequency of the structure, a small increase in the resonant frequency causes and significant drop in the output signal amplitude. Knowing the slope of the frequency response curve, it is possible to estimate the amount of change in the resonant frequency (Figure 7.17). This technique essentially converts a frequency-modulated (FM) signal to an amplitude-modulated (AM) signal and was widely used in FM receivers.

Employing this technique for micromachined devices is not a straight-forward process. The drive signal must be generated by a very stable signal source and its frequency must be carefully set for this technique to work properly. To make matters worse, the resonant frequency of many micromachined devices is a function of pressure, temperature, etc. Therefore, manual intervention and tweaking of the equipment are required in most cases if this technique is to be used. Moreover, the range of the frequencies which can be detected with this method strongly depends on the quality factor of the resonator, which is not an easy parameter to control.

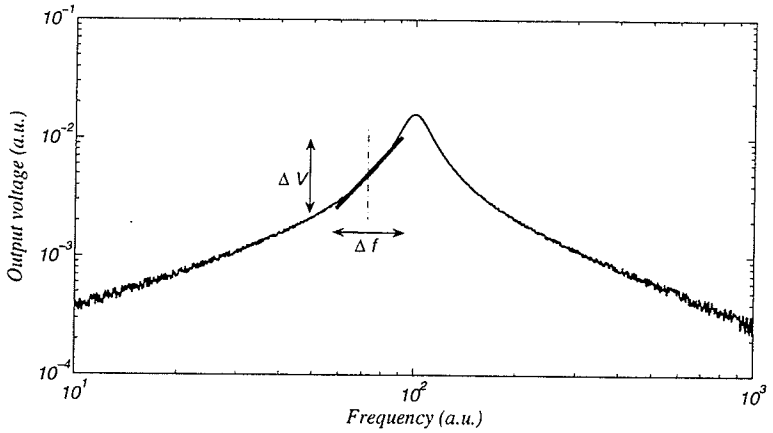

Figure 7.17: *FM to AM conversion.*

Further, a certain amount of time is needed (depending on Q of the structure) for the signal amplitude to build up after a shift in the resonant frequency of the structure. Thereby, this method may not provide enough bandwidth for some applications. Finally, as mentioned in preceding sections, the beating between the main signal and the interfering signals makes the amplitude information of the signal unreliable unless averaging techniques are employed, which adversely affects the measurement bandwidth.

7.5.2 FM to PM conversion

By employing a frequency dependent phase-shift in the signal path, the information embedded in the frequency of a signal can be converted to a phase difference between the original signal and its delayed version. This can potentially improve the accuracy of measurements by converting small frequency shifts to relatively large phase differences. If the amplitude of the signal is controlled, the shifts in the resonant frequency

of the structure are instantaneously converted to phase differences and can be measured. Therefore, sensitivity and bandwidth of measurements are both enhanced by using this technique.

Passive delay networks

Different techniques can be employed to produce a frequency-sensitive phase-shift. An LC tank is an example of an element that can be used for this purpose. The resonant frequency of the tank should be tuned to the signal frequency. Deviations in the frequency of the signal cause the phase difference between the input and output of the tank to vary, which can then be measured with a phase detector as shown in Figure 7.18. The dynamic range and sensitivity of the measurements depend on the quality factor of the elements used in the construction of the tank. It is possible to resolve a $0.01Hz$ frequency shift in a $50kHz$ signal with a $75Hz$ bandwidth when the setup in Figure 7.18 is used in a closed loop [178].

An alternative to a bulky LC tank is a ceramic resonator. In such cases, however, the frequency of the input signal must be within a certain range which is specific to the employed ceramic resonator. Therefore, an up or down conversion of the signal in frequency domain is often required, which adds to the complexity of the system.

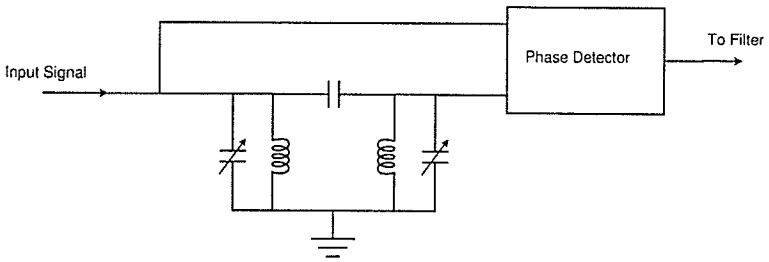

Figure 7.18: *Setup for passive frequency-sensitive phase-shift.*

Active delay networks

As discussed in the preceding section, it is often required to tune the phase shift network parameters with the resonator signal. To avoid the resulting complexities of using passive phase shift networks, it was decided to use the active alternative, which is an allpass (or delay) filter. Allpass filters do not modify the amplitude of the signal through them but will cause a predetermined phase shift at the designed frequency. This is done by properly choosing the location of poles and zeros of the transfer function of the filter. More specifically, the zeros and poles have the same frequency (to produce a flat amplitude response) but the zeros are placed in the right-half portion of the s-plane (to increase the phase difference between high and low frequencies). If allpass networks of orders larger than one are used, it is possible to independently control the frequency and phase performance (i.e., Q) of the circuit. An allpass network of order 2 has the following transfer function:

$$T_{ap}(s) = \frac{s^2 - \frac{\omega_p}{Q_p}s + \omega_p^2}{s^2 + \frac{\omega_p}{Q_p}s + \omega_p^2} \tag{7.2}$$

The effect of the quality factor of the poles and zeros of the transfer function (i.e., Q_p) is illustrated in Figure 7.19.

It is possible to increase the quality factor of the zeros and poles for enhanced sensitivity. However, the improvement in sensitivity of the electronics comes at the expense of reduced dynamic range, since the full scale phase shift (360° for a 2^{nd} order allpass filter) happens over a smaller frequency range. It is also possible to cascade multiple allpass stages to obtain a larger phase shift at a given frequency. This method does not sacrifice the dynamic range for resolution but special care must be

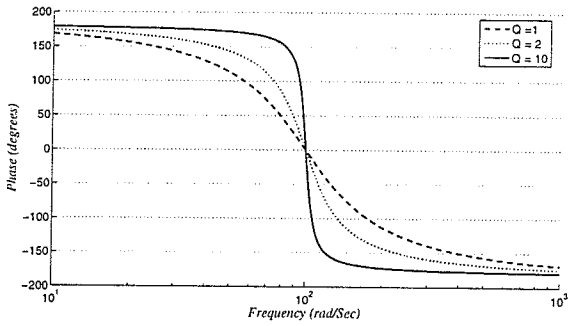

Figure 7.19: *Phase response of a 2^{nd} order allpass filter for different values of Q.*

taken when interpreting the output signal as the output might have undergone several 360° phase shifts which are not detectable unless the changes of the output signal are tracked.

Phase difference detection

The frequency dependent phase difference can be detected using various techniques [179, 180]. If the signals are converted to digital format, an Exclusive-OR (XOR) gate can be used to for this purpose (Figure 7.20). The DC component of the output voltage of the XOR gate is linearly proportional to the phase difference between its two inputs (for $0 \leq \phi < \pi$).

An analog mixer can also be used for phase difference detection (Figure 7.21). If

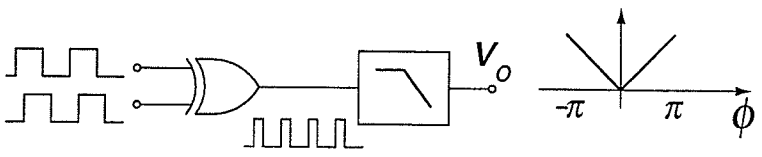

Figure 7.20: *Digital phase detector.*

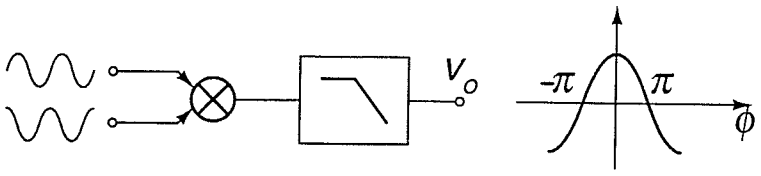

Figure 7.21: Analog phase detector.

the inputs to the mixer are $A \sin\omega t$ and $B \sin(\omega t + \phi)$, the output is given by:

$$v_{out} = KAB \sin\omega t \sin(\omega t + \phi) = \frac{KAB}{2}(\cos\phi - \cos(2\omega t + \phi)) \tag{7.3}$$

where K is the mixer gain. The high frequency component can be easily filtered and the output of the filter is a nonlinear function of the phase difference between the two signals.

It should be noted that there are other circuits for detecting the phase difference between two signals for extended linear range which are not discussed here [179,180].

Frequency shift measurement circuitry

If the phase difference detection is to be done at the signal frequency, high-Q allpass filters are required. For example, if it is desired to have a 45° phase shift for a $1Hz$ of change in the frequency of $40kHz$ signal, a 2^{nd} order allpass filter with a Q of about 6000 is needed, which is obviously difficult to realize. On the other hand, high-Q filters are generally prone to instability. Furthermore, tuning of high-Q filters is not easy because of their narrow bandwidth. To overcome these issues, a mixer is used to bring down the frequency of the resonator signal before feeding it to the delay circuitry. This reduction in signal frequency, which is essentially the same as removing the frequency offset that does not convey information, allows for performing sensitive

phase difference measurements with relatively low-Q allpass filters. Additionally, if the difference between the mixing signal and the sensor signal is kept constant, a stable and tuned circuit can be designed to produce the delay at the difference frequency, which greatly improves the versatility of the sensing electronics. This technique is similar to what is done in superhetrodyne receivers, where a tuned IF stage is carefully designed for a certain frequency range and all of the RF signals at the input of the receiver are mapped onto this frequency range with the aid of a local VCO and a mixer.

The circuit designed for measuring the shifts in the resonant frequency of the sensor is shown in Figure 7.22. The input signal is first filtered to remove unwanted high frequency signals. A mixer brings down the frequency of the signal to what the delay network is designed for ($100Hz$ in this case). The mixer output is then filtered to rid of high frequency components. The delay network consists of two cascaded allpass filters with a center frequency of $100Hz$ and quality factor of 5. Cascading of the allpass filters was mainly done to increase the sensitivity of the delay network. The sensitivity of the cascaded filters is almost the same as a single allpass filter with a Q of 10. However, the achievable dynamic range of the cascaded filters is twice as much as the the circuit with a single high-Q filter due to the doubling in the total number of poles and zeros. Moreover, adjusting the parameters of a relatively low-Q filter is easier than high-Q filters. The original and delayed versions of the signal

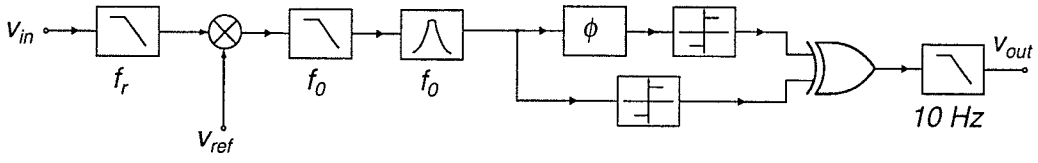

Figure 7.22: *Frequency shift measurement circuit.*

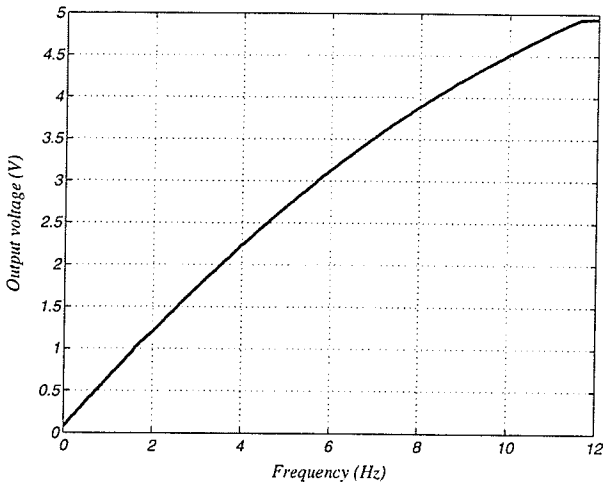

Figure 7.23: The output voltage of the frequency shift measurement circuit versus the difference between the input and reference signal frequencies.

are then converted to square waves and their relative phase is measured with an exclusive-OR (XOR) gate. The output of the XOR gate is filtered to obtain the DC value of the signal which is proportional to the phase difference between the signals

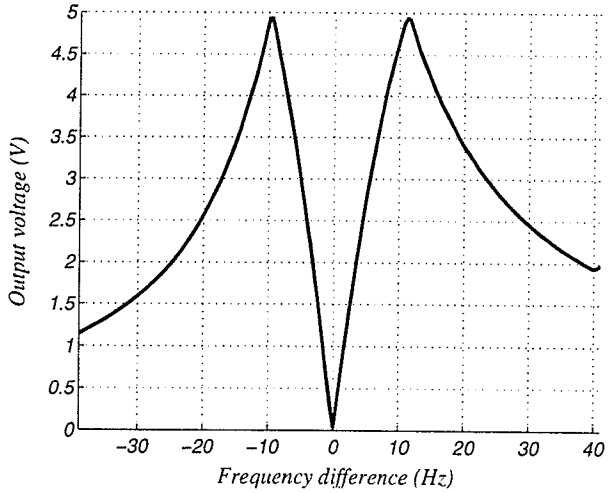

Figure 7.24: The output voltage of the frequency shift measurement circuit versus the difference between the input and reference signals.

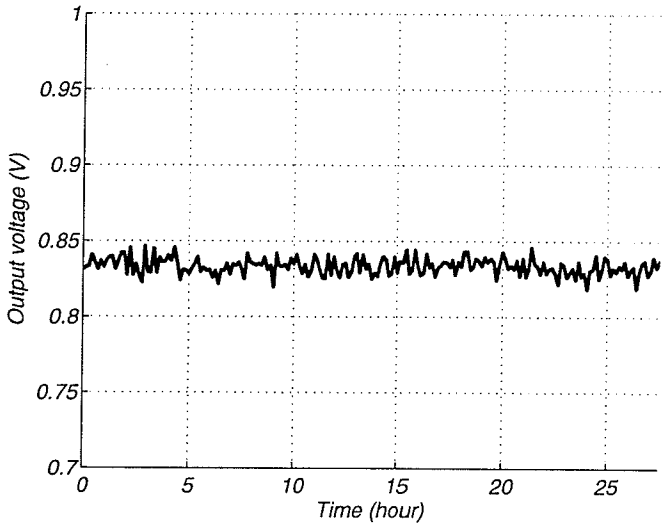

Figure 7.25: *Output voltage noise.*

at the inputs of the XOR gate. The frequency response of this last filter sets the bandwidth of measurements for the whole system.

Figure 7.23 shows the measured output of the circuit when the difference between the input and reference signal frequencies in Figure 7.22 changes from 0 to $12Hz$. This experiment shows an almost linear gain of $0.87V/Hz$ for small frequency shifts. The observed deviation of the response of the circuit from a line is due to the phase response of the allpass circuits. Figure 7.24 illustrates this better with the input frequency varied over a wider range. As expected, the total phase change from the poles and and zeros of the cascaded 2^{nd} order allpass filters approaches to 4π. Figure 7.25 shows the noise of the output voltage of the circuit. The standard deviation of the noise at the output, which sets the minimum detectable signal, is $5.4mV$. Using the sensitivity value of $0.87V/Hz$ for small frequency shifts, it can be seen that the frequency resolution of the circuit in Figure 7.22 is $6mHz$ with a $10Hz$ bandwidth for the output lowpass filter.

7.6 Sensing electronics

The complete sensing electronics is shown in Figure 7.26 with details given in Appendix C. The mixing signal can be produced with another micromachined electrostatic resonator whose resonant frequency can be controlled. The resonant frequency of electrostatic resonators can be modified by applying a bias to their shuttles or by heating them up. Frequency tuning should be performed only once to make sure that the resonant frequencies of the two structures are spaced as required by the frequency shift measurement circuitry. The whole process can be automated in a feedback loop where the frequency of the mixing signal is changed until a certain phase shift is produced at the output of the delay network. The sensor may then be used to measure a magnetic field. It is noteworthy that the frequency of the mixing signal should not be affected by magnetic fields to avoid measurement errors.

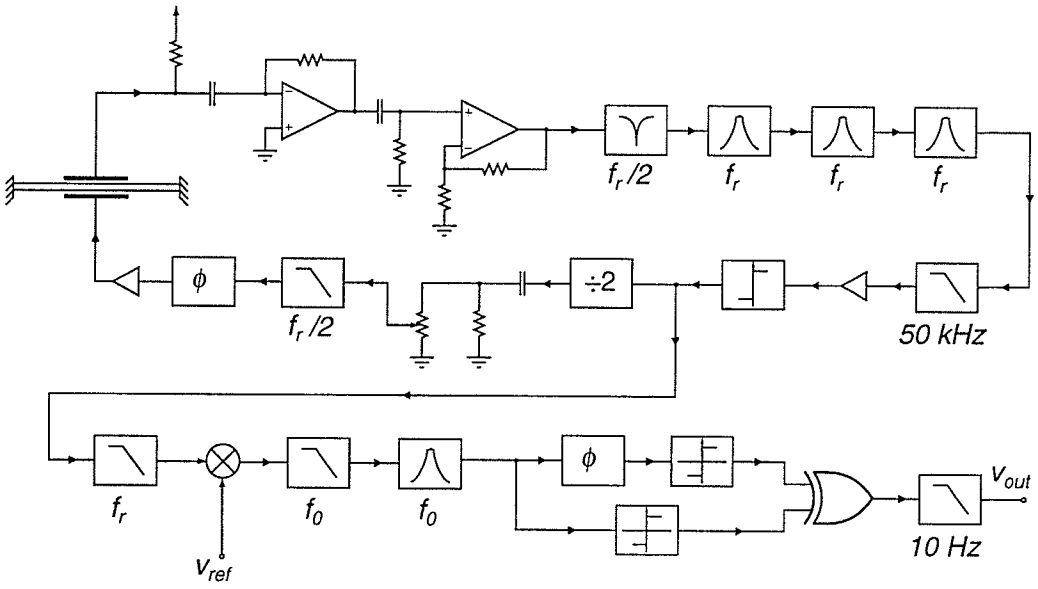

Figure 7.26: *Sensing electronics.*

Chapter 8

Noise

Noise proves nothing.

Mark Twain

Dissipation of energy in physical systems leads to generation of noise. Operation of microelectromechanical systems often involves interactions of multiple physical domains, which translates into addition of new energy and dissipation sources [181, 182]. The most familiar type of noise in micromechanical systems is Brownian noise, which is similar to the thermal noise of electric resistors. The source of this noise is random motion and vibration and impingement of particles (e.g., ambient gas molecules, photons, and phonons). Brownian noise can be considered as a white noise for normal operating frequencies of mechanical structures. Derivation of the model for this noise source is briefly presented [183, 184].

The other noise source which affects the operation of this sensor is shot noise [185, 186]. As described in chapter 2, a DC current flows through the crossbars. When inside a magnetic field, the shot noise of this current causes exertion of a noise force on beam springs. This noise force will cause fluctuations in the resonant frequency of the shuttle, and therefore, contributes to phase noise and spreading of the output signal spectrum.

In addition to these two noise sources, one should also consider the noise introduced by the signal processing electronics. As will be shown later, this noise actually dominates the total noise performance of the system and brings up the noise floor at the output. Methods to improve the signal to noise ratio will be proposed.

Finally, environmental disturbances and aging of the equipment also act as noise for long term measurements. This noise is usually called random walk. The main difference between random walk and other sources of noise is that its effect cannot be removed by integration. In particular cases, it is possible to reduce the effects of random walk by proper characterization of the measurement system and further processing of the signal in software.

8.1 Resonator noise

The two sources of electromechanical noise of the mechanical resonators are the Brownian motion of gas molecules and the shot noise of the current in crossbars. For this analysis, the dissipation of energy through thermoelastic and anchor losses are ignored. These losses are generally much smaller than the Brownian noise from impingements of gas molecules unless the resonator is operated under ultra high vacuum

(e.g., $\approx 10^{-9} Torr$) [110]. Furthermore, it is assumed that the only source of the Brownian noise is the impingement of gas molecules on the structures; i.e., the effect of phonons, photons, and other particles on the the total Brownian noise of the device is assumed to be insignificant.

8.1.1 Brownian noise

The effects of this noise source on the performance of micromachined structures has been researched extensively [110, 150, 187–190]. To illustrate how the power spectral density of this noise is derived, the procedure in reference [191] is summarized here. If the noise is represented by a force, $F(t)$, the spectral density of this force, $J(\omega)$, is found from:

$$J(\omega) = \int_{-\infty}^{+\infty} \langle F(t)F(t+\tau)\rangle e^{-j\omega\tau}\, d\tau$$
$$\langle F^2\rangle = \langle F(t)\, F(t)\rangle = \int_{-\infty}^{+\infty} J(\omega)\, d\omega = \int_{0}^{+\infty} J^{+}(\omega)\, d\omega \tag{8.1}$$

where the last integral is restricted to positive frequencies only by defining $J^{+}(\omega) = 2J(\omega)$. This is permissible since $J(\omega)$ is a real and even function of frequency [191]. It turns out that $J(\omega)$ is constant for a wide frequency range, and therefore, can be considered as a white noise source [192].

For harmonic motion of a mass-spring system as described by equation 3.1, we have:

$$X = \frac{F}{-M\omega^2 + j\omega\zeta + K} \tag{8.2}$$

Therefore, the mean value of kinetic energy is given by:

$$\langle \frac{1}{2} M\dot{x}^2 \rangle = \frac{1}{2} M \left\langle \left| \frac{j\omega F}{-M\omega^2 + j\omega\zeta + K} \right|^2 \right\rangle = \frac{M}{2K^2} \int_{-\infty}^{+\infty} \frac{F^2\omega^2 \, d\omega}{(1 - \frac{\omega^2}{\omega_0^2})^2 + \frac{\omega^2}{Q^2\omega_0^2}}$$
$$= \frac{J^+\omega_0}{2K} \times \frac{Q\pi}{2} \tag{8.3}$$

where $\omega_0 = \sqrt{K/M}$, $Q = \omega_0 M/\zeta$, and we used the fact that J^+ is frequency independent [183, 191].

The equipartition theorem states that each independent quadratic term in the total energy of a system has a mean value of $K_B T/2$ where K_B is Boltzmann's constant [191, 192]. The spectral density of the noise force can now be found from equation 8.3 by using equipartition theorem:

$$\frac{J^+\omega_0}{2K} \times \frac{Q\pi}{2} = \frac{1}{2} K_B T$$
$$\implies \quad J^+ = \frac{2}{\pi} K_B T \zeta \tag{8.4}$$

If the integral of equation 8.3 is taken with respect to frequency f rather than the radian frequency ω, this familiar result is obtained for the mean square value of the spectral density of the noise force:

$$J^+ = \tilde{f_B}^2 = 4K_B T\zeta \qquad N^2/Hz \tag{8.5}$$

It must be noted that other choices of a system frequency response would result in the same frequency distribution for the spectral density of the noise. Choosing a second degree system in this case merely allowed us to specify different quantities in

terms of familiar parameters Q and ω_0. The noise force is shaped by the frequency response of the system under analysis, and therefore, the total amount of noise at the output of a system will depend on its bandwidth. The other point of interest is proportionality of the amount of Brownian noise force to the square root of the damping factor, ζ. The damping factor itself , however, is a function of pressure (see section 3.6). Thereby, besides operating at low temperatures, the only method to reduce Brownian noise is to operate the sensor at lower pressures (i.e., vacuum). This is not a surprising result, as the origin of Brownian noise in this analysis was the impingements of gas molecules on the surfaces of a structure. A similar result is obtained for the Johnson (thermal) noise in electric circuits. Johnson noise is produced by random motion of electrons inside the material. The power spectral density of the voltage noise produced by a resistor in an electric circuit is given by $4K_BTR$.

To calculate the produced noise force, the effective damping coefficient should be calculated. As discussed in Section 3.6, the two sources of dissipation are Couette, ζ_c, and squeezed film damping, ζ_{sf}. Formulas for these two damping mechanisms are:

$$\zeta_c = \eta_{eff}\frac{A}{g} \tag{8.6}$$

$$\zeta_{sf} = \frac{96}{\pi^4} \times \frac{\eta_{eff} L W^3}{g^3} \tag{8.7}$$

where η_{eff} is the effective viscous coefficient of the ambient gas, A is the surface area between the moving structures, g is the gap between the moving plates, L is the length of the moving beam, and W is its width.

Squeezed film damping should be considered when two plates are moved toward each other. For comb-drive resonators, the movements of the ends of the fingers

toward stationary sidewalls gives rise to squeezed film damping. However, the distance between the ends of the moving comb fingers and the fixed sidewalls of the stationary comb is quite large compared to the interacting area between the two. Therefore, the amount of squeezed film damping turns out to be small and can be ignored, meaning that Couette damping is the main cause of energy dissipation during sensor operation.

The damping coefficient can now be calculated from:

$$\zeta = \zeta_c = \eta_{ss} \frac{A_{sh}}{g_{ss}} + 4\,\eta_{ff}\, N_f \frac{h\, L_{eng}}{g_f} \tag{8.8}$$

where A_{sh} is the area of the shuttle, g_{ss} is the gap between the shuttle and the substrate, N_f is the number of fingers on each side of the shuttle, h is the thickness of the structure, L_{eng} is the initial amount of finger engagement, and g_f is the gap between fingers. η_{ss} and η_{ff} are the effective viscosities for gas flow between the shuttle and the substrate and between the fingers. Equation 8.5 can now be used to calculate the total noise force acting on the shuttle of the sensor for planar motion. The Brownian motion of the shuttle manifests itself as an amplitude noise in the output current of the shuttle. If the resonator is used in oscillator configuration, however, the noise power is equally divided between amplitude and phase noises [193].

8.1.2 Shot noise

The existence of shot noise is due to the random arrival of electrons in a current conducting wire when the electrons have to pass through a potential wall; e.g., across the depletion region of a *pn* junction. Shot noise is always associated with a DC

current [186]. The amount of this noise is proportional to the number of electrons that pass through the wire at a given time, or in other words, the current. It can be shown that the power spectral density (PSD) of this noise is given by [185, 186]:

$$\tilde{i}_S^2 = 2q_e I_{DC} \qquad A^2/Hz \tag{8.9}$$

where I_{DC} is the mean value of the current and q_e is the magnitude of electronic charge ($1.6 \times 10^{-19} C$).

In presence of a magnetic field, the disturbances of the DC current flowing through the crossbars cause axial force fluctuations, and therefore, affect the resonant frequency of the device. The effect of this noise can be calculated by using the derived equations for the sensitivity of the sensor to the axial force. Shot noise in crossbars manifests itself as an additional source of phase noise at the output of the sensor.

8.2 Electronics noise

Electronics noise can be modeled by adding voltage and current noise sources to the circuit models of amplifiers and filter blocks in the system. The noise sources inside an amplifier block are generally referred to its inputs. To be able to model the amplifier

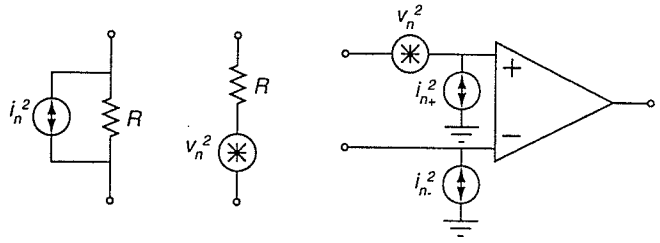

Figure 8.1: *Electronic noise source models for resistors and amplifiers.*

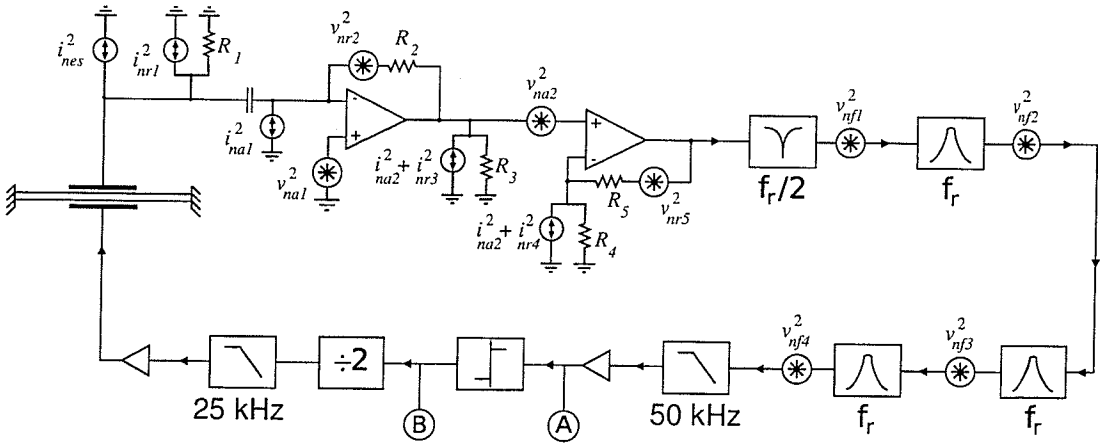

Figure 8.2: *Noise sources in the oscillator loop.*

noise for different configurations, both current and voltage sources are added to the inputs of amplifiers. At our frequency range of interest, the main sources of electronic noise are the Johnson (thermal) noise in resistors and flicker noise in active devices. The Johnson noise of resistors is modeled by adding either a voltage source, $4K_BTR$, in series or a current source, $4K_BT/R$, in parallel with them. Figure 8.1 illustrates the circuit models of amplifiers and resistors for noise calculations in circuits.

The circuit model of the oscillator loop for noise analysis is shown in Figure 8.2. To simplify the diagram and the analysis, the noise of the amplifiers is referred to their inputs and is represented by a combination of a noise voltage source and noise current sources. The noise sources are assumed to be uncorrelated. As will be seen, the large Q of the electrostatic resonator directly affects the noise performance of the circuit (the quality factors of the three bandpass filters are 50, 20, and 20, respectively, compared to the typical Q value of 15000 for the electrostatic resonator for the same center frequency). Also, it should be remembered that the notch filter was needed to remove the large interfering signal, which does not exist in our simplified model.

In Figure 8.2, sources i_{nrk} or v_{nrk} represent the Johnson noise of the resistors R_k, sources i_{nak} and v_{nak} represent the internal noise of the k^{th} amplifier, and finally, v_{nfk} is the output noise of the k^{th} filter. For noise calculations, we will use the fact that when a signal with power spectral density of $S_{ni}(f)$ goes through a system $H(s)$, the power spectral density of the noise at the output of the system is given by $S_{no}(f) = |H(f)|^2 S_{ni}(f)$ [134, 194].

In Figure 8.2, i_{nes} is the Brownian noise of the output current of the resonator with a power spectral density given by:

$$i_{nes}^2 = \left(V_B \frac{\partial C}{\partial y}\right)^2 \left|\frac{\omega}{-M\omega^2 + j\,\zeta\omega + k}\right|^2 f_n^2 \tag{8.10}$$

where $f_n = \sqrt{4K_BT\zeta}$. The power spectral density of the noise at the outputs of the blocks before the comparator is given by:

$$v_{noa1}^2 = \left(i_{nes}^2 + i_{na1}^2 + i_{nr1^2}\right) R_2^2 + v_{nr2}^2 + v_{na1}^2 \left(1 + \frac{R_2}{R_1}\right)^2 \tag{8.11}$$

$$v_{noa2}^2 = \left(v_{noa1}^2 + (i_{nr3}^2 + i_{na2}^2)R_3^2 + v_{na2}^2\right) \left(1 + \frac{R_5}{R_4}\right)^2 + (i_{nr4}^2 + i_{na2}^2)R_5^2 + v_{nr5}^2 \tag{8.12}$$

$$v_{nof1}^2 = v_{noa2}^2 + v_{nf1}^2 \tag{8.13}$$

$$v_{nofi}^2 = \left|G_i \frac{j\frac{\omega_0}{Q_i}\omega}{-\omega^2 + j\frac{\omega_0}{Q_i}\omega} + \omega_0^2\right|^2 v_{nof_{i-1}}^2 + v_{nfi}^2 \quad , \quad \text{for i=2, 3, and 4} \tag{8.14}$$

$$v_{nof5}^2 = \left|\frac{1}{\sum_{n=0}^{4} a_n \left(\frac{j\omega}{2\pi 50000}\right)^n}\right|^2 v_{nof4}^2 \tag{8.15}$$

where v_{nof5} is the output of the 4^{th} order Butterworth lowpass filter with a cutoff frequency of $50kHz$ and a_n are the coefficients of the normalized transfer function of the filter.

The root-mean-square (RMS) value of the voltage noise at the input of comparator, node A, can be found from:

$$v_{nA_{rms}} = \sqrt{\int_0^\infty v_{nof5}^2 \, df} \tag{8.16}$$

As an example, for a $1V$ actuation signal and a $30V$ bias voltage on the output comb for a resonator with a Q of 15000 and resonant frequency of $29.881kHz$ (device d), the RMS value of the output noise current of the resonator is $460fA$, which is added to a signal current of $5.41nA$. The total RMS noise voltage at the input of the comparator (node A) from the resonator and the electronics is $9.1mV$ on top of a $4.76V$ signal.

The Brownian noise from the resonator produces $283\mu V$ at the input of the comparator. The noise voltages produced by i_{nr1}, v_{nr2}, i_{na1}, v_{na1}, and v_{nf4} at the input of the comparator are $1.5mV$, $4.8mV$, $105\mu V$, $477\mu V$, and $649\mu V$, respectively. It can be seen that the noise produced by the resonator is small compared to the noise of circuit components, especially resistors R_1 and R_2 and the last filter. Refer to Appendix C for details on electronic components used for realization of the required transfer functions.

The noise added by the circuit blocks between the comparator and the resonator is negligible compared to the noise by the blocks preceding the comparator (i.e., the noise added by the lowpass and delay filters before the resonator is $3.7\mu V$).

8.3 Oscillator loop noise

The prevailing method of characterizing the noise in oscillators is by specifying their phase noise. Phase noise has been defined as [195, 196]:

$$\mathcal{L}(f) = \frac{\text{power density in one phase noise modulation sideband, per Hz}}{\text{total signal power}} \tag{8.17}$$

Analysis of the phase noise in linear oscillators has been thoroughly investigated [193, 197–203]. In case of nonlinear oscillators, the analysis is usually limited to ring oscillators or to the nonlinear behavior of the devices in the oscillator loop (e.g., the drain current of the transistor in Pierce oscillators) [204–207]. Linear oscillators are usually analyzed with the aid of transfer functions of the components in the loop and linearizing of the nonlinear elements about their operating point. The analysis of linear oscillators, therefore, is usually performed in the frequency domain. This is not possible for the case of our oscillator loop due to the extremely nonlinear behavior of elements in the loop: the operation of a comparator cannot be linearized, the force to voltage transfer function is quadratic, and there is no transfer function for a frequency divider. In fact, the mere existence of frequency division means that the linear or purely frequency domain analysis is not permissible. On the other hand, time domain analysis of the loop is not simple, since in addition to the nonlinear elements, there are 10 second order systems in the loop.

Numerical simulation of the noise behavior of the system is not a simple task either. The goal of simulations will be to investigate the output spectrum of the oscillator with a resolution on the order of a few mHz around a $30kHz$ to $50kHz$ signal. Therefore, when using numerical simulations, the frequency resolution needs to

be on the order of mHz. To achieve such a frequency resolution, the discrete Fourier transform (DFT) has to be performed on a large number of data points. For example, the minimum sampling frequency to have a $1mHz$ resolution around a $40kHz$ signal is $2 \times 1000 \times 40000 = 80MHz$, where the factor 2 is to satisfy the Nyquist theorem requirements. On the other hand, the spectrum purity of the signal is sacrificed if the DFT is performed on a small number of cycles of the signal. Considering these points, it can be seen that the numerical simulation of the oscillator performance quickly becomes computationally prohibitive.

The noise performance of the oscillator loop is studied using a combination of frequency and time domain analyses. The analysis of the behavior of nonlinear elements is performed in time domain and the rest of the loop is analyzed in frequency domain. For this analysis, the simplified schematic shown in Figure 8.3 will be used. In this figure, amplifier K_1 represents the amplifiers, the response of the bandpass filters is combined into one block, with Q_{ei} being the quality factor of bandpass filter i with a gain of G_i, the noise source x_n represents the all of the electronic noise before the comparator, the noise source z_n represents the all of the electronic noise after the comparator, the voltage to electrostatic force conversion is represented by block u^2, the gain block K_2 stands for all of the gain before the resonator and the force-to-current conversion factor of the resonator, and finally the electrostatic resonator response is represented by a second order block. The loop is opened between points 1 and 7 for the noise analysis. In this loop, a sinusoidal signal with frequency ω_0 goes through the loop without a phase shift. The amplitude, however, is set by the response of the comparator, which depends on the logic voltage levels, U, and the gain of the amplifier K_2. The notch filter is assumed to not affect the signal response

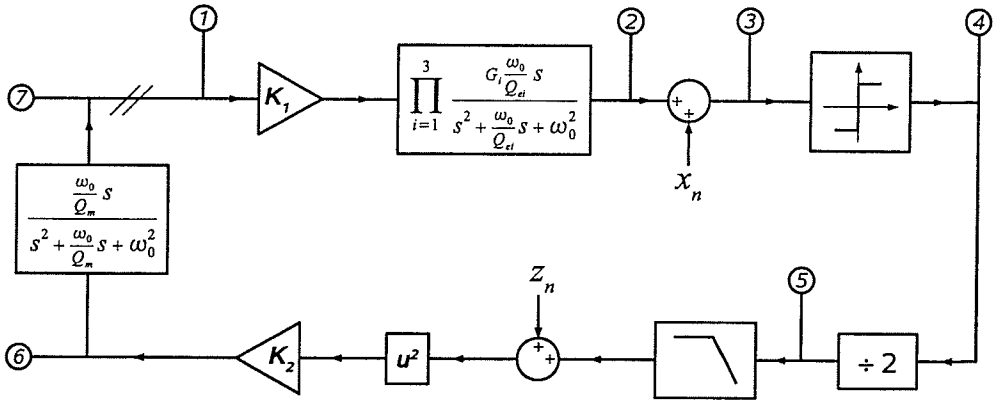

Figure 8.3: *Schematic of the simplified loop.*

at the frequency band of interest (except for the added noise).

The effect of the loop response is initially investigated on a signal with a frequency slightly different from the resonant frequency of the resonator; i.e., $\omega = \omega_0 + \Delta\omega$. Assume that $y_1 = A\cos\omega t$ and $x_n = z_n = 0$, where $A = K_2 U$. The signal before the comparator is given by:

$$\begin{aligned} Y_3 =& K_1 Y_1 H_e(j\omega) \\ =& K_1 Y_1 \prod_{i=1}^{3} G_i \frac{j\frac{\omega_0}{Q_{ei}}\omega}{\omega_0^2 - \omega^2 + j\frac{\omega_0}{Q_{ei}}\omega} \end{aligned} \tag{8.18}$$

where Y_i is the phasor representation of the signal y_i. The phase of the signal at node 3 is:

$$\angle Y_3 = \frac{3\pi}{2} - \sum_{i=1}^{3} \arctan \frac{\frac{\omega_0}{Q_{ei}}}{\omega_0^2 - \omega^2} \tag{8.19}$$

The comparator does not change the phase of the signal. The frequency divider block reduces the phase of the signal by half. However, when the lowpass-filtered signal is converted to electrostatic force, the original phase of the signal is recovered.

Therefore, $y_6 = K_2 U \cos(\omega t + \angle Y_3)$, where U is the amplitude of the filtered signal after the frequency divider. It follows that:

$$|Y_7| = K_2\, U \frac{\frac{\omega_0}{Q_m}\omega}{\sqrt{(\omega_0^2 - \omega^2)^2 + (\frac{\omega_0}{Q_m}\omega)^2}}$$

$$\angle Y_7 = 2\pi - \arctan\left(\frac{\frac{\omega_0}{Q_m}}{\omega_0^2 - \omega^2}\right) - \sum_{i=1}^{3} \arctan\left(\frac{\frac{\omega_0}{Q_{ei}}}{\omega_0^2 - \omega^2}\right) \tag{8.20}$$

meaning that the signal at node 7 is destructively added to the original signal. Therefore, it can be concluded that the phase noise in the loop *does not* build up.

The effect of amplitude noise on phase noise performance of the oscillator loop is analyzed below. Assume that the signal at node 1 is $y_1 = A\cos\omega_0 t$ and the signal x_n is what was calculated in equation 8.15. The comparator converts the amplitude noise in signal at node 3 to phase noise. Figure 8.4 illustrates this by applying a noisy voltage to the input of an ideal comparator. In practice, the comparator cannot follow the fast transitions at its input and the output transitions in Figure 8.4 are converted to changes in the output pulse width; i.e., phase noise. Remembering that a single pulse is produced at the output of the frequency divider for every two pulses at its input, the phase noise should be analyzed at only one of the two zero-crossing points in each cycle of the input signal. For small fluctuations relative to the amplitude of the signal, the amount of phase noise when a noise voltage, v_{n3}, is added to the input voltage of the comparator, v_3, is given by:

$$\delta t = v_{n3}\left(\frac{dv_3}{dt}\right)^{-1}$$

$$\Rightarrow \quad \phi_n = \omega_0\, \delta t = \omega_0 \frac{v_{n3}}{S} \tag{8.21}$$

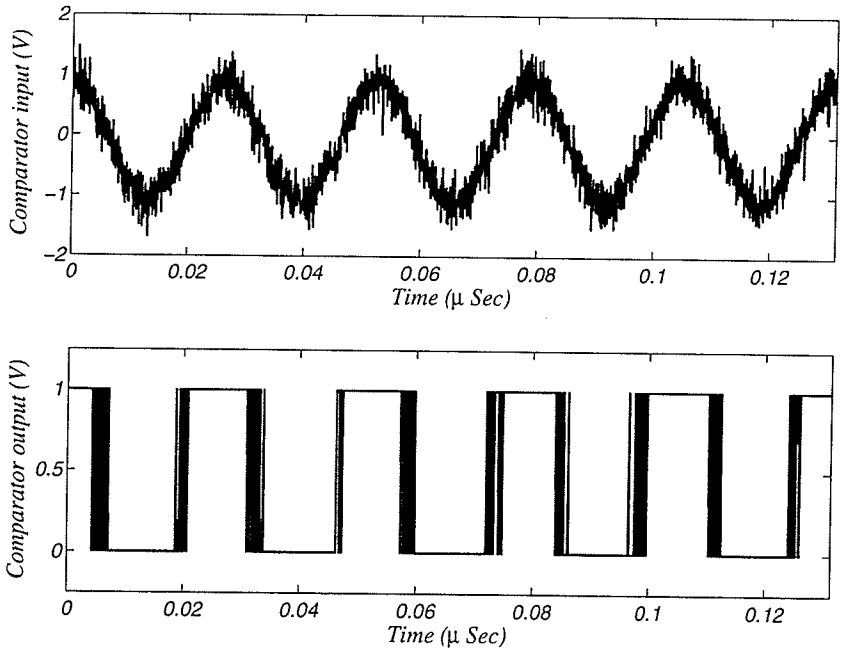

Figure 8.4: *Conversion of amplitude noise to phase noise.*

where δt is the time difference between the zero-crossing points of the noiseless and noisy signals and S is the slope of the signal at zero-crossing point. The random fluctuations of amplitude at the zero crossing points of the noisy waveform cause random phase disturbances. Assuming that the spectral density of the phase variations is wide-sense stationary, it follows from statistical arguments that $S_\phi(f) = \vartheta \left(\frac{f_0}{S f}\right)^2$ where $S_\phi(f)$ is the PSD of the phase fluctuations, f is the Fourier frequency, and ϑ is a constant that depends on the type of the oscillator (e.g., harmonic, relaxation, etc.) [202].

The signal goes through a frequency divider after the comparator. When the frequency of a signal is multiplied by n, the phase noise increases by n^2 [193]. Ignoring the noise introduced by the lowpass filter, the frequency of the signal is multiplied

by two when it goes through the u^2 block (voltage to electrostatic force converter). Therefore, after the nonlinear blocks the phase noise in the signal is the same as what it was after the comparator and the signal at node 6 will be $y_6 = K_2\, U\, \cos(\omega_0 t + \phi_n)$. It should be noted that the bandpass filters do not contribute to the phase, as the frequency of their input signal is ω_0.

The phase noise of the signal at the resonator input is half of the spectral density of phase fluctuations and is given by $\mathcal{L}(f) = \frac{1}{2} S_\phi(f)$ [208]. Since $\omega = \frac{d\phi}{dt}$, the spectral density of frequency deviations is : $S_y(f) = f^2\, S_\phi(f)$ where f is the Fourier frequency.

Amplitude noise after the frequency divider is shaped by the transfer function

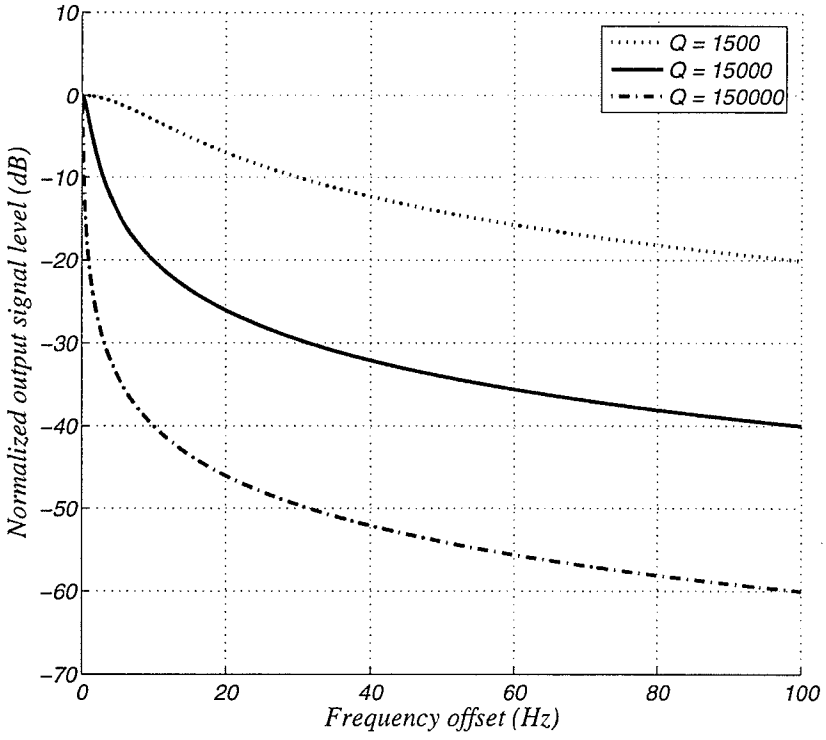

Figure 8.5: *Phase noise at the output current of the sensor for different values of resonator quality factor.*

of the resonator. The signal after the resonator at a frequency offset $\Delta\omega$ from the resonant frequency of the device, ω_0, is given by:

$$y_7 = K_2\, U \frac{\frac{\omega_0}{Q_m}\left(\omega_0 + \Delta\omega\right)}{\sqrt{\left(\omega_0^2 - (\omega_0 + \Delta\omega)^2\right)^2 + \left(\frac{\omega_0}{Q_m}(\omega_0 + \Delta\omega)\right)^2}} \cos\left((\omega_0 + \Delta\omega)\, t + \theta\right) \quad (8.22)$$

where $\theta = \frac{\pi}{2} - \arctan\left(\frac{\frac{\omega_0}{Q_m}(\omega_0+\Delta\omega)}{\omega_0^2-(\omega_0+\Delta\omega)^2}\right)$.

The normalized phase noise of the system due to amplitude variations at the input of resonator for different values of mechanical Q-factor for the resonator is plotted in Figure 8.5. It should be noted that equation 8.22 predicts the phase noise for an open loop oscillator. Consequently, if the open loop quality factor is used in this equation, the estimated phase noise spectrum of the oscillator will be much wider than the measured one. This can be verified by comparing the estimated phase noise with the open loop quality factor of the device ($\approx$ 15000) in Figure 8.5 with the measured spectrum in Figure 7.15. In a linear oscillator loop the better performance of the closed loop system can be explained by noticing that the poles of the closed loop system are on the $j\omega$ axis, meaning that signals at the frequency of the oscillations are amplified by a theoretical infinite gain. For the case of our nonlinear oscillator, a discussion based on location of poles is not valid. However, it can be said that to sustain a constant amplitude for the output current of the resonator, the mechanical losses of the resonator are compensated by the loop. Therefore, the effective damping factor of the resonator is greatly reduced inside a loop by the positive feedback; i.e., the Q of the resonator is enhanced.

8.4 Frequency stability

The noise floor of the oscillator loop is too high to allow direct measurement of phase noise of its output signal (see Figure 7.15). Therefore, long term time-domain frequency stability measurements were taken at predefined intervals to characterize the performance of the oscillator loop. Once the dataset of frequency measurements is obtained, the scatter of output frequency values has to be determined as a measure of frequency noise. One could use classical statistics such as standard deviation (or variance, the square of the standard deviation) to quantify the dispersion in signal frequency. However, variance is well defined for stationary data only; i.e., signals whose statistical parameters do not change over time. This is equivalent to assuming that the noise has a white spectral density. For stationary data, the mean and variance will converge to particular values as the number of measurements increases. With non-stationary data, the mean and variance never converge to any particular values. Oscillator data is usually non-stationary, because it contains time-dependent noise contributed by the frequency offset such as environmental disturbances and aging of the components.

For these reasons, a non-classical statistic is used to estimate stability in time domain. The statistics which are often employed to analyze the frequency stability of the oscillators is called Allan variance, also known as two-sample variance [179, 195, 209–211]. Allan variance is defined as:

$$\sigma_y^2(\tau) = \frac{1}{2\,(M-1)} \sum_{k=1}^{M-1} (\bar{y}_{k+1} - \bar{y}_k)^2 \tag{8.23}$$

where M is the number of data points in the dataset. $\bar{y}_k$ is the fractional frequency

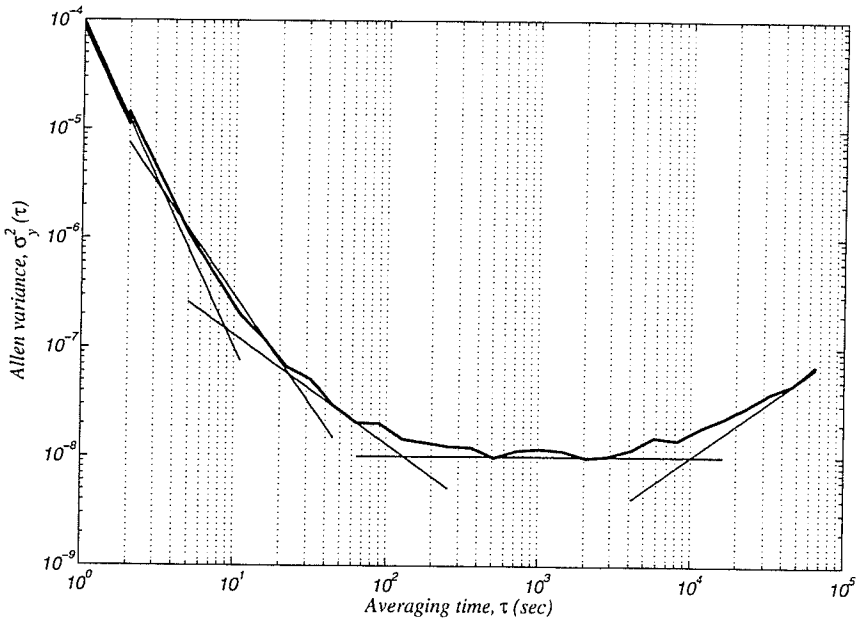

Figure 8.6: *Sample Allan variance plot of an oscillator. The asymptotic lines illustrate the different stability regimes.*

deviation averaged over period τ: $\bar{y} = \frac{1}{\tau f_{nom}} \int_\tau (f - f_{nom})\, dt$ for f_{nom} being the nominal frequency of the oscillator [179, 193, 212]. Allen deviation is the square root of Allen variance.

Figure 8.6 shows the calculated Allan variance for a sample dataset. It can be seen that the stability improves as the measurement (integration) period gets longer. At some point, the oscillator reaches the flicker noise floor and the increasing the integration period no longer improves the signal quality. Environmental disturbances contribute to random walk and the frequency stability deteriorates for very long integration periods.

It is possible to extract information about the type of noise from the Allen variance graphs. The power spectral density of frequency fluctuations is related to Allan

Table 8.1: *The relationship between time and frequency domain data. τ_0 is the initial averaging time and $\tau = n\tau_0$, where n is an integer.*

Type of noise	PSD, $S_y(f)$	Allan variance, $\sigma_y^2(\tau)$
White noise PM	$h_2 f^2$	$\left(\frac{1}{2\pi}\right)^2 3 f_h \tau_0 h_2 \tau^{-2}$
Flicker noise PM	$h_1 f$	$\left(\frac{1}{2\pi}\right)^2 (1.038 + 3 h_1 \ln(2\pi f_h \tau)) \tau^{-2}$
White noise FM	h_0	$\frac{1}{2} h_0 \tau^{-1}$
Flicker noise FM	$h_{-1} f^{-1}$	$2\ln(2) h_{-1} \tau^0$
Random walk FM	$h_{-2} f^{-2}$	$\frac{1}{6}(2\pi)^2 h_{-2} \tau$

variance data according to the following relationship:

$$\sigma_y^2(\tau) = \int_0^\infty 2 \frac{\sin^4(\pi\tau f)}{(\pi\tau f)^2} S_y(f)\, df \tag{8.24}$$

For white and flicker PM noises, the upper limit of the integral has to be set to the bandwidth of the measurement system, f_h, to ensure the convergence of the integral. Table 8.1 summarizes the relationships between the power spectral densities of common types of noise and the Allan variance of the dataset [212–215].

Figure 8.7 compares the Allen variances for the signal at the output of the oscillator loop after the comparator (with device b as the resonator) and the the signal directly taken from the output of a function generator. A Stanford Research Systems synthesized function generator (model DS345) was used for producing a $1V$ sine wave with the same frequency as the oscillator loop. The frequency of the signals was measured using an Agilent 34401A multimeter. Data acquisition software was developed in LabView 7 [216] and used to read and record the output frequency of the circuit at predefined intervals of $2sec$ for several hours. Both measurements were performed after the systems were on and running for $24hr$ to avoid the errors caused by warm-up of the equipment or by the initial changes of the pressure inside the chamber. As can

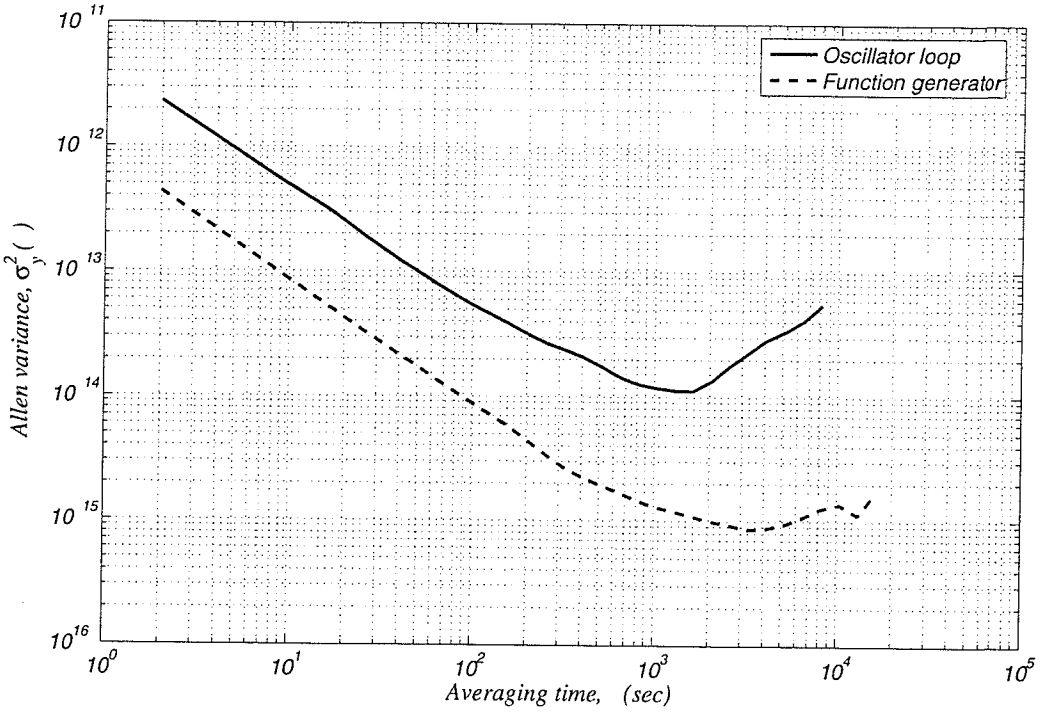

Figure 8.7: *Comparison of Allan variances for the function generator and the oscillator.*

be seen in Figure 8.7, the dominant noise sources contributing to the output phase noise of the oscillator are white frequency noise, flicker frequency noise, and random walk. The total noise in the output of the oscillator loop is higher than that of the function generator. This can be improved by increasing the Q of the resonator and processing the signal with an electronic circuitry with better noise performance. The output of the electrostatic resonator exhibits random walk noise at shorter integration times than the function generator. The most probable cause for this is the changes in the temperature of the environment, which affect the performance of both the resonator and the electronics.

In special cases, the PSD of phase or frequency fluctuations of the oscillator can be extracted from Allan variance data (see Table 8.1). Knowing the the PSD of the

frequency fluctuations, $S_y(f)$, the PSD of phase fluctuations, $S_\phi(f)$, can be calculated from $S_\phi(f) = \frac{f_0^2}{f^2} S_y(f)$, where f_0 is the carrier frequency and f is the Fourier frequency. It must be noted, however, that the transformation between Allan variance and frequency domain parameters is generally not a one-to-one transformation. Therefore, from mathematical point of view, the Allan variance information cannot be mapped into a single set of frequency domain parameters [217,218].

8.5 Total noise behavior

The uncertainty in the output signal of the complete sensory system depends on the noises of the oscillator loop and the frequency shift measurement circuitry. It can be seen from the Allan variance of the data for frequency stability analysis of the oscillator loop that the best frequency resolution is $2.9mHz$ for device d for an integration time of about $1000sec$. Therefore, the magnetic field resolution for this sensor is $32.56\mu T$ if the output frequency of the loop is measured with a frequency meter.

If the frequency shift measurement circuitry with the active delay filters is used, the additional noise produced by that circuit should be taken into account. The uncertainty produced in readings of this circuit are from the noise produced by the mixer, filters and, more importantly, the noise induced on the supply line by the switching of the comparators and logic circuits. As an example, the simulated noise at the output of each of allpass filters is shown is shown in Figure 8.8. The empirical formula for the output noise of the delay filters is:

$$v_{napf}^2 = (15.84 \times 10^{-9})^2 + \left(858 \times 10^{-9} \left| \frac{j \frac{\omega \omega_0}{Q}}{\omega_0^2 - \omega^2 + j \frac{\omega \omega_0}{Q}} \right| \right)^2 \quad V^2/Hz \qquad (8.25)$$

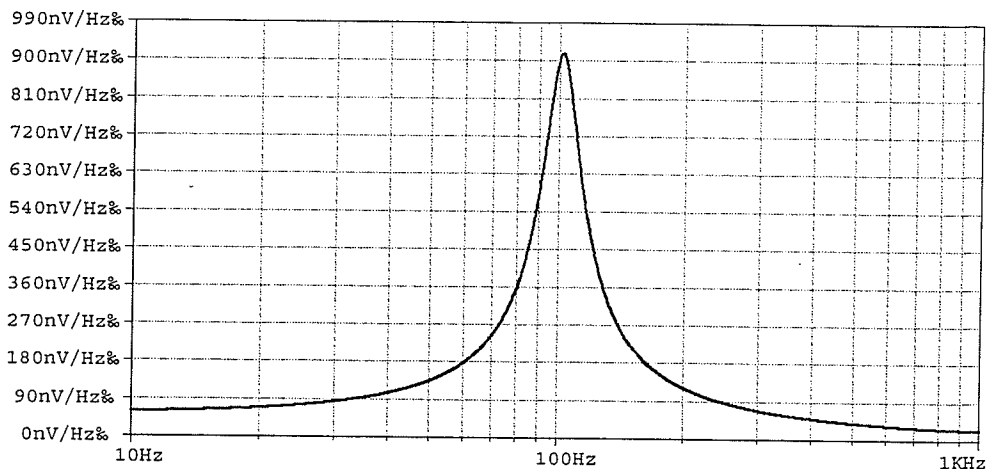

Figure 8.8: *Output noise voltage of each of the allpass filters.*

where $\omega_0 = 200\,\pi$ and $Q = 5$.

The output voltage of the circuit was measured to be stable within $5.4mV$ of its mean value (see Figure 7.25). Considering that the frequency shift measurement network has a gain of $0.87V/Hz$, this value of noise limits the minimum detectable frequency shift to $6.2mHz$. For device d that we used for our discussion of noise, total noise of the system causes an error of $6.8mHz$ in frequency shift measurements, and consequently, $\pm 77\mu T$ in the readings of the magnetic field.

8.6 Other signal detection techniques

The signal detection method can be altered to achieve better noise performance. Instead of using the resonator inside an oscillator loop, it can be driven by a signal source and the shifts in the resonant frequency can be monitored externally. One can use sine fitting algorithms to estimate the frequency of the signal based on samples from a few cycles.

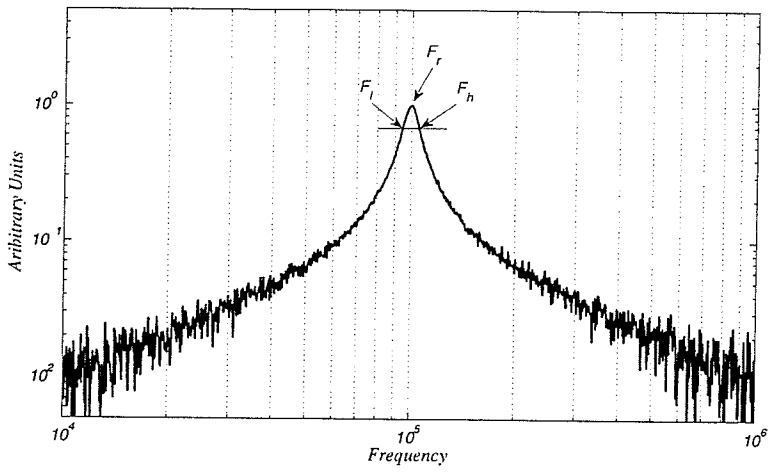

Figure 8.9: *Output spectrum of the output current of the resonator in presence of noise.*

To provide insight into the noise performance of the sensor, the case where the output signal of the driven sensor is monitored with a noiseless spectrum analyzer is investigated. In this case, the frequency of the input signal is slowly swept around the resonant frequency of the resonator. The resonant frequency of the sensor is taken to be the mean value of the frequencies where the amplitude of the output signal drops by $-3dB$. The drive signal is kept small enough to avoid the nonlinearities in the frequency response of the resonator.

An example for the expected waveform for the output current of a second order resonator is shown in Figure 8.9. The transfer function of the system is assumed to be:

$$\frac{I_{out}(j\,\omega)}{F_{in}(j\,\omega)} = \frac{V_B}{\zeta}\left(\frac{\partial C}{\partial y}\right)\frac{j\,\frac{\omega\,\omega_0}{Q}}{\omega_0^2 - \omega^2 + j\,\frac{\omega\,\omega_0}{Q}} \tag{8.26}$$

The signal amplitude drops by $-3dB$ at:

$$\omega_{h,l} = \frac{\omega_0}{2\,Q}\left(\pm 1 + \sqrt{1 + 4\,Q^2}\right) \tag{8.27}$$

Presence of noise at the output causes uncertainty in the reading of the frequencies at the crossover of the waveform and the threshold level as illustrated in Figure 8.9. The amount of uncertainty in frequency measurements due to the fluctuations in amplitude of the output signal spectrum is found from:

$$\delta\omega_{B_{h,l}} = \frac{\Delta|I_{out}|}{\left.\frac{dI_{out}}{d\omega}\right|_{\omega_{h,l}}} \tag{8.28}$$

where $\Delta|I_{out}|$ is the fluctuations in the amplitude of the output current.

If the only noise source of the system is assumed to be the Brownian noise of the sensor, the output noise current amplitude is calculated from:

$$\begin{aligned}\tilde{I_B} &= \frac{V_B\left(\frac{\partial C}{\partial y}\right)}{\zeta}\sqrt{4K_BT\zeta\int_0^{+\infty}\frac{\omega^2\,d\omega}{(\omega_0^2-\omega^2)^2+(\frac{\omega\omega_0}{Q})^2}} \\ &= V_B\left(\frac{\partial C}{\partial y}\right)\sqrt{\frac{2\pi K_BT}{M_{eff}}}\end{aligned} \tag{8.29}$$

Assuming that the resonator is driven by a sinusoidal input voltage $v_a\cos\frac{\omega}{2}t$, the output current is given by:

$$I_{out}(j\,\omega) = \frac{v_a^2\,V_B}{4\,\zeta}\left(\frac{\partial C}{\partial y}\right)^2\frac{j\,\frac{\omega\omega_0}{Q}}{\omega_0^2-\omega^2+j\,\frac{\omega\omega_0}{Q}} \tag{8.30}$$

and therefore:

$$\frac{d|I_{out}(j\,\omega)|}{d\omega} = \frac{v_a^2\,V_B}{4\,\zeta}\left(\frac{\partial C}{\partial y}\right)^2\frac{\omega_0\,(\omega^4-\omega_0^4)}{Q\left((\omega_0^2-\omega^2)^2+\left(\frac{\omega\,\omega_0}{Q}\right)^2\right)^{\frac{3}{2}}} \tag{8.31}$$

The uncertainty in reading frequencies ω_l and ω_h due to Brownian noise can now be found using equation 8.28:

$$|\delta\omega_{B_{h,l}}| = \frac{8\,K_{eff}\sqrt{\frac{2\pi K_B T}{M_{eff}}}\left(2Q^2+1-\sqrt{1+4Q^2}\right)^{\frac{3}{2}}}{v_a^2\,Q^2\left(\frac{\partial C}{\partial y}\right)\left(-1+\sqrt{1+4Q^2}-4Q^2+2Q^2\sqrt{1+4Q^2}\right)}$$
$$\approx \frac{8\sqrt{\pi}\,\omega_0}{v_a^2\,Q^2}\left(\frac{\partial C}{\partial y}\right)^{-1}\sqrt{K_B\,T\,K_{eff}} \qquad (8.32)$$

The uncertainty in determining the frequency of the peak value of the transfer function due to Brownian noise will be:

$$|\delta\omega_B| = \frac{|\delta\omega_{B_{h,l}}|}{\sqrt{2}}$$
$$= 4\sqrt{2\pi}\,\frac{\omega_0}{v_a^2\,Q^2}\left(\frac{\partial C}{\partial y}\right)^{-1}\sqrt{K_B\,T\,K_{eff}} \qquad (8.33)$$

The effect of shot noise in crossbars can be included in noise calculations at this step. If a current I_{XB} flows through the crossbars of a sensor with N beam springs, the power spectral density of the force fluctuations on the beam springs is given by $P_n^2 = 2\,q_e\,I_{XB}\,|L_{XB}\times B|^2/N^2$, where it is assumed that the beam springs are stiff in x-direction (i.e., the resonant frequency of the vibration mode in x-direction is at much higher frequencies than the bandwidth of interest). The resulting fluctuations in the resonant frequency of the sensor are given by $\delta\omega_S{}^2 = S_P^{\omega\,2}\,P_n^2\,\Delta\omega$, where $\Delta\omega$ is the measurement bandwidth and S_P^{ω} is the sensitivity of the output frequency of the sensor to the axial force on the beam springs (see section 3.5).

The total frequency fluctuations at the output of the resonator are given by:

$$\delta\omega_n{}^2 = \delta\omega_B{}^2 + \delta\omega_S{}^2 \tag{8.34}$$

This equation holds since the noise sources are assumed uncorrelated. However, it turns out that the phase noise produced by the shot noise of the current in crossbars is much smaller than the one caused by electronics, and therefore, can be ignored. The minimum detectable field is finally given by:

$$\begin{aligned} B_{min} &= \frac{\delta\omega_B}{S_B^\omega} \\ &= \frac{20\sqrt{2\pi}}{3}\sqrt{K_B T}\,\frac{L\,N^{\frac{3}{2}}\,k_b^{\frac{3}{2}}}{v_a^2\,Q^2\,I_{XB}\,L_{XB}}\left(\frac{\partial C}{\partial y}\right)^{-1} \end{aligned} \tag{8.35}$$

For devices a to d, the uncertainties in determining the resonant frequency of the devices due to Brownian noise are $60\mu Hz$, $45\mu Hz$, $24\mu Hz$, and $19\mu Hz$. The minimum detectable magnetic fields for these devices with a $10mA$ current in their crossbars, $2V$ actuation voltages, and Qs of 15000 are $1.250\mu T$, $578nT$, $516nT$, $217nT$. As an example, for a $10Hz$ measurement bandwidth and a $0.1T$ field, the Shot noise in the crossbars causes $\delta f_S = 157nHz$ of variation in the resonant frequency of the most sensitive of the devices (i.e., device d) which is considerably smaller than the amount from the Brownian noise (i.e., $19\mu Hz$).

The noise performance can easily be improved by increasing the Q and the amplitude of the actuation voltage. However, it should be remembered that the above analysis was performed with the assumption of noiseless electronics and the above values are theoretical minima.

8.7 Methods to improve the noise performance

Figure 8.10 illustrates the achievable range for the sensitivity the sensor against other common magnetic sensors. It should be noted that this sensor, unlike many other micromachined sensors, is fabricated in a standard micromachining process with no special materials or processing steps.

Various parameters can be modified to improve the noise performance of the sensor system, and hence, enabling the measurement of smaller fields with better resolution. The noise produced by electronics dominates the noise behavior of the system. As discussed in section 8.2, the amplifiers and components used in the first two stages of the signal processing electronics greatly affect the overall noise performance. The optimization of the noise performance could be achieved best if the electronics could

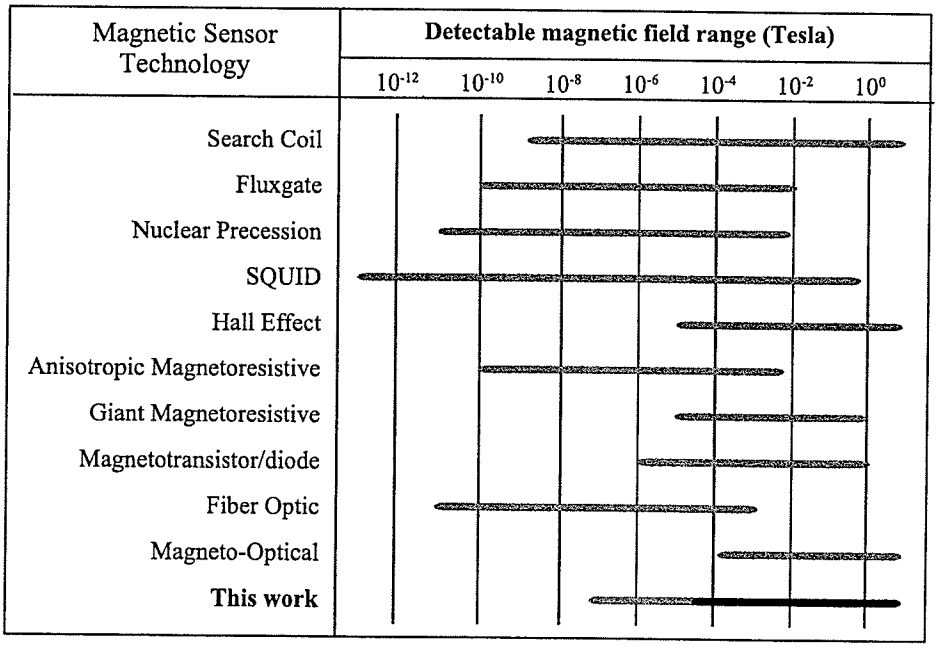

Figure 8.10: *Comparison of sensor performance with other magnetic sensors.*

be integrated on the same chip as the sensor or if they could be put at the closest distance from the sensor. In case of using an integrated circuit for signal processing, various amplifier topologies could be used with better noise performance than the current discrete circuits. Filters with better quality and less noise could also be designed specifically for this application. For a finalized design of the sensor, avoiding the use of switched capacitor filters will certainly improve the signal to noise ratio in the loop. Although not discussed here, the noise of the bias voltage on the output comb, V_B, also contributes to the total noise of the system and should be minimized [219].

The frequency measurement circuitry also plays a crucial role in overall noise performance of the system. The employed FM to PM conversion circuitry uses an XOR gate for phase detection. The dynamic range of the phase detection circuitry can be enhanced by using modified digital phase detectors or analog phase detectors. Analog phase detectors have the extra advantage that they do not produce as much noise on power supply rails as digital phase detectors. The power supply noise affects the stability of the DC voltage at the output of the last lowpass filter. The current analog multiplier which is used to bring down the frequency of the oscillator loop is quite noisy (with an equivalent noise spectral density of a $40M\Omega$ resistor) and can be replaced with a lower noise mixer to improve the signal quality. If it is desired to measure small fields, the sensitivity of the frequency-to-phase conversion can be easily enhanced by increasing the Q of the allpass filters (or by cascading them). The ultimate resolution, however, is determined by the noise behavior of the oscillator loop which is affected by different parameters.

The sensor itself can be modified to improve the noise performance. The most important parameters are the sensitivity and quality factor of the sensor. For a

particular application, the sensor structure and dimensions can be optimized to have the required frequency shift for the range of the magnetic fields that the sensor is going to be used in. The process parameters and technology can also be used as design tools. As an example, a sensor made in MUMPs technology with the same dimensions as device d will have the same resonant frequency but its sensitivity will be $330Hz/T$ instead of $69.6Hz/T$ for device d. Parameters which are easier to modify, especially for fabricated devices, are the drive voltage amplitude and the quality factor of the sensor. Increasing the quality factor reduces the noise inside the oscillator loop, and hence, improves the stability of the signal frequency. The quality factor of the resonator can probably be increased by an order of magnitude by operating the sensor at lower pressures.

Chapter 9

Conclusions

A conclusion is the place where you got tired of thinking.

Harold Fricklestein

Design, modeling, simulation, fabrication, and testing of a novel micromachined magnetic field sensor were discussed in this report. The sensor uses basic electromagnetic laws for detection and measurement of magnetic fields and produces a frequency shift proportional to the magnitude of the present magnetic field at its output. Since the information is embedded in the signal frequency, the output signal is robust against interference from other sources during transmission. The design of the sensor allows for its fabrication in many standard MEMS processes. For that matter, any process flow can be used to fabricate the sensor as long as the electrostatic resonator could be fabricated, and preferably, a metal layer exists to reduce the resistance of crossbars.

9.1 What has been done

The sensor design and the basics of its operation are explained in Chapter 2. The centerpiece of the device structure is an electrostatic resonator which is connected to two current-carrying beams by 2 or 4 beam springs. The principle behind the design and how a magnetic field causes exertion of an axial force on the beam springs were explained and a simple setup for operating the sensor was illustrated in this chapter.

The operation of the sensor was modeled in Chapter 3. The electrostatic drive and signal detection were discussed first. The mechanical behavior of the sensor was modeled next and a model for the behavior of beam springs under axial stress was derived. Dynamics of the mechanical structure were also modeled. Dunkerley's method was used to estimate the resonant frequency of the structure. The effect of the raise in temperature due to passing of the current through the crossbars was investigated and partially modeled. Combining all of the above resulted in deriving a relatively simple model for the sensitivity of the sensor to axial forces on beam springs, and consequently, to surrounding magnetic fields. Modeling of the damping in the system was also discussed. Validity of the developed model was verified through finite element simulations and eventually by experimental results. The derived model can be used for optimization of future sensor designs.

Chapter 4 was dedicated to the simulation of the sensor behavior. Each of the involved physical domains was investigated through performing finite element simulations. When it was required, the simulations were done in multiphysics domain (e.g., to investigate the electro-thermo-mechanical effects). The simulations were mainly used to verify the modeling results. In case of electro-thermo-mechanical effects, sim-

ulations allowed for investigation of phenomena which could not be included in the analytic model.

Fabrication techniques were briefly discussed in Chapter 5. Three different process flows were examined for fabrication of the sensors. The pros and cons of each of the process flows for fabrication of the sensor were also pointed out.

Dedicated signal processing electronics were designed and analyzed in detail in Chapter 7. The possible methods for electrostatic actuation and sensing were introduced first. The main challenge in processing the output of the sensor was to remove the interfering signals which were orders of magnitude larger than the desired signal. This was achieved by proper use of tunable active filters. To alleviate the need for precision measurement equipment, it was decided to use the sensor in a self oscillating loop and to employ dedicated electronics for frequency shift measurements. Additional signal processing was required to rid of the beating effects inside the oscillator loop. A novel technique was used to measure the frequency shifts. In this method, the main processing of the signal is performed at a predetermined frequency. A delay circuitry designed to work at a fixed frequency to cause a frequency sensitive phase shift on the down-converted signal. The phases of the signal and its delayed version are compared, and finally, a DC voltage is produced at the output as a measure of the frequency shift. Active allpass filters were used for delay elements which allowed for simple manipulation of their frequency response and sensitivity.

The experiments and conditions under which the sensors were tested were described in detail in Chapter 6. The difference between operation in air and vacuum were illustrated and the final test setup was discussed. Thermal effects posed a challenge in taking measurements of the magnetic fields with different currents in

crossbars. This issue was circumvented by taking differential measurements. The sensitivity of the sensors was measured to range from 46 to $88Hz/T$ using the setup described earlier.

The noise behavior of the resonator was discussed in Chapter 8. The nonlinear blocks used in the oscillator loop did not allow for frequency domain analysis and the noise analysis was performed on the open loop system. An idealized situation where the only sources of noise were the Brownian noise from the impingement of gas molecules and the Shot noise in crossbars was analyzed to find the theoretical minimum detectable signal with the sensor. Long term time-domain measurements were employed to experimentally analyze and quantify the noise behavior of the oscillator loop.

The sensor can sense a wide range of magnetic fields. The linear response of the sensor makes it ideal for applications where large fields are to be measured. There is a trade off between the dynamic range and sensitivity of the measurements. Both of these parameters can be individually or simultaneously improved by changing the quality factor, the order of the allpass filters, or the number of cascaded filters.

9.2 Future work

Future work on this sensor can focus on optimization of the sensor design for particular applications. Design optimization procedure would comprise of choosing an appropriate fabrication process flow and selecting proper dimensions for the sensor based on the developed model. The following equations for the resonant frequency,

sensitivity, and the minimum detectable field can be used for the initial steps of designs for future sensors:

$$f_0 = \frac{1}{2\pi}\sqrt{\frac{N k_b}{M_s + \frac{2N^2}{5} M_b}} \tag{9.1}$$

$$S_B^{f_0} = \frac{3\, I_{XB}\, L_{XB}\, f_0}{5\, N\, L\, k_b} \tag{9.2}$$

$$B_{min} = \frac{20\sqrt{2\pi}}{3}\sqrt{K_B T}\,\frac{L\, N^{\frac{3}{2}}\, k_b^{\frac{3}{2}}}{v_a^2\, Q^2\, I_{XB}\, L_{XB}}\left(\frac{\partial C}{\partial y}\right)^{-1} \tag{9.3}$$

The electronic circuitry can be improved for operation with lower noise. For example, the input signal amplifiers can be modified for optimum noise performance. If the electronics are to be designed for a single sensor, switched capacitor filters may be replaced with continuous time filters to remove the switching noise of the filters. The frequency shift measurement circuitry can benefit from using a mixer with lower noise and phase detectors with better performance. Moreover, noise performance, sensitivity, and dynamic range of measurements can be enhanced by employing negative feedback and measuring the shifts in frequency with a closed loop system. In such a system, the output DC voltage of the circuitry is monitored and the frequency of the signal used to down-convert the sensor signal is adjusted to yield a constant voltage at the output of the system. The closed-loop system design could be similar to that of phase-locked-loops.

Techniques from digital and nonlinear control theory may be employed to analyze the noise of the oscillator loop in more detail if required. However, this does not seem to be of imminent importance and characterization of the stability of the oscillator frequency seems to provide enough information.

Performance of the sensory system as a whole can be significantly improved if the electronics are designed on a chip. Three possible methods can be pursued to design the electronics: the electronic circuitry can be designed and fabricated in the same process that is used for fabrication of MEMS, the electronic and MEMS chips could be fabricated in separate processes and packaged in the same module, or the layers available in a standard microelectronic process can be used for fabrication of MEMS. In either case, proximity of the sensor and electronics greatly reduces the amount of unwanted signal interference and beating (with proper layout of the system components). This, in turn, would allow the required signal processing to be done with a simpler circuitry. Designing a dedicated chip for electronics would also lower the power consumption of the sensory system. Instead of switched capacitor filters, g_m−C filters could be used which also provide the possibility of tuning the frequency response.

Different aspects of the work in this report can be used for design of other devices and systems. Results of the modeling section can be adapted and adjusted to investigate the behavior of many of the micromechanical devices. The developed electronics can be used to process the output signal of many different electrostatic or thermal devices. A similar setup for frequency shift measurement circuitry can be employed for various other applications (e.g., Doppler radar systems).

Appendix A

Microsensor Fabrication Process

The sensors were fabricated at the NanoFab at the University of Alberta. Details of the process steps are specified below. A recipe for lithography with $2\mu m$ feature/gap size was developed for the fist time in NanoFab and successfully used to transfer the mask pattern to the substrate. As will be explained, the process needs a single mask only. Due to the small feature sizes, the mask had to be made through facilities outside the university by ADTEK photomask [220]. Parameters of the SOI wafers used in this process are specified in Table A.1.

The processing steps are explained below.

Table A.1: *SOI wafer parameters.*

Device layer thickness	$5\mu m$
Buried oxide thickness	$2.5\mu m$
Handle wafer thickness	$500\mu m$
Wafer diameter	$100mm$, *both sides polished*
Resistivity of the device layer	5 *to* 15 $\Omega - cm$
Device layer dopant	*Boron*
SOI wafer fabrication technique	*Bonding*

1. Initial cleaning of the wafers

This is done to rid of any metallic and organic residue on the surface of the wafers. The wafers are put in a 3 : 1 mixture of sulfuric acid and hydrogen peroxide ($750cc$ of H_2SO_4 and $250cc$ of H_2O_2) for 15 minutes.

2. Rinse and dry

The wafers are rinsed by deionized (DI) water and dried by a nitrogen flow over the surface of the wafers in a double stack spin drier system.

3. HMDS coating

To promote the adhesion between the silicon surface and the photoresist, the silicon syrface is coated with a layer of hexamethyldisilazane (HMDS). The wafers are put in the HMDS oven at a temperature of $150°C$ for 20 minutes. The wafers are removed from the oven and left to gradually cool down for 10 minutes.

4. Photoresist spinning

A $1.2\mu m$ layer of photoresist (HPR504) is spun on the wafer. This was done in two steps using a resist spinner at an angular speed of $500rpm$ for 10 seconds and then ramping the speed up and spinning the wafer at $4000rpm$ for 40 seconds.

5. Soft bake

To remove any remaining solvent in the photoresist, the coated wafers were put on a vacuum hot plate for 90 seconds at $115°C$.

6. Rehydration

Wafers are left for 30 to 60 minutes in the cleanroom environment with a hu-

midity of about 40% to absorb enough water for successful lithography at the next step.

7. Lithography

The photoresist on wafers was exposed to ultraviolet light (through the mask) to transfer the mask pattern to the photoresist layer. Due to the small feature sizes, it was necessary to leave the mask and wafer in contact for at least 2 minutes under vacuum before the exposure to avoid any stress induced patterns on the photoresist. The photoresist was then exposed to the UV light for 2.5 seconds.

8. Photoresist developing

The exposed photoresist was developed in a 50% diluted positive resist developer (Shippley 354) for 100 seconds. The dilution of the developer was a necessary step, as the original develeoper removed the photoresist so quickly that the smallest features on the wafer could not survive the process.

9. Rinse and dry

The wafer with patterned photoresist was rinsed in DI water for one minute and blow dried by filtered deionized nitrogen.

10. Etching of the device layer

The wafer was then transfered to a deep reactive ion etching system (DRIE). The etching is based on Bosch process; i.e., subsequent etch and deposition cycles. The recipe that was used to etch the wafers composed of 9 seconds of etching followed by 9 seconds of deposition. Process parameters are summarized in Table A.2. The etch rate for the silicon layer was found to roughly be about

Table A.2: *DRIE parameters.*

Parameter	C_4F_8 Flow	SF_6 Flow	Forward power	ICP power	Pressure
Etch	$1sccm$	$150sccm$	$40W$	$750W$	$30mTorr$
Deposition	$200sccm$	$1sccm$	$12W$	$750W$	$30mTorr$

$0.5\mu m/cycle$. However, since the etch rate was not uniform across the wafer (the edges etched faster than the center), 30% to 40% of over-etching was necessary.

11. Photoresist removal

The photoresist on wafer polymerized during the DRIE step and could not be removed by acetone or other solvents. Therefore, a second piranha cleaning was performed to remove any photoresist residue.

12. Dicing

The wafers were diced after the photoresist removal. The small size of the chamber of the critical-point drying system mandated this step. The dicing was done before etching of the buried oxide layer to avoid damaging of the delicate devices.

13. Buried Oxide etch

The exposed oxide layer was etched in a 10:1 diluted buffered hydrofluoric acid (BHF). With an etch rate of $\approx 55nm/min$, the required time to release the moving parts of the micromachined structures was about 20 minutes. The wafers were then rinsed in DI water and transferred to a container and immersed in isopropyl alcohol (IPA).

14. Critical point drying of the wafers

Unless done properly, the final drying step of microstructures can result in stiction of the devices to the substrate. One of the techniques with a very high yield is critical-point drying. The process that was used for critical-point drying of the microstructures consisted of the following steps:

1. The system chamber was filled with IPA and the chips were transferred to the chamber.
2. The chamber was sealed and cooled down to $0°C$.
3. Liquid CO_2 was pumped into the chamber to replace IPA.
4. The temperature was slowly increased until the pressure inside the chamber reached $1072psi$. The liquid CO_2 becomes gaseous under this circumstances.
5. The pressure is kept at $1350psi$ at a temperature of $31°C$ for 4 minutes.
6. The gaseous CO_2 is pumped out of the chamber.

Appendix B

Simulation Code

B.1 FEM simulation code

Finite element simulations were performed using ANSYS version 8.1 [158].

B.1.1 Electrostatic simulation code

Below is the simulation code for electrostatic simulation on the comb the structure and then calculate the capacitance using the CMATRIX macro.

```
/batch,list
/title, Electrostatic actuation analysis
/com, Electrostatics: SOLID122 brick elements
/com, uMKSV units

!************************
!PARAMETERS
!************************
feng=15 ! finger engagement, um
fl=35                    ! finger length, um
fw=3                     ! finger width, um
```

```
fg=2.5 ! finger gap, um
gs=10                          ! substrate gap, um
thk=10 ! silicon thickness, um
nf=15 ! number of fingers
shl=(2*nf-1)*fw+(nf-1)*2*fg ! shuttle length, um
shw=25 ! shuttle width, um
scl=(2*nf+1)*fw+nf*2*fg ! stationary comb length, um
scw=25 ! stationary comb width, um
gpext=20 ! ground plane extension, um
AirExt=25 ! air extension volume around the device, um

VSh=1 ! voltage on the shuttle, V
VSc=0 ! voltage on the stationary comb, V

!************************
!MODEL
!************************
/prep7

et,1,122                    ! 20-node bricks; Electrostaticsl

emunit,EPZRO,8.854e-6    ! pF/um

!SILICON

mp,ex,1,169e3             ! kg/(um)(s)^2
mp,nuxy,1,0.22
mp,dens,1,2.33e-15        ! kg/(um)^3
mp,kxx,1,150e6 ! pW/um K
mp,rsvx,1,0.112e-6 ! ohm-um
mp,alpx,1,2.9e-6 ! um/um

!GOLD

mp,ex,2,75e3              ! kg/(um)(s)^2
mp,nuxy,2,0.42
mp,dens,2,19.3e-15        ! kg/(um)^3
mp,kxx,2,315e6 ! pW/um K
mp,rsvx,2,92.3e-15 ! ohm-um
mp,alpx,2,14.2e-6 ! um/um

!AIR
```

```
mp,perx,3,1
mp,murx,3,1

!************************
!STRUCTURE
!************************
rectng,-scl/2,scl/2,0,-scw
rectng,-scl/2,-scl/2+fw,0,fl
agen,nf+1,2,,,2*fg+2*fw
aadd,all
numcmp,area

rectng,-shl/2,shl/2,2*fl-feng,2*fl-feng+shw
rectng,-shl/2,-shl/2+fw,fl-feng,2*fl-feng
agen,nf,3,,,2*fg+2*fw
asel,s,area,,1
asel,inve
aadd,all
numcmp,area

asel,all
/pnum,area,1
/number,1
aplot

vext,all,,,,,-thk

/pnum,area,0
/pnum,volu,1
/number,1
vplot

block,-scl/2-AirExt,scl/2+AirExt,-scw-AirExt,2*fl-feng+shw+AirExt
     ,-thk-AirExt,AirExt

vsbv,3,1,,delete,keep
vsbv,4,2,,delete,keep

block,-scl/2-gpext,scl/2+gpext,-gpext,2*fl+gpext,-thk-gs,-thk-gs-5
vsbv,3,4,,delete,keep
numcmp,volu
```

```
!v1: stationary comb v2: moving comb
!v3: ground plane v4: air

allsel,all

!************************
!MESHING
!************************
vsel,s,volu,,4
vatt,3
smrt,5
mshape,1,3D
mshkey,0
vmesh,all

!************************
!LOADS
!************************
vsel,s,volu,,1
aslv,r
nsla,r,1
cm,cond1,node ! fixed electrode
d,all,volt,VSc
allsel,all

vsel,s,volu,,2
aslv,r
nsla,r,1
cm,cond2,node ! moving electrode
d,all,volt,VSh
allsel,all

vsel,s,volu,,3
aslv,r
nsla,r,1
cm,cond3,node ! ground plane
d,all,volt,VSc
allsel,all

finish

!************************
```

```
!SOLUTION
!************************
/solu
solve

cmatrix,1,'cond',3,0,'C_comb'
finish
```

B.1.2 Statics simulation code

Static and modal simulations on device *a* were performed using the following code.

```
/batch,list
/title, Magnetic Sensor
/com, uMKSV units
/com,  Structural

!************************
!PARAMETERS
!************************
fl=35                    ! finger length, um
fw=3                     ! finger width, um
fg=3 ! finger gap, um
feng=15 ! finger engagement, um
nf=15 ! number of fingers
gs=2                     ! substrate gap, um
thk=10 ! silicon thickness, um
shl=(2*nf-1)*fw+(nf-1)*2*fg ! shuttle length, um
shw=50 ! shuttle width, um
bl=150 ! spring beam length, um
bw=3    ! spring beam width, um
bg=35    ! spring beam gap, um
sl=13 ! support length, um
sw=50 ! support width, um
sbl=520 ! crossbar length, um
sbw=9 ! crossbar width, um

NumMod=1 ! number of modes to extract

Vin=100 ! voltage between the combs, volts
```

```
ESForce=1.45e-3/2*Vin*Vin ! total electrostatic force, uN
ESPres=ESForce/nf/fw/thk ! electrostatic pressure on fingers, MPa

Iin=10e9 ! current in crossbars, pA
Bin=1e-12 ! present magnetic field strength, TT
MSPres=Iin*Bin/thk ! magnetostatic pressure, MPa

!************************
!MODEL
!************************
/prep7
et,1,186                ! 20-node bricks; Solid

emunit,EPZRO,8.854e-12   ! pF/um
mp,ex,1,169e3            ! kg/(um)(s)^2
mp,nuxy,1,0.22
mp,dens,1,2330e-18  ! kg/(um)^3

!************************
!STRUCTURE
!************************
rect,-shl/2,shl/2,-shw/2,shw/2 !a1
rect,-shl/2,-shl/2+fw,shw/2,shw/2+fl !a2
rect,-shl/2,-shl/2+fw,-shw/2,-shw/2-fl !a3
rect,-shl/2-bl,-shl/2,bg/2,bg/2+bw !a4
rect,-shl/2-bl,-shl/2,-bg/2,-bg/2-bw !a5
rect,shl/2+bl,shl/2,bg/2,bg/2+bw !a6
rect,shl/2+bl,shl/2,-bg/2,-bg/2-bw !a7
rect,-shl/2-bl,-shl/2-bl-sl,sw/2,-sw/2 !a8
rect,shl/2+bl,shl/2+bl+sl,sw/2,-sw/2 !a9

agen,nf,2,,,2*fg+2*fw
agen,nf,3,,,2*fg+2*fw ! fingers done

rect,shl/2+bl+sl,shl/2+bl+sl+sbw,-sbl/2,sbl/2 !a9
rect,-shl/2-bl-sl,-shl/2-bl-sl-sbw,-sbl/2,sbl/2 !a10

asel,all
aadd,all ! a50
numcmp,all

vext,1,,,,,-thk ! v1
```

```
!************************
!LOADS
!************************
asel,s,loc,y,sbl/2,sbl/2
asel,a,loc,y,-sbl/2,-sbl/2
da,all,all,0

asel,s,loc,x,-shl/2-bl-sl-sbw,-shl/2-bl-sl-sbw
asel,a,loc,x,shl/2+bl+sl+sbw,shl/2+bl+sl+sbw
sfa,all,1,pres,MSPres

asel,s,loc,y,-fl-shw/2,-fl-shw/2
sfa,all,1,pres,ESPres

allsel

!************************
!MESHING
!************************
vsel,s,volu,,1
vatt,1,,1,0
smrt,5
mshape,1,3D
mshkey,0
vmesh,all
allsel,all
finish

!************************
!ANALYSIS
!************************
/solu
antype,0
lnsrch,on
solve
finish

!************************
!POSTPROCESSING
!************************
/post1
```

```
/efacet,1
avprin,0,
plnsol,u,y,0,1.0
finish

!************************
!ANALYSIS
!************************
/solu
antyp,2
msave,0
modopt,lanb,NumMod,100
eqslv,spar
mxpand,NumMod,,,0
lumpm,0
pstres,on !off
solve
finish

/post1
set,list
finish
```

B.1.3 Electrothermal simulation code

Simulations of the electro-thermo-mechanical effects on device d were performed with the following code.

```
/batch,list
/title, Electrothermal analysis
/com, Structure: SOLID98 brick elements
/com, uMKSV units

!************************
!PARAMETERS
!************************
fl=35                    ! finger length, um
fw=3                     ! finger width, um
fg=2.5 ! finger gap, um
```

```
feng=15 ! finger engagement, um
nf=15 ! number of fingers
gs=10                        ! substrate gap, um
thk=10 ! silicon thickness, um
shl=(2*nf-1)*fw+(nf-1)*2*fg ! shuttle length, um
shw=15 ! shuttle width, um
shcw=33 ! shuttle connector length, um
shcl=10 ! shuttle connector length, um
bl=200 ! spring beam length, um
bw=3    ! spring beam width, um
sl=3 ! support length, um
sw=20 ! support width, um
sbl=520 ! crossbar length, um
sbw=9 ! crossbar width, um

mw=5                        ! metal line width, um
mt=0.08                    ! metal line thickness, um

Ves=100 ! voltage between the combs, volts
ESForce=1.45e-3/2*Ves*Ves ! total electrostatic force, uN
ESPres=ESForce/nf/fw/thk
        ! electrostatic pressure at the ends of the fingers, MPa

Tenv=300 ! environment temperature, C
Vin=0.24 ! input voltage, V

!************************
!MODEL
!************************
/prep7

et,1,98             ! 10-node bricks; Coupled field

emunit,EPZRO,8.854e-6   ! pF/um

!SILICON
mp,ex,1,171.031998e3,-38.748788          ! kg/(um)(s)^2
mp,nuxy,1,0.22
mp,dens,1,2.33e-15      ! kg/(um)^3
mp,kxx,1,150e6 ! pW/um K
mp,rsvx,1,0.112e-6 ! ohm-um
mp,alpx,1,2.9e-6 ! um/um
```

```
!GOLD
mp,ex,2,75e3            ! kg/(um)(s)^2
mp,nuxy,2,0.42
mp,dens,2,19.3e-15      ! kg/(um)^3
mp,kxx,2,315e6 ! pW/um K
mp,rsvx,2,92.3e-15 ! ohm-um
mp,alpx,2,14.2e-6 ! um/um

!************************
!STRUCTURE
!************************
rect,-shl/2,shl/2,shcw/2,shcw/2+shw !a1
rect,-shl/2,-shl/2+fw,shcw/2+shw,shcw/2+shw+fl !a2
rect,-shl/2,shl/2,-shcw/2,-shcw/2-shw !a3
rect,-shl/2,-shl/2+fw,-shcw/2-shw,-shcw/2-shw-fl !a4
rect,-shcl/2,shcl/2,-shcw/2,shcw/2 !a5
rect,-bl-shcl/2,bl+shcl/2,-bw/2,bw/2 !a6
rect,-shcl/2-bl,-shcl/2-bl-sl,-sw/2,sw/2 !a7
rect,shcl/2+bl,shcl/2+bl+sl,-sw/2,sw/2 !a8
rect,shcl/2+bl+sl,shcl/2+bl+sl+sbw,-sbl/2,sbl/2 !a9
rect,-shcl/2-bl-sl,-shcl/2-bl-sl-sbw,-sbl/2,sbl/2 !a10

agen,nf,2,,,2*fg+2*fw
agen,nf,4,,,2*fg+2*fw ! fingers done

asel,all
aadd,all ! a49
numcmp,all

vext,1,,,,,-thk ! v1

block,shcl/2+bl+sl+sbw/2-mw/2,shcl/2+bl+sl+sbw/2+mw/2,-sbl/2,sbl/2
     ,0,mt !v2
block,-shcl/2-bl-sl-sbw/2-mw/2,-shcl/2-bl-sl-sbw/2+mw/2,-sbl/2,sbl/2
     ,0,mt !v3

vglue,1,2,3
numcmp,volu

!************************
!MESHING
```

```
!************************
vsel,s,volu,,3
vatt,1,,1,0
smrt,5
mshape,1,3D
mshkey,0
vmesh,all

vsel,s,volu,,1
vsel,a,volu,,2
vatt,2,,1,0
smrt,4
mshape,1,3D
mshkey,0
vmesh,all

allsel,all
finish

!************************
!LOADS
!************************
/solu
asel,s,loc,y,-sbl/2
asel,a,loc,y,sbl/2
da,all,ux,0
da,all,uy,0
da,all,uz,0
da,all,temp,Tenv

asel,s,loc,y,-sbl/2
da,all,volt,0

asel,s,loc,y,sbl/2
da,all,volt,Vin

asel,s,loc,y,shcw/2+shw+fl
sfa,all,1,pres,ESPres

allsel

!************************
```

```
!ANALYSIS
!************************
antype,0
lnsrch,on
solve
finish

!************************
!POSTPROCESSING
!************************
/post1
plnsol,temp,,0
```

B.1.4 Thermal stress simulation code

Simulations to investigate the effects of thermal stress in crossbars for device d were performed using the simulation code below.

```
/batch,list
/title, Magnetic Sensor
/com, uMKSV units
/com,  Structural

!************************
!PARAMETERS
!************************
fl=35                    ! finger length, um
fw=3                     ! finger width, um
fg=2.5 ! finger gap, um
feng=15 ! finger engagement, um
nf=15 ! number of fingers
gs=10                     ! substrate gap, um
thk=10 ! silicon thickness, um
shl=(2*nf-1)*fw+(nf-1)*2*fg ! shuttle length, um
shw=15 ! shuttle width, um
shcw=33 ! shuttle connector length, um
shcl=10 ! shuttle connector length, um
bl=200 ! spring beam length, um
bw=3    ! spring beam width, um
```

```
sl=3 ! support length, um
sw=20 ! support width, um
sbl=520 ! crossbar length, um
sbw=9 ! crossbar width, um

NumMod=1 ! number of modes to extract

Vin=100 ! voltage between the combs, volts
ESForce=1.45e-3/2*Vin*Vin ! total electrostatic force, uN
ESPres=ESForce/nf/fw/thk
          ! electrostatic pressure at the ends of the fingers, MPa

IC=1e-3
Iin=IC*1e12 ! current in crossbars, pA
Bin=1e-12 ! present magnetic field strength, TT
MSPres=Iin*Bin/thk ! magnetostatic pressure, MPa

Tc=IC*IC*120*520e-6/150/8/90e-12
E_T=169e3*(1-9.4e-5*Tc)
ThStress=1.117e-24*E_T*Iin*Iin
         ! thermally induced stress in crossbars, MPa
ThDisp=ThStress*sbl/E_T
         ! change in the length as a result of thermal stress, um

!************************
!MODEL
!************************
/prep7
et,1,186 ! 20-node bricks; Solid

emunit,EPZRO,8.854e-6 ! pF/um
mp,ex,1,E_T             ! kg/(um)(s)^2, thermal changes included
mp,nuxy,1,0.22
mp,dens,1,2330e-18  ! kg/(um)^3

!************************
!STRUCTURE
!************************
rect,-shl/2,shl/2,shcw/2,shcw/2+shw !a1
rect,-shl/2,-shl/2+fw,shcw/2+shw,shcw/2+shw+fl !a2
rect,-shl/2,shl/2,-shcw/2,-shcw/2-shw !a3
rect,-shl/2,-shl/2+fw,-shcw/2-shw,-shcw/2-shw-fl !a4
```

```
rect,-shcl/2,shcl/2,-shcw/2,shcw/2 !a5
rect,-bl-shcl/2,bl+shcl/2,-bw/2,bw/2 !a6
rect,-shcl/2-bl,-shcl/2-bl-sl,-sw/2,sw/2 !a7
rect,shcl/2+bl,shcl/2+bl+sl,-sw/2,sw/2 !a8
rect,shcl/2+bl+sl,shcl/2+bl+sl+sbw,-sbl/2,sbl/2 !a9
rect,-shcl/2-bl-sl,-shcl/2-bl-sl-sbw,-sbl/2,sbl/2 !a10

agen,nf,2,,,2*fg+2*fw
agen,nf,4,,,2*fg+2*fw ! fingers done

asel,all
aadd,all ! a49
numcmp,all

vext,1,,,,,-thk ! v1

!************************
!LOADS
!************************
asel,s,loc,y,sbl/2,sbl/2
da,all,all,0

asel,s,loc,y,-sbl/2,-sbl/2
da,all,uy,ThDisp
da,all,ux,0
da,all,uz,0

allsel

!************************
!MESHING
!************************
vsel,s,volu,,1
vatt,1,,1,0
smrt,5
mshape,1,3D
mshkey,0
vmesh,all
allsel,all
finish

!************************
```

```
!ANALYSIS
!************************
/solu
antype,0
lnsrch,on
solve
finish

!************************
!POSTPROCESSING
!************************
!/post1
!/efacet,1
!avprin,0,
!plnsol,u,y,0,1.0
!finish

!************************
!ANALYSIS
!************************
/solu
antyp,2
msave,0
modopt,lanb,NumMod,100
eqslv,spar
!mxpand,NumMod,,,0
lumpm,0
pstres,on !off
solve
finish

/post1
set,list
finish
```

B.2 Analytic modeling code

The code for calculating various parameters from the derived analytic models given below. Maple version 10 from Waterloo Maple Inc. was used to carry some of the

analytic calculations [221].

```
restart;
with(Units):

#Physical constants
eta:=1.78e-5: #*Unit(kg/m/s):          #Viscosity of air at atm
lambda_0:=70e-9: #*Unit(m):            #Mean free path at atm
epsilon_0:=8.854e-12: #*Unit(F/m):     #Dielectric constant of vacuum
K_B:=1.3806e-23: #*Unit(J/K):          #Boltzmann constant

#Material Properties
rho_e:=0.112:     #*Unit(ohm*m):       #Resistivity of Si
rho_m:=2330:      #*Unit(kg/m^3):      #Density of Si
E0:=144.063e9:    #*Unit(Pa):          #Young's modulus of Si @ 300K
ET:=T-> E0*(1-9.4e-5*T): #*Unit(Pa):   #Young's modulus of Si @ TK
nu0:=0.2075:                           #Poisson's ratio of Si
alpha:=2.9e-6:                         #Thermal expansion coefficient of Si
kappa:=148: #*Unit(W/K/m):             #Thermal conductivity of Si

rho_e_au:=92.3e-9: #*Unit(ohm*m):      #Resistivity of Au
rho_m_au:=19300: #*Unit(kg/m^3):       #Density of Au
E0_au:=79e9: #*Unit(Pa):               #Young's modulus of Au
nu0_au:=0.42:                          #Poisson's ratio of Au
alpha_au:=14.2e-6:                     #Thermal expansion coefficient of Au
kappa_au:=310: #*Unit(W/K/m):          #Thermal conductivity of Au

#Environmental properties
T0:=300:      #*Unit(K):               #Temperature
P0:=103e3:    #*Unit(Pa):              #Pressure
B0:=0.4:      #*Unit(T):               #Present magnetic field

#Input Parameters
va:=1:      VA:=0:          #Actuation port
VB:=30:     vb:=0:          #Detection port
VG:=0:      vg:=0:          #Ground port
IC:=10e-3:                 #Crossbar current
BandWidth:=2*Pi*100:       #Measurement bandwidth


#Device Data
NF:=15:                            #Number of fingers
```

```
UC:=0.25e-6:  #*Unit(m):        #Undercut at the corners
Gf:=2.5e-6+UC:   #*Unit(m):     #Gap between fingers
Lf:=35e-6-UC:     #*Unit(m):    #Finger length
Wf:=3e-6-UC:       #*Unit(m):   #Finger width
Wb:=3e-6:       #*Unit(m):      #Spring width
Thk:=10e-6:  #*Unit(m):         #Layer thickness
Lb:=200e-6+2*UC:   #*Unit(m):   #Spring length
NB:=2:                          #Total number of springs
Ash:=NB-> if NB=2               #Area of the shuttle
then (15*157*2+10*33)*1e-12:    #*Unit(m)^2
else (50*157)*1e-12 end if:
LC:=520e-6+2*UC: #*Unit(m):    #Crossbar length
Wsb:=9e-6-2*UC: #*Unit(m):      #Crossbar width
Wau:=5e-6: #*Unit(m):           #Gold layer width
Tau:=80e-9: #*Unit(m):          #Gold layer thickness
AirGap:=10e-6: #*Unit(m):       #Air gap underneath the structure
RC:=120:  #*Unit(Ohm):         #Crossbar resistance


#Mechanical analsys
Msh:=(2*NF*Lf*Wf+Ash(NB))*Thk*rho_m:        #Mass of the shuttle
Mb:=Lb*Wb*Thk*rho_m:                        #Mass of the beam springs
Meff:=Msh/NB+2*NB/5*Mb:
Tc:=T0+(IC^2*RC*LC)/(8*Wsb*Thk*kappa):
Ib:=Thk/48*(Wb+Wb-2*UC)*(Wb^2+(Wb-2*UC)^2): #Spring's moment of inertia

k0:=12*ET(T0)*Ib/Lb^3;
k0T:=k0*ET(Tc)/E0;
f0:=evalf(1/2/Pi*sqrt(k0/Meff));
f0T:=evalf(f0*sqrt(ET(Tc)/E0));
SFB0:=evalf((3*IC*LC)/(2*Pi*5*NB*Lb*sqrt(k0*Meff)));
SFBT:=evalf((3*IC*LC)/(2*Pi*5*NB*Lb*sqrt(k0T*Meff)));

w0:=2*Pi*f0T:
Q:=15000:
dCdy:=1.4e-9:

#Noise analysis
I_out:=w-> va^2*VB/4/zeta*dCdy^2*I*w*w0/Q/(I*w*w0/Q+w^2-w0^2):
Imag:=w-> va^2*VB/4/zeta*dCdy^2*w*w0/Q/sqrt((w*w0/Q)^2+(w^2-w0^2)^2):
dImag:=simplify(diff(Imag(w),w)):
#w_1:=solve(Imag(w)=sqrt(1/2)*va^2*VB/4/zeta*dCdy^2,w):
```

```
w_h:=1/2*sqrt(2)*sqrt(1+2*Q^2+sqrt(1+4*Q^2))*w0/Q:
dIdw_h:=simplify(eval(dImag,w=w_h),assume=positive):

X:=w^2/((w*w0/Q)^2+(w^2-w0^2)^2):
I_noise:=
simplify(VB*dCdy*sqrt(4*K_B*T0*w0/2/Pi/Q/Meff*int(X,w=0..infinity))):

Delta_omega:=
simplify(eval(I_noise/dIdw_h,zeta=Meff*w0/Q),assume=positive);

Delta_f:=evalf(Delta_omega/2/Pi);

Delta_f_n:=evalf(sqrt(2)*Delta_f);

Delta_B_n:=Delta_f_n/SFBT;

#Thermal analysis
R0:=rho_e_au*SBL/AuW/AuT;
qdot:=IC^2*R0/SBL/SBW/Thk/kappa;
ThermalEqn:=Diff(T(x),x,x)+qdot=0;
dsolve({ThermalEqn, T(0)=T0, T(SBL)=T0},T(x));
assign(%);
TSh:=eval(T(x),x=SBL/2);
E:=E_T(TSh):
```

B.3 Allan variance calculations

The code for calculating the Allan variance of the measured frequencies in Matlab R14 is given below [222].

```
clear all;

FData=load('FMeasure_Sensor_2Sec');  %Load measurement results from a file

M=length(FData)
y=FData./mean(FData);
tau0=2;
nmax=floor(log(M/3)/log(2));
taumax=nmax*tau0;
```

```
p=3;
q=floor((2^(1/p)).^[0:p*nmax]);

adev(1)=allan(y,1);
for i=2:length(q)
    n=q(i);
    yt=zeros(1,M-n+1);
    fprintf('.');
    for j=1:M-n+1
        yt(j)=mean(y(j:j+n-1));
    end;
    adev(i)=allan(yt,n);
end;
fprintf('\n');

tau=tau0*q;
avar=adev.^2;

figure(1)
hold on;
loglog(tau,avar,'k-','LineWidth',2);
xlabel('Averaging time, \tau (sec)');
ylabel('Allen variance, \sigma_y^2 (\tau)');
grid;

%%%%%%%%%%%%%%%%%%%%%%%%

function sigmay=allan(y,n)
M=length(y);
s2=0;
for k=1:(M-2*n+1)
    s2=s2+(y(k+n)-y(k))^2;
end;
sigmay=sqrt(s2/(2*(M-2*n+1)));
```

Appendix C

Signal processing circuits

Details of the circuits used for processing of the sensor signal are discussed in this appendix. The most important of the signal processing blocks are filters which are realized in different ways to accommodate the system requirements. Filter design is a mature field with many references on theoretical and practical issues [167, 169]. The complete signal processing electronics is schematically shown in Figure C.1. Operation of the mixer, comparators, and the phase detector are fairly simple and is not covered here.

The circuit behavior of the blocks in Figure C.1 are summarized in Table C.1. The part number of active element used for realization of each block is also provided.

C.1 Amplifiers

Block A_1 (Figure C.1) is a transresistance amplifier to convert the output current of the shuttle into a voltage with a gain of $1M\Omega$. Further amplification of the signal

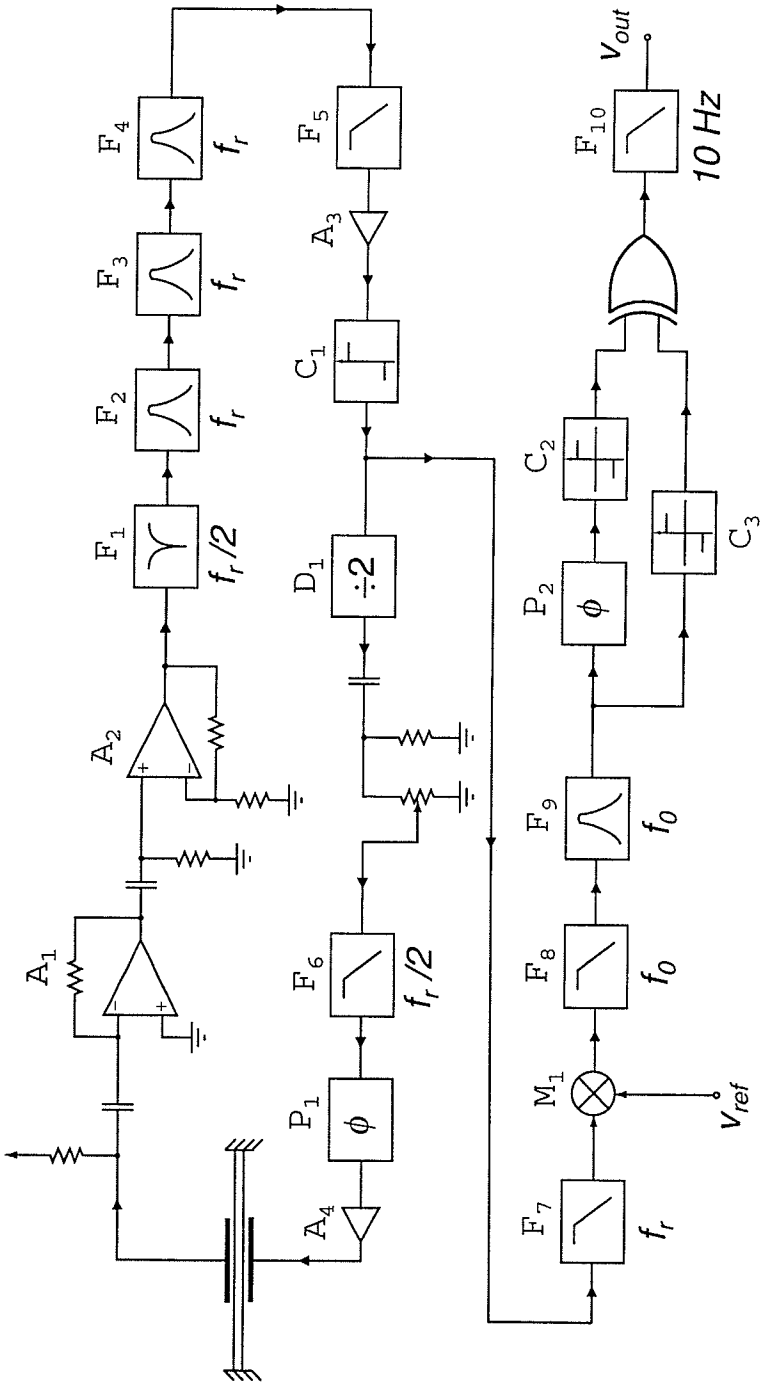

Figure C.1: *Sensing electronics.*

from the sensor is provided by amplifier A_2 (with a gain of $10V/V$) before sending the signal to the filters. Both A_1 and A_2 are put in close proximity of the sensor within the vacuum chamber to prevent the loss of the signal in its transmission to the outside of the vacuum chamber. Amplifier A_3 at the output of the filter block produces a large signal at the input of the comparator C_1. Finally, amplifier A_4 is used to set the amplitude of the drive signal for the shuttle.

Table C.1: *Summary of properties of the circuit blocks. f_c is either the corner frequency of lowpass filters or center frequency of bandpass filters.*

Block	**Function**	**Gain**	f_c	**Order**	Q	**Device**
A_1	Amplifier, transresistance	$10^6\,\Omega$	–	–	–	TLE2072
A_2	Amplifier, non-inverting	$10\,V/V$	–	–	–	TLE2072
F_1	Notch filter	$1\,V/V$	$f_r/2$	2	1	LMF100
F_2	Bandpass filter	$20\,V/V$	f_r	2	50	LMF100
F_3	Bandpass filter	$2\,V/V$	f_r	2	20	LMF100
F_4	Bandpass filter	$2\,V/V$	f_r	2	20	LMF100
F_5	Bessel lowpass filter	$1\,V/V$	$50\,kHz$	4	–	TLE2072
A_3	Amplifier, non-inverting	*Variable*	–	–	–	TLE2072
C_1	Comparator, open-collector	–	–	–	–	LM311
D_1	Frequency divider	–	–	–	–	74HCT74
F_6	Bessel lowpass filter	$1\,V/V$	$25\,kHz$	4	–	TLE2074
P_1	Bessel allpass filter	$1\,V/V$	$25\,kHz$	2	–	TLE2074
A_4	Amplifier, non-inverting	*Variable*	–	–	–	TLE2074
F_7	Chebychev lowpass filter	$1\,V/V$	$45\,kHz$	4	–	TLE2074
M_1	Analog multiplier	$0.1\,V/V$	–	–	–	MPY634
F_8	Butterworth lowpass filter	$1\,V/V$	$100\,Hz$	2	–	TLE2074
F_9	Butterworth bandpass filter	$5\,V/V$	$100\,Hz$	2	2.5	TLE2074
P_2	Allpass filters	$1\,V/V$	$100\,Hz$	2	–	TLE2074
C_2	Comparator, open-collector	–	–	–	–	LM311
C_3	Comparator, open-collector	–	–	–	–	LM311
F_{10}	Butterworth lowpass filter	$1\,V/V$	$10\,Hz$	4	–	TLE2072

C.2 Filters

Various types of filters were used for processing of the resonator signal, including notch, bandpass, lowpass, and allpass filters. The notch filter and some of the bandpass filters were realized using switched-capacitor filters. Other filters were active filters with standard transfer functions. Chebychev filters were used when the highest degree of attenuation was required for out-of-band signals. Butterworth filters were used when a flat response in the passband of the filter was needed. Finally, Bessel filters were employed wherever a smooth transition in the phase response of filters around their cut-off frequencies was required.

C.2.1 Notch filter

The first step of the signal processing is to remove the large interfering signal at the drive frequency. This is necessary as this large signal can cause saturation of the amplifiers and result in generation of signal harmonics, which adversely affect the accuracy of the measurements. The notch filter was realized with a 2^{nd} order switched capacitor filter (block F_1 in Figure C.1). The reason for choosing a switched capacitor filter is the ease of tuning the filter response for testing devices with different resonant frequencies, which is simply achieved by changing its input clock frequency [223].

Although notch filters with high Q values reject a narrower frequency band, a relatively low Q was chosen for this filter. Due to the imperfections in component values, notch filters with a low Q generally have a larger attenuation factor at the rejected frequency band. The high Q bandpass filters that follow the notch filter will compensate for any undesired attenuation of the main signal caused by the notch filter.

C.2.2 Bandpass filters

Bandpass filters F_2, F_3, and F_4 in Figure C.1 are realized with 2^{nd} order switched capacitor filters. In addition to the ability of tuning the frequency response, using switched capacitor filters for these blocks relaxes the requirements on matching of the frequency response of the filters with each other.

Filter F_9 was designed to pass the desired signal at the output of the mixer and its main purpose is to limit the noise bandwidth to the input of the delay network. Schematic of this filter is shown in Figure C.2.

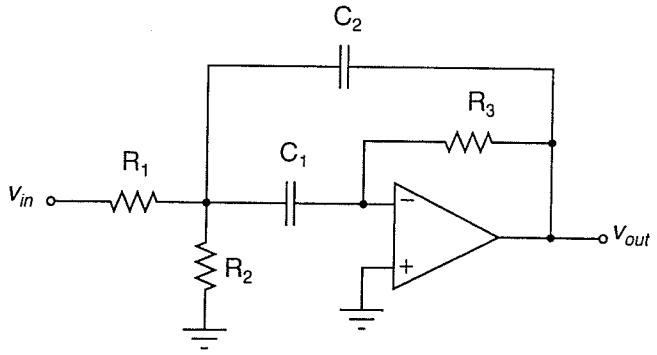

Figure C.2: *Schematic of the bandpass filter after the mixer (Filter F_9).*

C.2.3 Lowpass filters

There are two common topologies for realization of 2^{nd} order filter functions; namely multifeedback and Sallen-Key configurations. Both configurations employ a single OpAmp and a few capacitors and resistors [167, 170, 224]. Multifeedback filters have smaller sensitivities to component values than Sallen-Key filters for high-gain or high-Q filters. On the other hand, Sallen-Key filters provide excellent passband gain

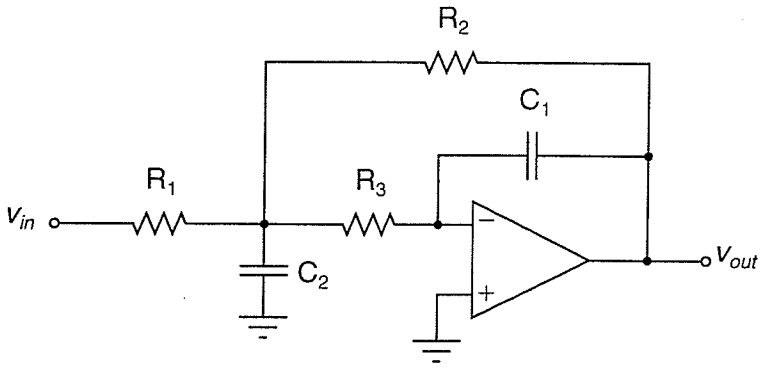

Figure C.3: *Diagram of a mutlifeedback lowpass filter.*

accuracy. Filters F_5 to F_8 are of multifeedback type (see Figure C.3). Filter F_{10} is a 4^{th} order Sallen-Key lowpass filter to reduce the possible inaccuracies that may be caused by the offset voltage of the OpAmps.

C.2.4 Allpass filters

The allpass filters for the frequency-shift measurement circuitry were realized using a circuit similar to what is shown in Figure C.4 [167, 225]. The transfer function of

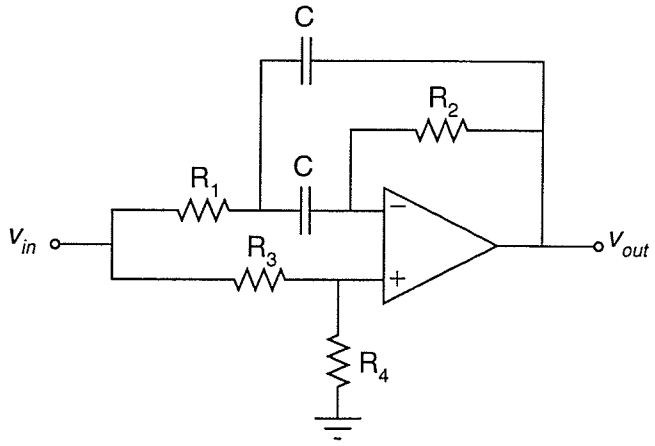

Figure C.4: *Diagram of the allpass filter with controllable quality factor.*

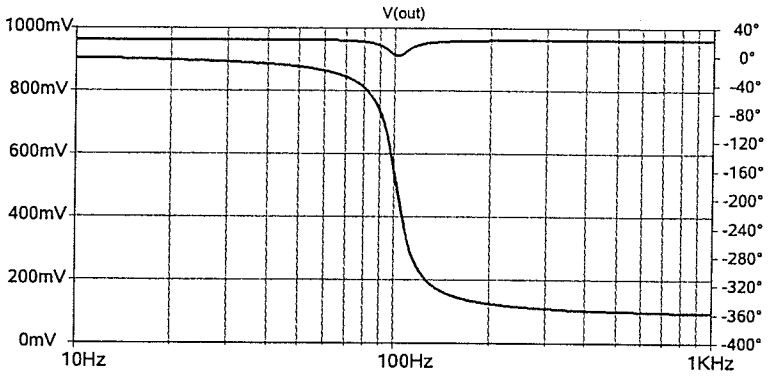

Figure C.5: *Simulated amplitude and phase response of the employed allpass filters.*

the filter is given by:

$$H(s) = K\,\frac{s^2 - a\,s + b}{s^2 + a\,s + b} \tag{C.1}$$

where $a = 2/R_2\,C$, $b = (R_1\,R_2\,C^2)^{-1}$, and $K = R_4/(R_3 + R_4)$ for $R_2\,R_3 = 4R_1\,R_4$. The employed allpass filters have a Q of 5 at $100Hz$ with a gain of ≈ 1.

Simulated response of the designed filters is shown in Figure C.5. As can be seen, the deviation of the component values from their designed ones causes a slight drop in the amplitude response of the filter at $100Hz$.

C.3 Clock generator

Since the stability of the clock signal frequency is not critical, a simple CMOS oscillator was used to generate the clock signals needed by switched capacitor filters (Figure C.6). The duty cycle of this oscillator is close to 50% as required by the filters. The frequency of the output signal of the oscillator is given by [226]:

$$F_{clk} = \frac{1}{2R_1C(\frac{0.4R_2}{R_1+R_2} + 0.69)} \tag{C.2}$$

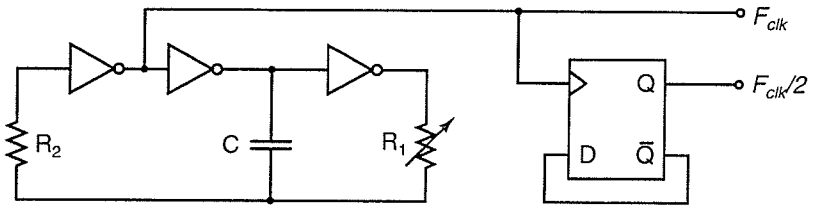

Figure C.6: *Clock signal generator.*

Resistor R_1 can be varied to tune the frequency response of the filters as required.

The generated clock signal is used for the bandpass filters which are tuned to the second harmonic of the drive signal. The frequency of the oscillator output is then divided by two using a T-flipflop to provide the clock signal for the notch filter which is tuned to the drive signal frequency.

Bibliography

[1] D. K. Cheng, *Field and wave electromagnetics*, 2nd ed. USA: Prentice Hall, 1989.

[2] J. E. Lenz, "A review of magnetic sensors," *Proceedings of the IEEE*, vol. 78, no. 6, pp. 973–989, June 1990.

[3] J. Lenz and A. S. Edelstein, "Magnetic sensors and their applications," *IEEE Sensors Journal*, vol. 6, no. 3, pp. 631–649, June 2006.

[4] M. J. Caruso, C. H. Smith, T. Bratland, and R. Schneider. (2004, December) A new perspective on magnetic field sensing. [Online]. Available: http://www.ssec.honeywell.com/magnetic/datasheets/new_pers.pdf

[5] H. A. C. Tilmans, "Micro-mechanical sensors using encapsulated built-in resonant strain gauges," Ph.D. dissertation, University of Twente, The Netherlands, 1993.

[6] P. Ripka, Ed., *Magnetic sensors and magnetometers.* USA: Artech House, 2001.

[7] W. F. Stuart, "Earth's field magnetometry," *Journal of Reports on Progress in Physics*, vol. 35, no. 2, pp. 803–881, May 1972.

[8] P. Ripka, "Advances in fluxgate sensors," *Sensors and Actuators A: Physical*, vol. 106, no. 1-3, pp. 8–14, September 2003.

[9] G. Vértesy, A. Gasparics, and J. Szöllöy, "High sensitivity magnetic field sensor," *Sensors and Actuators A: Physical*, vol. 85, no. 1-3, pp. 202–208, August 2000.

[10] T. Sonoda, R. Ueda, H. Ikemoto, K. Kudo, and K. Kajiwara, "Differentially DC biased type magnetic field sensor of high sensitivity," *IEEE Transactions on Magnetics*, vol. 25, no. 5, pp. 3396–3398, September 1989.

[11] T. Sonoda and R. Ueda, "Distinctive features of magnetic field controlled type magnetic field sensor," *IEEE Transactions on Magnetics*, vol. 25, no. 5, pp. 3393–3395, September 1989.

[12] A. de Sa and K. Heron, "A three-axes fluxgate magnetometer with multiplexed sensors," *Journal of Measurement Science and Technology*, vol. 4, no. 5, pp. 633–634, May 1993.

[13] W. Magnes, D. Pierce, A. Valavanoglou, J. Means, W. Baumjohann, C. T. Russell, K. Schwingenschuh, and G. Graber, "A sigma-delta fluxgate magnetometer for space applications," *Journal of Measurement Science and Technology*, vol. 14, no. 7, pp. 1003–1012, July 2003.

[14] G. Kallias, E. Devlin, C. Christides, and D. Niarchos, "High T_c SQUID sensor system for non-destructive evaluation," *Sensors and Actuators A: Physical*, vol. 85, no. 1-3, pp. 239–243, August 2000.

[15] P. Josephs-Franks, L. Hao, A. Tzalenchuk, J. Davies, O. Kazakova, J. C. Gallop, L. Brown, and J. C. Macfarlane, "Measurement of the spatial sensitivity of miniature SQUIDs using magnetic-tipped STM," *Journal of Superconducting Science and Technoilogy*, vol. 16, no. 12, pp. 1570–1574, December 2003.

[16] K. D. Oh, "Optical fiber fabry-perot interferometer based sensor instrumentation system for low magnetic field measurement," Ph.D. dissertation, Department of Electrical and Computer Engineering, Virginia Polytechnic Institute and State University, USA, 1997.

[17] H. Sohlström, "Fibre optic magnetic field sensors utilizing iron garnet materials," Ph.D. dissertation, Department of Signals, Sensors & Systems, Royal Institute of Technology, KTH, Sweden, 1993.

[18] M. Bock, R. Umathum, J. Sikora, S. Brenner, E. N. Aguor, and W. Semmler, "A Faraday effect position sensor for interventional magnetic resonance imaging," *Physics in medicine & biology*, vol. 51, no. 4, pp. 999–1009, 2006.

[19] G. T. A. Kovacs, *Micromachined transducer sourcebook*. USA: McGraw-Hill, 1998.

[20] K. W. Na, H. S. Park, D. S. Shim, J. S. Hwang, and S. O. Choi, "MEMS-based fluxgate microsensor for digital compass systems," in *Proceedings of the 17th European Conference on Solid-State Transducers, Eurosensors XVII*, Guimars, Portugal, September 2003, pp. 1087–1090.

[21] T. M. Liakopoulos and C. H. Ahn, "A micro-fluxgate magnetic sensor using micromachined planar solenoid coils," *Sensors and Actuators A: Physical*, vol. 77, no. 1, pp. 66–72, September 1999.

[22] S. Kawahito, Y. Sasak, M. Ashiki, and T. Nakamura, "Micromachined solenoids for highly sensitive magnetic sensors," in *Digest of Technical Papers of International Conference on Solid State Sensors and Actuators, TRANSDUCERS '91*, San Francisco, USA, June 1991, pp. 1077–1080.

[23] W.-Y. Choi, J.-S. Hwang, and S.-O. Choi, "The microfluxgate magnetic sensor having closed magnetic path," *IEEE Sensors Journal*, vol. 4, no. 6, pp. 768–771, December 2004.

[24] J. M. Guettler, P. Last, R. Otremba, and S. Buettgenbach, "A novel angular joint-sensor using a fluxgate magnetometer," in *Proceedings of the 4th IEEE Sensors Conference*, Irvine, USA, November 2005.

[25] P. Ripka, X. Li, and J. Fan, "Orthogonal fluxgate effect in electroplated wires," in *Proceedings of the 4th IEEE Sensors Conference*, Irvine, USA, November 2005.

[26] S. A. Solin, R. A. Stradling, T. Thio, and J. W. Bennett, "Thin, horizontal-plane Hall sensors for read heads in magnetic recording," *Journal of Measurement Science and Technology*, vol. 8, no. 10, pp. 1174–1181, October 1997.

[27] Y. H. Seo, K.-H. Han, and Y.-H. Cho, "New plasma Hall effect magnetic sensors: macrosensors versus microsensors," *Sensors and Actuators A: Physical*, vol. 92, no. 1-3, pp. 123–131, August 2001.

[28] R. S. Popovic, Z. Randjelovic, and D. Manic, "Integrated Hall-effect magnetic sensors," *Sensors and Actuators A: Physical*, vol. 91, no. 1-2, pp. 46–50, June 2001.

[29] H. Koehler, B. Kostyshyn, and T. C. Ku, "A note on Hall probe resolution," *IBM Journal*, vol. 5, no. 4, pp. 326–327, October 1961.

[30] J. Hara and T. Hatanaka, "Magnetic field sensor," US Patent 6 777 932, 2004.

[31] N. Haned and M. Missous, "Nano-tesla magnetic field magnetometry using an InGaAs-AlGaAs-GaAs 2DEG Hall sensor," *Sensors and Actuators A: Physical*, vol. 102, no. 3, pp. 216–222, January 2003.

[32] R. J. Braun, "Modular Hall masterslice transducer," *IBM Journal of Research and Developement*, vol. 19, no. 4, pp. 344–352, July 1975.

[33] H. Blanchard, F. D. Montmollin, J. Hubin, and R. S. Popovic, "Highly sensitive Hall sensor in CMOS technology," *Sensors and Actuators A: Physical*, vol. 82, no. 1-3, pp. 144–148, May 2000.

[34] M. Avram, C. Codreanu, O. Neagoe, C. Voitincu, and M. Simion, "A monolithically integrated magnetic field sensor system," in *Proceedings of the International Semiconductor Conference, CAS 2002*, vol. 1, Sinaia, Romania, October 2002, pp. 79–82.

[35] F. L. Bihan, E. Carvou, B. Fortin, R. Rogel, A. C. Salan, and O. Bonnaud, "Realization of polycrystalline silicon magnetic sensors," *Sensors and Actuators A: Physical*, vol. 88, no. 2, pp. 133–138, February 2001.

[36] S. Methfessel, S. Middlehoek, and H. Thomas, "Domain walls in thin Ni-Fe films," *IBM Journal of Research and Development*, vol. 4, no. 2, pp. 96–106, April 1960.

[37] S. Methfessel, "Survey of the field of magnetic semiconductors," *IBM Journal of Research and Development*, vol. 14, no. 3, pp. 207–213, May 1970.

[38] C. Bajorek, S. Krongelb, L. Romankiw, and D. Thompson, "A permalloy current sensor," *IEEE Transactions on Magnetics*, vol. 12, no. 6, pp. 813–815, November 1976.

[39] J. L. Brown, "High sensitivity magnetic field sensor using gmr materials with integrated electronics," in *Proceedings of the IEEE International Symposium on Circuits and Systems, ISCAS '95*, vol. 3, Seattle, USA, April 1995, pp. 1864–1867.

[40] A. Sprotte, K. Buckhorst, W. Brockherde, B. J. Hosticka, and D. Bosch, "CMOS magnetic-field sensor system," *IEEE Journal of Solid-State Circuits*, vol. 29, no. 8, pp. 1002–1005, August 1994.

[41] J. W. A. von Kluge, "Analysis of split-current magnetic field sensitive resistors," *Sensors and Actuators A: Physical*, vol. 93, no. 2, pp. 103–108, September 2001.

[42] B. Morten, M. Prudenziati, G. D. Cicco, A. Bianco, G. Montesperelli, and G. Gusmano, "Thick-film magnetoresistors and related sensors," *Journal of Measurement Science and Technology*, vol. 8, no. 1, pp. 21–28, January 1997.

[43] V. Schmitz and J. Schelten, "Split-electrode drift device as magnetic-field sensor," *Sensors and Actuators A: Physical*, vol. 109, no. 1-2, pp. 25–33, December 2003.

[44] C. P. O. Treutler, "Magnetic sensors for automotive applications," *Sensors and Actuators A: Physical*, vol. 91, no. 1-2, pp. 2–6, June 2001.

[45] G. Riege, K. Ludwig, J. Hauch, and W. Clemens, "GMR sensors for contactless position detection," *Sensors and Actuators A: Physical*, vol. 91, no. 1-2, pp. 7–11, June 2001.

[46] J. L. Prieto, N. Rouse, N. K. Todd, D. Morecroft, J. Wolfman, J. E. Evetts, and M. G. Blamire, "Integrated magnetic field sensor based on magnetoresistive spin valve structures," *Sensors and Actuators A: Physical*, vol. 94, no. 1-2, pp. 64–68, October 2001.

[47] R. S. Popovic, P. M. Drljaca, and C. Schott, "Bridging the gap between AMR, GMR, and Hall magnetic sensors," in *Proceedings of the 3rd International Conference on Microelectronics, MIEL 2002*, vol. 1, Nis, Yugoslavia, May 2002, pp. 55–58.

[48] M. Pannetier, C. Fermon, G. L. Goff, J. Simola, and E. Kerr, "Femtotesla magnetic field measurement with magnetoresistive sensors," *Science Magazine*, vol. 304, no. 5677, pp. 1648–1650, June 2004.

[49] J. M. Daughton and Y. J. Chen, "GMR materials for low field applications," *IEEE Transactions on Magnetics*, vol. 29, no. 6, pp. 2705–2710, November 1993.

[50] A. F. Cobeo, A. Zhukov, J. M. Blanco, V. Larin, and J. Gonzalez, "Magnetoelastic sensor based on GMI of amorphous microwire," *Sensors and Actuators A: Physical*, vol. 91, no. 1-2, pp. 95–98, June 2001.

[51] D. M. Cannon, W. R. Dempwolf, J. M. Schmalhorst, F. B. Shelledy, and R. D. Silkensen, "Design and performance of a magnetic head for a high-density tape drive," *IBM Journal of Research and Development*, vol. 30, no. 3, pp. 270–277, May 1986.

[52] S. Arana, E. Casta, and F. J. Gracia, "High temperature magnetic position sensor based on a giant magnetoresistive alloy," in *Proceedings of the 17th European Conference on Solid-State Transducers, Eurosensors XVII*, Guimars, Portugal, September 2003, pp. 1079–1082.

[53] M. Vopálenský, P. Ripka, and A. Platil, "Precise magnetic sensors," *Sensors and Actuators A: Physical*, vol. 106, no. 1-3, pp. 38–42, September 2003.

[54] M. Takezawa, H. Kikuchi, K. Ishiyama, M. Yamaguchi, and K. I. Arai, "Micro magnetic thin-film sensor using LC resonance," *IEEE Transactions on Magnetics*, vol. 33, no. 5, pp. 3400–3402, September 1997.

[55] D. Atkinson, P. T. Squire, M. G. Maylin, and J. Gore, "An integrating magnetic sensor based on the giant magneto-impedance effect," *Sensors and Actuators A: Physical*, vol. 81, no. 1-3, pp. 82–85, August 2000.

[56] H. Hauser, R. Steindl, C. Hausleitner, A. Pohl, and J. Nicolics, "Wirelessly interrogable magnetic field sensor utilizing giant magneto-impedance effect and surface acoustic wave devices," *IEEE Transactions on Instrumentation and Measurement*, vol. 49, no. 3, pp. 648–652, June 2000.

[57] A. W. Vinal, "A magnetic sensor utilizing an avalanching semiconductor device," *IBM Journal of Research and Development*, vol. 25, no. 2, pp. 196–201, May 1981.

[58] P. S. A. Kumar and J. C. Lodder, "The spin-valve transistor," *Journal of Physics D: Applied Physics*, vol. 33, no. 22, pp. 2911–2920, November 2000.

[59] R. Jansen, "The spin-valve transistor: a review and outlook," *Journal of Physics D: Applied Physics*, vol. 36, no. 19, pp. R289–R308, 2003.

[60] P. Losantos, C. C. D. Flandre, and J. P. Eggermont, "Magnetic-field sensor based on a thin-film SOI transistor," *Sensors and Actuators A: Physical*, vol. 67, no. 1-3, pp. 96–101, May 1998.

[61] M. Paranjape, I. Filanovsky, and L. J. Ristic, "Integrated micromachined magnetic field sensor with on-chip support circuitry," *Applied Physics Letters*, vol. 64, no. 12, pp. 1576–1578, March 1994.

[62] S. Kordic and P. J. A. Munter, "Three-dimensional magnetic-field sensors," *IEEE Transactions on Electron Devices*, vol. 35, no. 6, pp. 771–779, June 1988.

[63] D. M. Schaadt, E. T. Yu, S. Sankar, and A. E. Berkowitz, "A monolithic field-effect-transistor-amplified magnetic field sensor," *Applied Physics Letters*, vol. 75, no. 5, pp. 731–733, August 1999.

[64] R. S. Popovic and H. P. Baltes, "A CMOS magnetic field sensor," *IEEE Journal of Solid-State Circuits*, vol. 18, no. 4, pp. 426–428, August 1983.

[65] J. J. Clark, "CMOS magnetic sensor arrays," in *Technical Digest of the IEEE Solid-State Sensor and Actuator Workshop*, Hilton Head Island, USA, June 1988, pp. 72–75.

[66] D. Misra, "A novel CMOS magnetic field sensor array," *IEEE Journal of Solid-State Circuits*, vol. 25, no. 2, pp. 623–625, April 1990.

[67] B. Wagner, M. Kreutzer, and W. Benecke, "Linear and rotational magnetic micromotors fabricated using silicon technology," in *Proceedings of the 5th IEEE Micro Electro Mechanical Systems Conference, MEMS '92*, Travemunde, Germany, February 1992, pp. 183–189.

[68] B. Wagner and W. Benecke, "Microfabricated actuator with moving permanent magnet," in *Proceedings of the 4th IEEE Micro Electro Mechanical Systems Conference, MEMS '91*, Nara, Japan, January 1991, pp. 27–32.

[69] C. Liu and Y. W. Yi, "Micromachined magnetic actuators using electroplated permalloy," *IEEE Transactions on Magnetics*, vol. 35, no. 3, pp. 1976–1985, May 1999.

[70] J. W. Judy, "Batch-fabricated ferromagnetic microactuators with silicon flexures," Ph.D. dissertation, Department of Electrical Engineering and Computer Sciences, University of California, Berkeley, USA, 1996.

[71] J. W. Judy, R. S. Muller, and H. H. Zappe, "Magnetic microactuation of polysilicon flexure structures," *IEEE Journal of Microelectromechanical Systems*, vol. 4, no. 4, pp. 162 – 169, December 1995.

[72] M. Capanu, J. G. Boyd, and P. J. Hesketh, "Design, fabrication, and testing of a bistable electromagnetically actuated microvalve," *IEEE Journal of Microelectromechanical Systems*, vol. 9, no. 2, pp. 181–189, June 2000.

[73] C. H. Ahn, Y. J. Kim, and M. G. Allen, "A planar variable reluctance magnetic micromotor with fully integrated stator and wrapped coils," in *Proceedings of the 6th IEEE Micro Electro Mechanical Systems Conference, MEMS '93*, Fort Lauderdale, USA, February 1993, pp. 1–6.

[74] R. P. Cowburn and A. M. Moulin, "High sensitivity measurement of magnetic fields using microcantilevers," *Applied Physics Letters*, vol. 71, no. 15, pp. 2202–2204, October 1997.

[75] M. Willemin, C. Rossel, J. Brugger, M. H. Despont, H. Rothuizen, P. Vettiger, J. Hofer, and H. Keller, "Piezoresistive cantilever designed for torque magnetometry," *Journal of Applied Physics*, vol. 83, no. 3, pp. 1163–1170, February 1998.

[76] L. M. Miller, J. A. Podosek, E. Kruglick, T. W. Kenny, J. A. Kovacich, and W. J. Kaiser, "A μ-magnetometer based on electron tunneling," in *Proceedings of the 9th IEEE Micro Electro Mechanical Systems Conference, MEMS '96*, San Diego, USA, February 1996, pp. 467–472.

[77] D. DiLella, L. J. Whitman, R. J. Colton, T. W. Kenny, W. J. Kaiser, E. C. Vote, J. A. Podosek, and L. M. Miller, "A micromachined magnetic-field sensor based on an electron tunneling displacement transducer," *Sensors and Actuators A: Physical*, vol. 86, no. 1-2, pp. 8–20, October 2000.

[78] R. J. Kretschmann and R. D. Harris, "Magnetic field sensor using microelectromechanical system," US Patent 6 664 786, 2003.

[79] J. Kaienburg, M. Lutz, B. Maihofer, and R. Schellin, "A precise and contactless angle detection sensor using surface micromachining technology," in *Proceedings of the 11th IEEE Micro Electro Mechanical Systems Conference, MEMS '98*, Heidelberg, Germany, January 1998, pp. 367–371.

[80] H. Emmerich and M. Schofthaler, "Magnetic field measurements with a novel surface micromachined magnetic-field sensor," *IEEE Transactions on Electron Devices*, vol. 47, no. 5, pp. 927–977, May 2000.

[81] L. Latorre, V. Beroulle, and P. Nouet, "Design of CMOS MEMS based on mechanical resonators using a RF simulation approach," *IEEE Transactions on Computer-Aided Design of Integrated Circuits and Systems*, vol. 23, no. 6, pp. 962–967, June 2004.

[82] Z. Kádár, A. Bossche, J. R. Mollinger, and P. M. Sarro, "Magnetic-field measurements using an integrated resonant magnetic-field sensor," *Sensors and Actuators A: Physical*, vol. 70, no. 3, pp. 225–232, October 1998.

[83] B. Eyre, K. S. J. Pister, and W. Kaiser, "Resonant mechanical magnetic sensor in standard CMOS," *IEEE Electron Device Letters*, vol. 19, no. 12, pp. 496–498, December 1998.

[84] A. B. Temnykh and R. V. E. Lovelace, "Electro-mechanical resonant magnetic field sensor," *Journal of Nuclear Instruments and Methods in Physics Research Section A: Accelerators, Spectrometers, Detectors and Associated Equipment*, vol. 484, no. 1-3, pp. 95–101, May 2002.

[85] T. C. Leichle, M. V. Arx, S. Reiman, I. Zana, W. Ye, and M. G. Allen, "A low-power resonant micromachined compass," *Journal of Micromechanics and Microengineering*, vol. 14, no. 4, pp. 462–470, April 2004.

[86] T. C. Leichle, M. von Arx, and M. G. Allen, "A micromachined resonant magnetic field sensor," in *Proceedings of the 14th IEEE Micro Electro Mechanical Systems Conference, MEMS '01*, Interlaken, Switzerland, January 2001, pp. 274–277.

[87] S. Baglio, L. Latorre, and P. Nouet, "Resonant magnetic field microsensors in standard CMOS technology," in *Proceedings of the 16th IEEE Instrumentation and Measurement Technology Conference, IMTC/99*, vol. 1, Venice, Italy, May 1999, pp. 452–457.

[88] T. C. Leichle, W. Ye, and M. G. Allen, "A μW micromachined magnetic compass," in *Proceedings of the 16th IEEE Micro Electro Mechanical Systems Conference, MEMS '03*, Tokyo, Japan, January 2003, pp. 514–517.

[89] P. D. D. Schwindt, S. Knappe, V. Shah, L. Hollberg, J. Kitching, L.-A. Liew, and J. Moreland, "Chip-scale atomic magnetometer," *Applied Physics Letters*, vol. 85, no. 26, pp. 6409–6411, December 2004.

[90] P. Schwindt, S. Knappe, V. Shah, L.-A. Liew, J. Moreland, L. Hollberg, and J. Kitching, "Microfabricated atomic magnetometer," in *Proceedings of the 4th IEEE Sensors Conference*, Irvine, USA, November 2005.

[91] D. A. Horsley, N. Wongkomet, R. Horowitz, and A. P. Pisano, "Precision positioning using a microfabricated electrostatic actuator," *IEEE Transactions on Magnetics*, vol. 35, no. 2, pp. 993–999, March 1999.

[92] P. B. Chu and S. J. Pister, "Analysis of closed-loop control of parallel-plate electrostatic microgrippers," in *Proceedings of the IEEE International Conference on Robotics and Automation*, vol. 1, San Diego, USA, May 1994, pp. 820–825.

[93] M. J. Sinclair, "A high force low area MEMS thermal actuator," in *Proceedings of the Seventh Intersociety Conference on Thermal and Thermomechanical Phenomena in Electronic Systems, ITHERM 2000*, vol. 1, Redmond, USA, May 2000, pp. 127–132.

[94] B. Rashidian and M. G. Allen, "Electrothermal microactuators based on dielectric loss heating," in *Proceedings of the 6th IEEE Micro Electro Mechanical Systems Conference, MEMS '93*, Atlanta, USA, February 1993, pp. 24–29.

[95] C. C. Barrona, J. H. Comtoisa, and M. A. Michalicek, "Electrothermal actuators fabricated in four-level planarized surface micromachined polycrystalline silicon," *Sensors and Actuators A: Physical*, vol. 70, no. 1-2, pp. 23–31, October 1998.

[96] H. Toshiyoshi, H. Fujita, and T. Ueda, "A piezoelectrically operated optical chopper by quartz micromachining," *IEEE Journal of Microelectromechanical Systems*, vol. 4, no. 1, pp. 3–9, March 1995.

[97] D. J. Laser and J. G. Santiago, "A review of micropumps," *Journal of Micromechanics and Microengineering*, vol. 14, no. 6, pp. R35–R68, June 2004.

[98] R. Legtenberg, A. W. Groeneveld, and M. Elwenspoek, "Comb-drive actuators for large displacements," *Journal of Micromechanics and Microengineering*, vol. 6, no. 3, pp. 320–329, September 1996.

[99] M. A. Rosa, S. Dimitrijev, and H. B. Harrison, "Enhanced electrostatic force generation capability of angled comb finger design used in electrostatic comb-drive actuators," *IEE Electronics Letters*, vol. 34, no. 18, pp. 1787–1788, September 1998.

[100] W. O. Davis, "Mechanical analysis and design of vibratory micromachined gyroscopes," Ph.D. dissertation, Department of Mechanical Engineering, University of California, Berkeley, USA, 2001.

[101] N. Yazdi, F. Ayazi, and K. Najafi, "Micromachined inertial sensors," *Proceedings of the IEEE*, vol. 86, no. 8, pp. 1640–1659, August 1998.

[102] L. Lin, R. T. Howe, and A. P. Pisano, "Microelectromechanical filters for signal processing," *IEEE Journal of Microelectromechanical Systems*, vol. 7, no. 3, pp. 286–294, September 1998.

[103] C. T.-C. Nguyen, "Frequency-selective MEMS for miniaturized low-power communication devices," *IEEE Transactions on Microwave Theory and Techniques*, vol. 47, no. 8, pp. 1486–1503, August 1999.

[104] ——, "Micromechanical resonators for oscillators and filters," in *Proceedings of the IEEE Ultrasonics Symposium*, vol. 1, Ann Arbor, USA, November 1995, pp. 489–499.

[105] C. T.-C. Nguyen and R. T. Howe, "An integrated CMOS micromechanical resonator high-Q oscillator," *IEEE Journal of Solid-State Circuits*, vol. 34, no. 4, pp. 440–455, April 1999.

[106] R. T. Howe, "Resonant microsensors," in *Technical Digest of the 4th International Conference on Solid-State Sensors and Actuators (Transducers '87)*, Tokyo, Japan, June 1987, pp. 843–848.

[107] W. C. Tang, T. C. H. Nguyen, and R. T. Howe, "Laterally driven polysilicon resonant microstructures," in *Proceedings of the 2nd IEEE Micro Electro Mechanical Systems Conference, MEMS '89*, Salt Lake City, USA, February 1989, pp. 53–59.

[108] W. C. Tang, "Electrostatic comb drive for resonant sensor and actuator applications," Ph.D. dissertation, Department of Electrical Engineering and Computer Sciences, University of California, Berkeley, USA, 1992.

[109] C. T.-C. Nguyen, "Electromechanical characterization of microresonators for circuit applications," Master's thesis, Department of Electrical Engineering and Computer Sciences, University of California, Berkeley, USA, 1991.

[110] ——, "Micromechanical signal processors," Ph.D. dissertation, Department of Electrical Engineering and Computer Sciences, University of California, Berkeley, USA, 1994.

[111] L. Fan, Y. C. Tai, and R. S. Muller, "IC-processed electrostatic micro-motors," in *Technical Digest of the 1998 International Electron Devices Meeting*, San Francisco, USA, December 1988, pp. 666–669.

[112] M. Mehregany, P. Nagarkar, S. D. Senturia, and J. H. Lang, "Operation of microfabricated harmonic and ordinary side-drive motors," in *Proceedings of the 3rd IEEE Micro Electro Mechanical Systems Conference, MEMS '90*, Napa Valley, USA, February 1990, pp. 1–8.

[113] Y. C. Tai, L. S. Fan, and R. S. Muller, "IC-processed micro-motors: design, technology, and testing," in *Proceedings of the 2nd IEEE Micro Electro Mechanical Systems Conference, MEMS '89*, Salt Lake City, USA, February 1989, pp. 1–6.

[114] W. C. Tang, M. G. Lim, and R. T. Howe, "Electrostatic comb drive levitation and control method," *IEEE Journal of Microelectromechanical Systems*, vol. 1, no. 4, pp. 170–178, December 1992.

[115] T. A. W. Roessig, "Integrated MEMS tuning fork oscillators for sensor applications," Ph.D. dissertation, Department of Mechanical Engineering, University of California, Berkeley, USA, 1998.

[116] K. A. Shaw, Z. L. Zhang, and N. C. MacDonald, "SCREAM I: a single mask, single-crystal silicon process for microelectromechanical structures," in *Proceedings of the 6th IEEE Micro Electro Mechanical Systems Conference, MEMS '93*, Atlanta, USA, February 1993, pp. 155–160.

[117] J. W. Weigold, W. H. Juan, and S. W. Pang, "Etching and boron diffusion of high aspect ratio Si trenches for released resonators," *Journal of Vaccum Science and Technology, B*, vol. 15, no. 2, pp. 267–272, March 1997.

[118] F. Ayazi and K. Najafi, "High aspect-ratio combined poly and single-crystal silicon (HARPSS) MEMS technology," *IEEE Journal of Microelectromechanical Systems*, vol. 9, no. 3, pp. 288–294, September 2000.

[119] S. Pourkamali, A. Hashimura, R. Abdolvand, G. K. Ho, A. Erbil, and F.Ayazi, "High-Q single crystal silicon HARPSS capacitive beam resonators with self-aligned sub-100-nm transduction gaps," *IEEE Journal of Microelectromechanical Systems*, vol. 12, no. 4, pp. 487–496, August 2003.

[120] S. D. Senturia, *Microsystem design.* USA: Kluwer Academic Publishers, 2000.

[121] S. Timoshenko, *Strength of materials, Part 1*, 3rd ed. USA: Krieger Publishing, 1983.

[122] S. Diamantis, M. Ahmadi, G. A. Jullien, and W. C. Miller, "A programmable MEMS bandpass filter," in *Proceedings of the 43rd IEEE Midwest Symposium on Circuits and Systems*, vol. 1, Lansing, USA, August 2000, pp. 522–525.

[123] K. Y. Park, C. W. Lee, H. S. Jang, Y. S. Oh, and B. J. Ha, "Capacitive sensing type surface micromachined silicon accelerometer with a stiffness tuning capability," in *Proceedings of the 11th IEEE Micro Electro Mechanical Systems Conference, MEMS '98*, Heidelberg, Germany, January 1998, pp. 637–642.

[124] M. Elwenspoek and R. Wiegerink, *Mechanical microsensors.* Germany: Springer-Verlag, 2001.

[125] K. A. Gibbons, J. T. Borenstein, D. S. Nokes, M. S. Weinberg, and D. L. Trumper, "The design, fabrication, and testing of a micromechanical silicon oscillating accelerometer," in *Proceedings of the AIAA Conference on Guidance and Control*, Boston, USA, August 1998, pp. 1296–1306.

[126] W. C. Young and R. G. Budynas, *Roark's formulas for stress and strain*, 7th ed. USA: McGraw-Hill, 2002.

[127] L. X. Zhang and Y. P. Zhao, "Electromechanical model of RF MEMS switches," *Journal of Microsystem Technologies*, vol. 9, no. 6-7, pp. 420–426, September 2003.

[128] F. P. Beer and E. R. Johnston, *Mechanics of materials*, 2nd ed. Singapore: McGraw-Hill, 1992.

[129] J. Case, L. Chilver, and C. T. F. Ross, *Strength of materials and structures*, 4th ed. United Kingdom: Arnold Publishers, 1999.

[130] C. A. Deseor and E. H. Kuh, *Basic circuit theory.* McGraw-Hill, 1969, Persian translation.

[131] J. W. Harris and H. Stocker, *Handbook of Mathematics and Computational Science.* USA: Springer-Verlog, 1998.

[132] C. M. Wang, C. Y. Wang, and J. N. Reddy, *Exact solutions for buckling of structural members.* USA: CRC Press, 2004.

[133] S. Dunkerley, "On the whirling and vibrations of shafts," *Philosophical Transactions of Royal Society of London*, vol. 185, pp. 279–360, 1894.

[134] W. T. Thomson, *Theory of vibration with applications*, 2nd ed. Englewood Cliffs, USA: Prentice-Hall, 1981.

[135] I. Mirolyubov, S. Engalychev, N. Sergievsky, F. Almametov, N. Kuritsyn, K. Smirnov-Vasilyev, and L. Yashina, *An aid to solving problems in strength of materials.* Moscow, Russia: Mir Publishers, 1983, translated from Russian by Yuri Ermolyev.

[136] B. Bahreyni, F. Najafi, and C. Shafai, "Piezoresistive sensing with twin-beam structures in standard MEMS foundry processes," *Sensors and Actuators A: Physical*, vol. 127, no. 2, pp. 325–331, March 2006.

[137] J. A. King, Ed., *Materials handbook for hybrid microelectronics.* USA: Artech House, 1988.

[138] Y. A. Burenkov and S. P. Nikanorov, "Temperature dependence of elastic constants of silicon," *Journal of the Soviet Physics of the Solid State*, vol. 16, pp. 963–964, 1974.

[139] R. Hull, Ed., *Properties of Crystalline Silicon.* Institution of Electrical Engineers, 1999.

[140] L. Thomas, *Fundamentals of heat transfer.* Prentice-Hall, 1980.

[141] F. Incropera and D. DeWitt, *Fundamentals of heat and mass transfer*, 2nd ed. Wiley, 1985.

[142] J. Brotz, "Damping in CMOS-MEMS resonators," Master's thesis, Department of Electrical Engineering and Computer Engineering, Carnegie Mellon University, USA, 2004.

[143] A. H. Nayfeh and M. I. Younis, "A new approach to the modeling and simulation of flexible microstructures under the effect of squeeze-film damping," *Journal of Micromechanics and Microengineering*, vol. 14, no. 2, pp. 170–181, February 2004.

[144] R. Darling and J. Yang, "Compact analytical models for squeeze film damping with arbitrary venting conditions," in *Proceedings of the IEEE International Conference on Solid State Sensors and Actuators, TRANSDUCERS '97*, vol. 2, Chicago, USA, June 1997, pp. 1113–1116.

[145] Y. Cho, A. P. Pisano, and R. T. Howe, "Viscous damping model for laterally oscillating microstructures," *IEEE Journal of Microelectromechanical Systems*, vol. 3, no. 2, pp. 81–87, June 1994.

[146] C. Bourgeois, F. Porret, and A. Hoogerwerf, "Analytical modeling of squeeze film damping in accelerometers," in *Technical Digest of the 9th International Conference on Solid-State Sensors and Actuators (Transducers '97)*, vol. 2, Chicago, USA, June 1997, pp. 1117–1120.

[147] Z. Xia and W. C. Tang, "Viscous air damping in laterally driven microresonators," in *Proceedings of the 7th IEEE Micro Electro Mechanical Systems Conference, MEMS '94*, Oiso, Japan, January 1994, pp. 199–204.

[148] A. Duwel, M. Weinstein, J. Gorman, J. Borenstein, and P. Ward, "Quality factors of MEMS gyros and the role of thermoelastic damping," in *Proceedings of the 15th IEEE Micro Electro Mechanical Systems Conference, MEMS '02*, Las Vegas, USA, January 2002, pp. 214–219.

[149] M. I. Younis, "Modeling and simulation of microelectromechanical systems in multi-physics fields," Ph.D. dissertation, Virginia Polytechnic Institute and State University, Blacksburg, Virginia, June 2004.

[150] G. K. Fedder, "Simulation of microelectromechanical systems," Ph.D. dissertation, Department of Electrical Engineering and Computer Sciences, University of California, Berkeley, USA, 1994.

[151] W. Ye, W. Hemmert, D. Freeman, and J. White, "Air damping in laterally oscillating microresonators: a numerical and experimental study," *IEEE Journal of Microelectromechanical Systems*, vol. 12, no. 5, pp. 557–566, October 2003.

[152] T. Veijola and M. Turowski, "Compact damping models for laterally moving microstructures with gas-rarefaction effects," Circuit Theory Laboratory, Department of Electrical and Communications Engineering, Helsinki University of Technology, Helsinki, Finland, Tech. Rep., 2000.

[153] S. A. Campbell, *The science and engineering of microelectronic fabrication.* USA: Oxford University Press, 1996.

[154] T. Veijola and M. Turowski, "Compact damping models for laterally moving microstructures with gas-rarefaction effects," *IEEE Journal of Microelectromechanical Systems*, vol. 10, no. 2, pp. 263–273, June 2001.

[155] K. Chang, S. Lee, and S. Li, "Squeeze film damping effect on a MEMS torsion mirror," *Journal of Micromechanics and Microengineering*, vol. 12, no. 5, pp. 556–561, September 2002.

[156] G. Wong, "Behavioral modeling and simulation of MEMS electrostatic and thermomechanical effects," Master's thesis, Department of Electrical Engineering and Computer Engineering, Carnegie Mellon University, USA, 2004.

[157] T. Veijola, K. Ruokonen, and I. Tittonen, "Compact model for the squeezed-film damping including the open border effects," in *Technical Proceedings of the 2001 International Conference on Modeling and Simulation of Microsystems, MSM 2001*, South Carolina, U.S.A., March 2001, pp. 76–79.

[158] *ANSYS version 8.1*, ANSYS Inc., Southpointe, 275 Technology Drive, Canonsburg, PA 15317, USA, 2004. [Online]. Available: http://ansys.com

[159] *Introduction to MicraGEM: A Silicon-on-Insulator Based Micromachining Process*, 3rd ed., Canadian Microelectronics Corporation, December 2004.

[160] W. S. Jr., B. Yuan, and R. Edwards, "A new technique for measuring the mechanical properties of thin films," *IEEE Journal of Microelectromechanical Systems*, vol. 6, no. 3, pp. 193–199, September 1997.

[161] S. Franssila, *Introduction to Microfabrication.* UK: John Wiley and Sons, 2004.

[162] D. A. Koester, R. Mahadevan, B. Hardy, and K. W. Markus, *MUMPs design handbook*, 7th ed., Cronos Integrated Microsystems, 3026 Cornwallis Rd. Research Triangle Park, NC 27709, 2001.

[163] J. Zhao, "Experimental characterization of dynamic behavior of micromachined resonators," Master's thesis, Department of Electrical and Computer Engineering, University of Manitoba, Winnipeg, Manitoba, Canada, 2005.

[164] S. R. Trout, "Use of Helmholtz coils for magnetic measurements," *IEEE Transactions on Magnetics*, vol. 24, no. 4, pp. 2108–2111, July 1988.

[165] W. M. Frix, G. G. Karady, and B. A. Venetz, "Comparison of calibration systems for magnetic field measurement equipment," *IEEE Transactions on Power Delivery*, vol. 9, no. 1, pp. 100–108, January 1994.

[166] E. L. Bronaugh, "Helmholtz coils for calibration of probes and sensors: limits of magnetic field accuracy and uniformity," in *IEEE International Symposium on Electromagnetic Compatibility*, Atlanta, USA, August 1995, pp. 72 – 76.

[167] R. Schaumann and M. E. V. Valkenburg, *Design of Analog Filters*, 2nd ed. USA: Oxford University Press, 2001.

[168] G. S. Moschytz, *Active filter design handbook : for use with programmable pocket calculators and mini computers.* USA: Wiley, 1981.

[169] T. Deliyannis, Y. Sun, and J. K. Fidler, *Continuous-Time Active Filter Design*, ser. Electronic Engineering Systems. CRC Press, December 1998, vol. 12.

[170] G. C. Temes and S. K. Mitra, Eds., *Modern Filter Theory and Design.* USA: Wiley, 1973.

[171] M. N. Horenstein and P. R. Stone, "A micro-aperture electrostatic field mill based on MEMS technology," *Journal of Electrostatics*, vol. 51-52, pp. 515–521, May 2001.

[172] H. B. Chan, V. A. Aksyuk, R. N. Kleiman, D. J. Bishop, and F. Capasso, "Nonlinear micromechanical Casimir oscillator," *Physical Review Letters*, vol. 87, no. 21, pp. 211 801–1–211 801–4, November 2001.

[173] C. Gui, R. Legtenberg, H. A. C. Tilmans, J. H. J. Fluitman, and M. Elwenspoek, "Nonlinearity and hysteresis of resonant strain gauges," *IEEE Journal of Microelectromechanical Systems*, vol. 7, no. 1, pp. 122–127, March 1998.

[174] V. Kaajakari, T. Mattila, A. Oja, and H. Sepp, "Nonlinear limits for single-crystal silicon microresonators," *IEEE Journal of Microelectromechanical Systems*, vol. 13, pp. 715–724, October 2004.

[175] B. P. Otis and J. M. Rabaey, "A 300μW 1.9GHz CMOS oscillator utilizing micromachined resonators," *IEEE Journal of Solid-State Circuits*, vol. 38, pp. 1271–1274, July 2003.

[176] G. H. McGibney, "Wireless networking with simple terminals," Ph.D. dissertation, Department of Electrical and Computer Engineering, The University of Calgary, Canada, 2000.

[177] N. R. Karpov, "Vernier method of measuring time intervals," *Journal of Measurement techniques*, vol. 23, no. 9, pp. 817–820, September 1980.

[178] T. R. Albrecht, P. Grtitter, D. Horne, and D. Rugar, "Frequency modulation detection using high-Q cantilevers for enhanced force microscope sensitivity," *Journal of Applied Physics*, vol. 69, no. 2, pp. 668–673, January 1991.

[179] J. G. Webster, Ed., *The Measurement, Instrumentation and Sensors Handbook*, ser. Electrical Engineering Handbook. USA: CRC Press, 1999, vol. 14.

[180] W. Rosenkranz, "Phase-locked loops with limiter phase detectors in the presence of noise," *IEEE Transactions on Communications*, vol. 30, no. 10, pp. 2297–2304, October 1982.

[181] T. Kenny, "Nanomete-scale force sensing with MEMS devices," *IEEE Sensors Journal*, vol. 1, no. 2, pp. 148–157, August 2001.

[182] J. R. Vig and Y. Kim, "Noise in microelectromechanical system resonators," *IEEE Transactions on Ultrasonics, Ferroelectrics and Frequency Control*, vol. 46, no. 6, pp. 1558–1565, November 1999.

[183] K. Huang, *Introduction to statistical physics.* United Kingdom: Taylor and Francis, 2001.

[184] H. L. Pecseli, *Fluctuations in physical systems.* United Kingdom: Cambridge University Press, 2000.

[185] M. J. Buckingham, *Noise in electronic devices and systems.* United Kingdom: Ellis Harwood, 1983.

[186] P. R. Gray, P. J. Hurst, S. H. Lewis, and R. G. Meyer, *Analysis and design of analog integrated circuits*, 4th ed. USA: John Wiley and Sons, 2000.

[187] V. Annovazzi-Lodi and S. Merlo, "Mechanicalthermal noise in micromachined gyros," *Microelectronics Journal*, vol. 30, no. 12, pp. 1227–1230, December 1999.

[188] G. M. Rebeiz, "Phase-noise analysis of MEMS-based circuits and phase shifters," *IEEE Transactions on Microwave Theory and Techniques*, vol. 50, no. 5, pp. 1316–1323, May 2002.

[189] T. B. Gabrielson, "Mechanical-thermal noise in micromachined acoustic and vibration sensors," *IEEE Transactions on Electron Devices*, vol. 40, no. 5, pp. 903–909, May 1993.

[190] A. N. Cleland and M. L. Roukes, "Noise processes in nanomechanical resonators," *Journal of Applied Physics*, vol. 92, no. 5, pp. 2758–2769, September 2002.

[191] T. Hofler and S. L. Garrett, "Thermal noise in a fiber optic sensor," *Journal of Acoustical Society of America*, vol. 84, no. 2, pp. 471–475, August 1988.

[192] F. Reif, *Fundamentals of statistical and thermal physics.* USA: McGraw-Hill, 1965.

[193] W. P. Robins, *Phase noise in signal sources; theory and application.* UK: Peter Pregrinus, 1982.

[194] B. Razavi, *Design of analog CMOS integrated circuits.* USA: McGraw Hill, 2001.

[195] IEEE Standards Coordinating Committee 27 on Time and Frequency, "IEEE Std 1139-1999; IEEE standard definitions of physical quantities for fundamental frequency and time metrology - random instabilities," The Institute of Electrical and Electronics Engineers, 345 East 47th Street, New York, NY 10017, USA, Tech. Rep., 1999.

[196] IEEE Standards Board, "IEEE Std 1139-1988; IEEE standard definitions of physical quantities for fundamental frequency and time metrology," The Institute of Electrical and Electronics Engineers, Inc, 345 East 47th Street, New York, NY 10017, USA, Tech. Rep., 1988.

[197] T. H. Lee and A. Hajimiri, "Oscillator phase noise: A tutorial," *IEEE Journal of Solid-State Circuits*, vol. 35, no. 3, pp. 326–336, March 2000.

[198] B. Razavi, "A study of phase noise in CMOS oscillators," *IEEE Journal of Solid-State Circuits*, vol. 31, no. 3, pp. 331–343, March 1996.

[199] K. A. Kouznetsov and R. G. Meyer, "Phase noise in LC oscillators," *IEEE Journal of Solid-State Circuits*, vol. 35, no. 8, pp. 1244–1248, August 2000.

[200] P. Réfrégier, *Noise theory and application to physics.* USA: Springer-Verlag, 2003.

[201] M. Planat, Ed., *Noise, oscillators, and algebraic randomness: from noise in communication systems to number theory.* Germany: Springer-Verlag, 2000.

[202] A. Demir and A. L. Sangiovanni-Vincentelli, "Simulation and modeling of phase noise in open-loop oscillators," in *Proceedings of the IEEE Custom Integrated Circuits Conference*, San Diego, USA, May 1996.

[203] A. Demir, E. W. Y. Liu, and A. L. Sangiovanni-Vincentelli, "Time-domain non-Monte Carlo noise simulation for nonlinear dynamic circuits with arbitrary excitations," *IEEE Transactions on Computer-Aided Design of Integrated Circuits and Systems*, vol. 15, no. 5, pp. 493–505, May 1996.

[204] L. Dai and R. Harjani, "Analysis and design of low-phase-noise ring oscillators," in *Proceedings of the 2000 International Symposium on Low Power Electronics and Design, ISLPED '00*, Rapallo, Italy, July 2000, pp. 289–294.

[205] G. V. Klimovitch, "A nonlinear theory of near-carrier phase noise in free-running oscillators," in *Proceedings of the 2000 Third IEEE International Caracas Conference on Devices, Circuits and Systems*, Cancun, Mexico, March 2000, pp. T80/1–T80/6.

[206] H.-G. Ryu, Y. S. Li, and J.-S. Park, "Nonlinear analysis of the phase noise in the OFDM communication system," *IEEE Transactions on Consumer Electronics*, vol. 50, no. 1, pp. 54–63, February 2004.

[207] M. Regis, O. Llopis, and J. Graffeuil, "Nonlinear modeling and design of bipolar transistors ultra-low phase-noise dielectric-resonator oscillators," *IEEE Transactions on Microwave Theory and Techniques*, vol. 46, no. 10, part 2, pp. 1589–1593, October 1998.

[208] R. J. van de Plassche, J. H. Huijsing, and W. M. Sansen, Eds., *Analog Circuit Design : RF Analog-to-Digital Converters; Sensor and Actuator Interfaces; Low-Noise Oscillators, PLLs and Synthesizers.* Springer, 1997.

[209] F. L. Walls and D. W. Allan, "Measurements of frequency stability," *Proceedings of the IEEE*, vol. 74, no. 1, pp. 162–168, January 1986.

[210] F. Vernotte, J. Groslambert, and J. J. Gagnepain, "A new method of measurement of the different types of noise altering the output signal of oscillators," *IEEE Transactions on Instrumentation and Measurement*, vol. 42, no. 6, pp. 968–975, December 1993.

[211] F. Vernotte, E. Lantz, J. Groslambert, and J. J. Gagnepain, "Oscillator noise analysis: multivariance measurement," *IEEE Transactions on Instrumentation and Measurement*, vol. 42, no. 2, pp. 342–350, April 1993.

[212] J. Rutman, "Characterization of phase and frequency instabilities in precision frequency sources: Fifteen years of progress," *Proceedings of the IEEE*, vol. 66, no. 9, pp. 1048–1075, September 1978.

[213] D. W. Allan, "Time and frequency (time-domain) characterization, estimation, and prediction of precision clocks and oscillators," *IEEE Transactions on Ultrasonics, Ferroelectrics and Frequency Control*, vol. 34, no. 6, pp. 647–654, November 1987.

[214] J. Rutman and F. L. Walls, "Characterization of frequency stability in precision frequency sources," *Proceedings of the IEEE*, vol. 79, no. 6, pp. 952–960, June 1991.

[215] W. F. Egan, "An efficient algorithm to compute Allan variance from spectral density," *IEEE Transactions on Instrumentation and Measurement*, vol. 37, no. 2, pp. 240–244, June 1988.

[216] *LabView 7*, National Instruments Co., 11500 N Mopac Expwy, Austin, TX 78759-3504, USA, 2004. [Online]. Available: http://ni.com/labview/

[217] C. A. Greenhall, "Does Allan variance determine the spectrum?" in *Proceedings of the 1997 IEEE International Frequency Control Symposium*, Orlando, USA, May 1997, pp. 358–365.

[218] ——, "Spectral ambiguity of Allan variance," *IEEE Transactions on Instrumentation and Measurement*, vol. 47, no. 3, pp. 623–627, June 1998.

[219] M. Agarwal, K. K. Park, M. Hopcroft, S. Chandorkar, R. N. Candler, B. Kim, R. Melamud, G. Yama, B. Murmann, and T. W. Kenny, "Effects of mechanical vibrations and bias voltage noise on phase noise of MEMS resonator based oscillators," in *Proceedings of the 19th IEEE Micro Electro Mechanical Systems Conference, MEMS '06*, Istanbul, Turkey, January 2006, pp. 154–157.

[220] ADTEK Photomask. 4950 Fisher St., Montreal, QC, Canada, H4T 1J6. [Online]. Available: http://adtekphotomask.com/

[221] *Maple version 10*, Waterloo Maple, Inc., 57 Erb St W., Waterloo, Ontario, N2L 6C2, Canada, 2005. [Online]. Available: http://www.maplesoft.com

[222] *Matlab Version R14*, The MathWorks, Inc., 3 Apple Hill Drive, Natick, MA 01760-2098, USA, 2005. [Online]. Available: http://www.mathworks.com/

[223] *LMF100 Datasheet*, National Semiconductor Corp., Santa Clara, CA, USA, July 1999. [Online]. Available: http://www.national.com/pf/LM/LMF100.html

[224] *FilterPro MFB and Sallen-Key Design Program*, Texas Instruments Inc., Dallas, TX, USA, May 2004. [Online]. Available: http://focus.ti.com/docs/toolsw/folders/print/filterpro.html

[225] J. L. Hilburn and D. E. Johnson, *Manual of active filter design*, 2nd ed. USA: McGraw-Hill, 1983.

[226] M. Tabandeh, *Pulse technique and digital circuits.* Iran: Sharif University of Technology Press, 1997, in Persian.